Université du Québec
Institut National de la Recherche Scientifique
Centre Énergie Matériaux Télécommunications

Munich University of Applied Sciences
Department of Applied Sciences and Mechatronics

Elemental analysis of multilayer and aerosol samples by simultaneous laser-based XRF and PIXE

Par

Nils Dietrich

Thèse présentée pour l'obtention du grade de
Maître es Sciences (M.Sc.)
en sciences de l'énergie et des matériaux

13.08.2025

Jury d'évaluation

Research Director	Prof. Dr. Patrizio Antici
Research Co-Director	Prof. Dr. Alfred Kersch
Internal Reviewer, Jury President	Prof. Dr. Andreas Rüdiger
External Reviewer	Prof. Dr. Jörg Schreiber

Eidesstattliche Erklärung

Ich versichere hiermit, dass ich meine Master's Thesis mit dem Thema

"*Elemental analysis of multilayer and aerosol samples by simultaneous laser-based XRF and PIXE*"

selbstständig verfasst und keine anderen als die angegebenen Quellen und Hilfsmittel benutzt habe. Im Rahmen des Double Degree-Programms mit dem Institut national de la recherche scientifique wird diese Arbeit nur der Hochschule München und dem Institut national de la recherche scientifique vorgelegt. Sie wurde bisher keiner anderen Prüfungsbehörde vorgelegt und auch nicht veröffentlicht.

Varennes, den 13.08.2025

Nils Dietrich

Acknowledgements

I would first and foremost like to express my deepest gratitude to my supervisor, Patrizio Antici, for his guidance and support throughout my Master's journey. Your expertise, insightful feedback, and constant encouragement were instrumental in the development and completion of this work. I am truly grateful for the opportunities you have provided me and for the mentorship that has shaped me as a researcher. I also want to thank the rest of Patrizio Antici's team (namely Elias Catrix and Canan Yagmur Boynukara) for their constant help, feedback, and technical insights. I also want to thank the technical team of the ALLS facility, as well as Simon Vallières for the opportunity to work with them on various projects and for their availability, patience, and support regarding all my questions. Thanks to your feedback and help, I had the opportunity to learn a lot about a new topic and make the project a success. I especially want to thank Patrizio, Elias, Dennis, and Sebastian for their assistance and time in proofreading my thesis.

I also want to thank both the *Munich University of Applied Sciences* and the *Institut national de la recherche scientifique*, who took part in the double degree program together. I want to express my deepest gratitude for receiving this kind of amazing and unique opportunity to finish my studies abroad. I want to primarily extend my thanks to Prof. Andreas Ruediger and Prof. Christina Schindler, on whose shoulders this program was constructed, but also to everyone else who was involved in the creation and constant evolution of this program.

Finally, I owe my most profound thanks and gratitude to my family and friends for their unconditional love and unwavering support. To my parents and my brother, thank you for everything; your belief in me and your continuous support in my decisions have been my greatest motivation. I also want to dedicate this thesis to our family dog Sugar, who sadly passed away this year. She accompanied me throughout all of my studies with her joyful nature and always knew how to cheer me up. I miss her dearly and will always keep her in my heart. I also want to give my sincere thanks to my friends back in Munich, especially my friend Dennis, as well as the new ones I made along the way during my time here in Canada, for their enduring encouragement and support from near and afar. My experience in Canada would not have been this amazing without all your support.
I am truly looking forward to continuing to work and enjoying the next four years together during my PhD studies.

Abstract

This thesis presents the implementation of a layer-by-layer analysis for the chemical composition of multilayer samples, using a combination of laser-driven Particle-Induced X-ray Emission (PIXE) and X-Ray Fluorescence (XRF) at the ALLS facility in Varennes, Canada. To this end, the capabilities of a *MATLAB* routine based on previous work of the same group were extended, and a new routine for the analysis was developed. A proton energy selector was integrated into the experimental setup, with the two components forming the basis for the proposed multilayer measurement method from the software and hardware side. The functionality of the energy selector in the ALLS beamline was verified and calibrated. The custom *MATLAB* routine was finalized and validated using existing measurement data. For the full identification of potential shortcomings of the new methodology, future experiments with metallic multilayer samples have already been planned and scheduled, which will deliver further experimental data. Additionally, it is demonstrated that the simultaneous use of PIXE and XRF, generated through the interaction of a high-power laser with a target, can be employed to analyze aerosols and emission gases in air. The aerosol experiments indicate that krypton (Kr) dilutions can be reliably detected, with projections suggesting the capability to measure and quantify dilutions down to several hundred ppm when compared to a reference measurement. The system is, however, currently constrained by the hardware of the valve system.

Zusammenfassung

In dieser Arbeit wird die Implementierung einer schichtweisen Analyse der chemischen Zusammensetzung von Mehrschichtproben vorgestellt. Diese Methodik basiert auf der Kombination von laserinduzierter „Particle-Induced X-ray Emission“ (PIXE) und „X-ray Fluorescence“ (XRF), im Folgenden als XPIF bezeichnet, welche an der *ALLS*-Lasereinrichtung in Varennes, Kanada, angewandt wurde. In diesem Zusammenhang wurden die Berechnungen einer bestehenden *MATLAB*-Routine aus derselben Arbeitsgruppe erweitert und eine neue Routine zur Analyse von Mehrschichtproben implementiert. Zusätzlich wurde eine neue Hardwarekomponente zur Auswahl der Protonenenergien in den bestehenden Messaufbau integriert, und deren Funktionalität überprüft und kalibriert. Die Software und die Hardwarekomponente bilden die Grundlage für die präsentierte Methodik zur Analyse von Mehrschichtsystemen. Die neue *MATLAB*-Routine wurde fertiggestellt und mithilfe von bestehenden Messdaten validiert. Zur genauen Identifizierung und Behebung potenzieller Fehler sind bereits neue Experimente mit metallischen Mehrschichtproben geplant, welche die notwendigen Daten liefern werden. Des Weiteren wird demonstriert, dass die simultane Anwendung von PIXE und XRF, induziert durch die Wechselwirkung eines Hochleistungslasers mit einer dünnen Folie, genutzt werden kann, um Aerosole und Emissionsgase direkt in der Umgebungsluft zu detektieren. Die XPIF-Experimente mit Aerosolen zeigen, dass Krypton (Kr) zuverlässig detektiert werden kann. Die Ergebnisse deuten darauf hin, dass der Messaufbau Konzentrationen bis zu einigen hundert ppm nachweisen und quantifizieren kann, sofern eine Referenzmessung vorliegt. Derzeit ist das System jedoch durch die Hardware der Gaszufuhr limitiert.

Résumé

Cette thèse présente la mise en œuvre d'une analyse couche par couche de la composition chimique d'échantillons multicouches, en utilisant une combinaison des techniques Particle-Induced X-ray Emission (PIXE) et X-Ray Fluorescence (XRF) induites par laser sur l'installation ALLS à Varennes, Canada. Afin de réaliser l'analyse couche par couche, les capacités d'un programme *MATLAB* basé sur les travaux antérieurs du même groupe ont été étendues, et un nouveau programme d'analyse a été développé. De plus, un sélecteur d'énergie de protons a été intégré au montage expérimental. Ces deux élément forment la base, logicielle et matérielle, de la méthode de mesure multicouche proposée. La fonctionnalité du sélecteur d'énergie sur la ligne de faisceau de l'ALLS a été vérifiée et calibrée. Le programme *MATLAB* relatif à cette étude a été finalisé et validé à l'aide de données de mesure existantes. Qui plus est, afin d'identifier toutes les lacunes potentielles de la nouvelle méthodologie, de futures expériences avec des échantillons métalliques multicouches ont déjà été planifiées, permettant ainsi l'acquisition de données expérimentales complémentaires. De plus, il est démontré que l'utilisation simultanée des techniques PIXE et XRF, obtenues par l'interaction d'un laser de haute puissance avec une cible, peut être employée pour analyser les aérosols et les gaz d'émission dans l'air. Les expériences menées sur les aérosols ont démontré qu'il est possible de détecter de manière fiable des dilutions de krypton (Kr). Les projections indiquent une capacité à mesurer et quantifier des concentrations allant jusqu'à plusieurs centaines de ppm par rapport à une valeur de référence. Les performances du système sont principalement limitées par le dégazage des parois en aluminium de la chambre PIXE et par le comportement non linéaire de la jauge de pression à des pressions inférieures à 1 torr.

Contents

List of Figures

List of Tables

Acronyms

Al aluminum.

ALLS Advanced Laser Light Source.

Ar argon.

Au gold.

Be beryllium.

C carbon.

Ca calcium.

CCD Charge Coupled Device.

Cr chromium.

Cu copper.

EDX Energy Dispersive X-ray fluorescence.

Fe iron.

FWHM Full Width Half Maximum.

H hydrogen.

Kr krypton.

MCP Micro Channel Plate.

MDL Minimal Detectable Limit.

N nitrogen.

Ni nickel.

O oxygen.

PDD Percentage Depth Dosage.

PIGE Particle-Induced Gamma-ray Emission.

PIXE Particle-Induced X-ray Emission.

SEM Scanning Electron Microscope.

Si silicon.

SNR Signal to Noise Ratio.

SPE Single Pixel Event.

Ta tantalum.

Ti titanium.

TNSA Target Normal Sheath Acceleration.

ToF Time of flight.

TP Thomson Parabola.

XPIF X-ray and Particle Induced X-ray Fluorescence.

XRF X-Ray Fluorescence.

1 Introduction

In the last decades, a strong effort has been put into the research of innovative diagnostics techniques able to obtain as much information as possible by using equipment with improved characteristics, i.e., quicker readout, higher sensitivity, and more portability. Advanced spectroscopic techniques, particularly Particle-Induced X-ray Emission (PIXE) and Particle-Induced Gamma-ray Emission (PIGE) [1], are among the most effective and sensitive methods for comprehensive chemical characterization of bulk materials relying on the emission of element-specific X-rays [1, 2]. They are highly sensitive and potent analytical tools, often chosen when detailed compositional data (qualitative and quantitative) is required. In many domains, the non-destructive nature of these techniques proves to be a significant advantage as well. Currently, both PIXE and PIGE depend on employing large particle accelerators. This presents a key drawback of the measurement techniques because the massive scale and intricacy of the necessary infrastructure restrict their usage in a broader field of applications significantly.
Besides the use of accelerators, PIXE can also be achieved through laser-based sources, which utilize high-intensity and short-pulse laser systems in the TW or PW regime. Applications for proton beam, such as medicine and biomedical applications [3, 4], picosecond metrology [5], stress testing [6, 7] and probing of materials [8, 9], cultural heritage [10, 11], as well as environmental applications have prompted the construction of multiple o these laser-beamlines across the world. Examples of facilities capable of producing laser-accelerated particles include the Advanced Laser Light Source (ALLS) in Canada [12], APOLLON in France [13], and VEGA in Spain [14]. Conventional accelerator facilities linked especially to cultural heritage investigations include the AGLAE facility at the French Louvre Laboratory C2RMF [15] or the INFN-LABEC laboratory [16,17], located in Florence.
Besides PIXE, other similar techniques for the probing of chemical compositions exist, with the main candidates being X-Ray Fluorescence (XRF) [2] or the electron-based Energy Dispersive X-ray fluorescence (EDX) [18]. In this thesis, a combination of PIXE and XRF (named X-ray and Particle Induced X-ray Fluorescence (XPIF)), both well-established techniques in the field, is utilized to analyze all samples regarding their chemical composition. The technique offers a non-destructive, multi-element analysis with the possibility for quantitative analysis of the sample composition. The presented experiments in this work were performed at the ALLS facility in Canada, utilizing the 150 TW Ti:Sapphire beamline for the acceleration of protons. By using thin foils for the Target

Normal Sheath Acceleration (TNSA) process, proton beams from low MeV energies up to ∼6 MeV and integrated proton yields of up to 10^{10} - 10^{12} are generated [2]. It is a routinely available and established acceleration mechanism that provides high stability and reliability [1]. The key advantage of this unique setup is the utilization of additional X-rays produced by Target Normal Sheath Acceleration (TNSA), increasing the yield of characteristic X-rays and thereby reducing the number of laser shots necessary for a single measurement.

It can be seen that PIXE is an area of increasing interest within the scientific community, with major facilities such as ELI and C2RMF dedicating specific beamlines (ELIMAIA and AGLAÉ, respectively) to experimental investigations [19, 20]. The technique is a prominent diagnostic method and has frequently been discussed in recent scientific publications. While there is substantial interest from various research groups and a considerable amount of experimental data available, a robust analytical tool for multilayer samples, particularly for incident proton energies between 1 and 7 MeV, remains a critical bottleneck. Therefore, this work aims to establish the foundational framework to address this current deficiency.

1.1 Objectives

The primary advantage of using heavily charged particles (e.g., protons) for X-ray emission analysis over electrons (EDX) lies in their distinct energy deposition profile within a material. As they traverse matter, heavy ions deposit the majority of their kinetic energy in a narrow region at the end of their trajectory. Protons with an energy of 70 MeV will deposit 6 times the amount of energy at the peak location compared to the entry point. For lower energies, the ratio is expected to increase even more [21]. The depth at which this peak occurs is mainly dependent on the initial energy of the sample. Combined with the overall higher penetration depth up to the cm range [21, 22], this enables the probing of samples at a specified location inside an originally much greater interaction volume. However, even when using a broad proton spectrum, samples located underneath a layer of a different material can be tested. While the broad proton spectrum generally increases the X-ray yield, it also makes the quantitative analysis more complex since most interactions with the material depend on the energy of the incoming particle. This gives rise to the work of this thesis, which is structured around the following two objectives:

1. The primary objective is the layer-by-layer elemental analysis of multilayer samples with unknown compositions. To this end, custom *MATLAB* code was developed and optimized specifically for this purpose, serving as the principal analytical tool. This code performs the entire analysis, which consists of interpreting the raw data gathered from the X-ray camera, analyzing the spectrum, and calculating the amounts of each element within the substance. For multilayer samples, these calculations need to take into consideration the various interactions of protons and

X-rays with other layers above the targeted interaction volume. The scanning of a sample layer by layer is achieved using a so-called "energy selector" placed between the proton beam and the sample. The necessary hardware used for the energy selection process will be implemented, verified, and calibrated. The proposed method is expected to prove especially useful for cultural heritage and material science applications, with other potential future expansion into the semiconductor industry and biological domain.

2. For the second objective, this work will show the feasibility of performing the XPIF technique on aerosols. For this purpose, different dilution percentages of krypton (Kr) were diluted in air, which was directly irradiated by the proton beam. The high precision (typically 100 ppm) of PIXE allows for detecting harmful trace elements embedded in an aerosol [23]. While in the case of aerosols trapped in filters, EDX/SEM is a valid option for trace element analysis [24], only very limited data is available regarding the detection threshold, and the sample preparation proves to be more complex. Combined with the inability of EDX to be performed directly in air, a limitation that XPIF does not have, it will be shown that PIXE presents a viable alternative for this field of research. Additionally, comparing the cross sections for common elements contained in gases (carbon (C), oxygen (O), hydrogen (H), nitrogen (N), argon (Ar) and calcium (Ca)) as well as Kr, one can find that protons in the PIXE energy range of interest offer 10 times up to 1000 times bigger cross-sections compared to electrons at typical EDX/SEM energies of 30 keV [25] and tantalum (Ta) K_α (60 keV) respectively [26–28].

1.2 Thesis outline

The thesis is structured as follows: First, the physical groundwork and the equations needed for understanding the presented measurements and the calculations are introduced. Afterwards, the measurement setup and the *MATLAB* code used for data analysis will be explained in detail. Lastly, the results of the analysis and improvements of the code will be discussed as well as analyzed, and a short outlook for potential future work will be given.

2 Theory

This chapter introduces the necessary theory and physical fundamentals required to understand the experiments, code, and measurement data presented later in this thesis. It first describes the generation of the proton beam and X-rays used to probe the material, followed by a discussion of the various interactions between these particles and photons within solid matter.

2.1 Particle-Induced X-ray Emission and X-Ray Fluorescence

The fundamental approach of X-Ray Fluorescence (XRF) and Particle-Induced X-ray Emission (PIXE) is very similar to the aforementioned EDX. In EDX, the sample is bombarded with electrons. However, the main principle of XRF and PIXE is the excitation of electrons of an atom by irradiation of photons (X-rays) and ions (protons). The produced X-ray spectra will then be analyzed, which enables the determination of the chemical composition of the irradiated sample as well as the proportions of each element contained in the probed material. Both measuring techniques pose the advantages of being nondestructive, able to identify multiple elements at once, while also being fast and offering a low detection threshold (PIXE) and high sensitivity [29, 30]. This makes them good candidates for trace element analysis, where the element concentrations are very low or only a limited amount of sample material is available. The measurement can be performed on solid, liquid, and, as will be shown later, on gaseous samples as well. Besides the excitation mechanism, they also differ in the analytical volume, background distribution, detection limits, and performance on different types of samples [9]. Depending on the energy, XRF can offer a relatively high analytical area (up to a few mm, depending on the material). Compared to that, the analytical area of PIXE is smaller (up to a few dozen µm depending on the proton energy and spread). They behave differently regarding the background signal or noise. In PIXE, the background signal gets smaller for elements with a higher atomic number. In XRF, the background noise becomes more prominent as the atomic number increases, making it more suited for samples containing elements of lower atomic numbers. Therefore, both techniques complement each other's weaknesses, making them a suitable combination for elemental analysis, with the control of the analytical depth being driven only by the PIXE mechanism [1].
The measurements performed in this thesis result in X-ray spectra, which are subse-

quently analyzed by software presented in a later section. For an accurate interpretation and understanding of the data presented later in the thesis, the physical principles of X-ray generation will be briefly explained. A typical X-ray spectrum is composed of a continuous part (Bremsstrahlung) and a line spectrum, also called "characteristic spectrum" [9, 31]. The characteristic spectrum is, as the name suggests, indicative of each element. The process of the generation of such a spectrum is best described using the Bohr theory of the atom, as shown in Figure 2.1. It is a simplified model that groups the orbital electrons in 3 shells: K, L, and M. In reality, each shell consists of several sub-shells, characterized by their quantum number. However, for the understanding of this thesis, the simple Bohr model is sufficient [32].

Figure removed due to copyrights issues

Figure 2.1 Generation of characteristic K-shell X-rays shown using the atomic model devised by Bohr. An incoming X-ray or proton with sufficient energy kicks out an electron from the K shell. The vacancy gets filled by an electron of a higher energy level, and the difference gets emitted in the form of a photon. The resulting line in the energy spectrum is named K_α and K_β depending on the transition which occurs [33].

Characteristic X-ray radiation is emitted when an electron is removed from an atom by an external excitation source. This electron ejection most commonly occurs through collisions with other electrons, but can also result from excitation by energetic protons or photons, provided they possess sufficient energy. The removal of an electron leaves the atom in an ionized state with a vacancy. An electron from a higher shell then transitions to this lower, energetically more favourable state to fill that vacancy. The energy difference between the old and new states of the electrons results in the emission

of a photon (typically X-rays). As these energy gaps and hence the photon energies are unique to each element, this phenomenon allows for the characterization of the constituent elements within a sample based on a measured spectrum.
While all transitions are possible, the most likely transitions are the ones where the electron falls back to the innermost K-shell. The resulting lines in the spectrum are called K_α and K_β (shown in Figure 2.2), depending on the energy level from which the electron drops down. The two transitions from the L- and M-shells are by far the most dominant in terms of relative intensity and probability and are thus primarily used for the analysis of X-ray spectra. The analysis in this work is similarly based solely on the K_α and K_β lines, because of the low intensity of the $L_{\alpha,\beta}$ lines as well as the fact that most of them can not be detected by the current setup (see subsubsection 3.1.4).

Figure removed due to copyrights issues

Figure 2.2 Typical characteristic X-ray spectrum induced by PIXE. The visible peaks correspond to the K_α lines of the corresponding elements [9].

Besides the emission of a photon, it is also possible for the energy to be used to release a second electron from the atom. This is called the Auger effect. It is, however, mostly present in elements with a low atomic number ($Z < 12$) [32] and will not be further elaborated upon, since those elements are not within the X-ray detector range, discussed in chapter 3.

2.2 Target normal sheath acceleration

In this section, the process of generating an ion beam using laser-driven ion acceleration is explained. The possibility of generating ions by utilizing a laser is no new concept. Driven by the introduction of lasers with femtosecond pulse lengths, the first experiments of Target Normal Sheath Acceleration (TNSA) based on metallic targets (Aluminum) were published in the year 2000 [34, 35]. The the following years, the topic became a field of research of high interest. Therefore, over the last decades, a lot of improvements have been made to the process and systems involved, opening the door for a multitude of applications in various fields of research. Laser-driven ion beams offer unique characteristics, such as their high particle numbers and very energetic and intense burst shape. TNSA gets its name from the fact that ions are expanding in the normal direction from the rear surface of the target in a cone beam-like fashion. Since its discovery, laser-driven ion beam systems, their characteristics, and their applications have been the subject of many different works of research. Before discussing its applications, it is first necessary to understand the working principle of the TNSA mechanism. Since it is not the main focus of this thesis, the theory of the TNSA process and its mathematical descriptions will not be discussed in elaborate detail.
In general, to produce an ion beam by the interaction of a laser with a solid foil target, the following conditions have to be met [36–38]:

- A high intensity laser pulse typically exceeding $10^{18} \frac{W}{cm^2}$, required for the ponderomotive force effect to occur
- A very short pulse length ($<$ ps regime), enabling high intensities. The pulse duration needs to be shorter than the expansion time of the target, so the back surface is still unperturbed when the shockwave reaches it
- A high laser contrast refers to a high-intensity ratio between the main laser pulse and any unwanted pre-pulses, also called amplified spontaneous emission (ASE) [39]
- A very thin interaction target, usually in the nanometric or micrometric thickness range

State-of-the-art laser-acceleration systems rely on tunnel ionization to generate ion beams. The first step for the TNSA mechanism is the generation of hot electrons via the laser's ponderomotive force, causing a change in charge distribution inside the target material. The acceleration of ions is then caused by the consequent charge separation fields. The basics of the TNSA technique, discussed in this section, are schematically depicted in Figure 2.3. The TNSA process, shown in Figure 2.3, has been extensively described in the works of M. Roth and M. Schollmeier [36] as well as J. Schreiber [39], with the most crucial information being summarized in this section.

Figure removed due to copyrights issues

Figure 2.3 Schematic depicting the Target Normal Sheath Acceleration process extracted from [36]. The incoming laser pulse interacts with the interaction target (thickness in the μm range). The pre-pulse creates the pre-plasma, which the main pulse interacts with. Afterward, the MeV electrons are propelled through the target and try to escape into the vacuum on the rear surface, creating a dense electron sheath. The charge separation fields ($\sim \frac{TV}{m}$) then ionize the atoms and impurities on the back side of the foil, which get accelerated by the sheath field in the normal direction.

For an efficient acceleration of protons, it is essential to maintain an unperturbed target surface up to the impact of the main pulse. This requires a high temporal contrast ratio ($\geq 10^6$) to suppress prepulses that might induce premature plasma formation. Above the electron's relativistic intensity threshold ($I_L > 10^{18} \frac{\mathrm{W}}{\mathrm{cm}^2}$ for a laser wavelength of 1 µm), the intense electromagnetic wave propels electrons forward from the target via the relativistic ponderomotive force. These electrons are predominantly ionized from the target material through high-field tunnel ionization [40]. The conversion efficiency of this process is not perfect but can reach values up to 90% for ultra-high intensities and irradiance at an angle smaller than 45%. This means that still plenty of highly energetic electrons, which are needed for the process, are generated. The number of generated hot electrons can be estimated by $N = \frac{\eta E_L}{k_b T_{hot}}$ [36], with E_L being the laser energy and T_{hot} the cycle averaged kinetic energy of an electron oscillating in the laser electromagnetic field.

In the intensity range of 10^{18} - 10^{20} $\frac{\mathrm{W}}{\mathrm{cm}^2}$, the accelerated electrons experience significant heating, predominantly due to $\vec{J} \times \vec{B}$ and vacuum heating absorption mechanisms [40]. Afterwards, the hot electrons travel through the target at relativistic velocities and leave the target material via the rear side. The relativistic velocities ensure that the mean free path of the electrons is much greater than the target thickness. However, only a fraction of electrons manage to exit the material. To minimize the self-generated

magnetic field that stems from the travelling electrons, counter-currents in the opposite direction are generated. While this process, schematically shown in Figure 2.4, affects the forward motion of the electrons, without it, the magnetic field resulting from the laser-driven charge separation would only allow the electrons to travel a few nm. Besides counter-currents, the electrons also undergo collisions and therefore scattering inside the material. This results in a divergence/broadening of the electron distribution, which also reduces the effect of the self-generated magnetic field [36, 39]. On the rear side, most of the electrons are retained due to strong charge separation, driven by the target's capacitance. There they form an electron cloud (also called the "sheath") that establishes an intense quasi-electrostatic electric field over a distance comparable to the Debye length λ_D [40, 41].

Figure removed due to copyrights issues

Figure 2.4 Schematic of laser-generated fast electron transport inside the laser-interaction target. The generated electron current j_{fast} (green) causes the germination of filamentation (light-red) and magnetic fields (blue). At the backside of the target, the electrons form a sheath which causes recirculation $j_{ret.}$ and confinement of the electrons inside the target. The figure is extracted from [36].

The electron density at the rear side strongly scales with the laser intensity and is inversely proportional to the square of the target thickness. The resulting electric field is strong enough to electrostatically confine lower-energy electrons inside the target foil, making them unable to leave the material. These electrons start to recirculate inside the target material, creating strong charge separation fields in the range of several $\frac{TV}{m}$. This recirculation becomes mainly important for foils below 10 nm, where it was found that it enhances the maximum proton energy [36].
The longitudinal electric field completely ionizes water molecules and hydrocarbon impurities instantaneously, naturally present on the target back surface. The resulting ions

get accelerated along the target-normal direction. While the ionization through collisions is technically possible, it is mainly driven by the field ionization since its cross-section is much higher. The resulting accelerated ions are able to reach energies in the order of up to hundreds of MeV. The combination of a steep plasma density gradient, a high-intensity electromagnetic wave, and ions starting from rest on a cold surface produces energetic ion beams that are strongly forward-oriented (i.e., non-isotropic). These beams exhibit very low divergence at their source, resulting in high beam quality. The short duration of the laser pulse enables the generation of a steep, hot electron density gradient, which in turn gives rise to a strong accelerating electric field. Additionally, the laser contrast (shown on the left-hand side in Figure 2.3) must be high enough to prevent a too-strong target decompression as well as the formation of a pre-plasma induced by the ASE, before the main pulse interacts with the target. It can be seen that the TNSA mechanism is dependent on the generation of a dense, hot electron cloud, serving as an intermediate step in the energy transfer from the laser to the protons. [38] is explained by a plasma expansion model [40, 42].

To conclude this section, it is important to mention that besides electrons, protons, and other ions, some additional X-rays are also generated during this process [2]. In general, it can be said that the ejected photon energies correlate with the K_α and K_β lines of the target material. For materials with a higher atomic number, the spectrum broadens due to Bremsstrahlung [27]. The experiments later described in this thesis, for now, only include protons and characteristic X-rays in the yield calculations [36].

2.3 Interaction of X-rays and ions with matter

This section will first examine the interaction of protons and X-rays with a sample. This includes the loss of energy while traversing through a sample as well as the generation of the previously mentioned characteristic X-rays. All important formalisms and equations, which are later utilized in the analysis of the X-ray spectra using a custom-written *MATLAB* code, will be explained in detail.

Bragg's additivity rule

Before discussing the interactions of X-rays and protons in matter as well as quantifying and calculating their physical characteristics, an important rule called Bragg's additivity rule (Bragg and Kleeman 1905 [43]) needs to be introduced. This principle is used to calculate properties such as stopping power or attenuation coefficients for compound materials. While these values are often available in databases for pure elements, they are typically not provided for compounds. Bragg's rule addresses this limitation by stating that a property of a compound material can be approximated by the weighted sum of the properties of its constituent elements [9, 44, 45]:

$$\frac{S}{\rho} = \sum_i w_i \left(\frac{S}{\rho}\right)_i , \tag{2.1}$$

where $\frac{S}{\rho}$ is the mass stopping power and w_i is the fraction by weight of each element present in the sample. One can imagine this method by replacing the bulk material with a series of very thin sheets of each constituent element. Given the simplicity of Equation 2.1, one can surmise that this rule is only an approximation. In reality, the modelling of compounds is much more complicated. It does not take into account the effects of chemical bonds, physical states, or the lattice structure [9]. Despite these neglections, it still is proven to hold true quite well [44].

2.3.1 Mechanisms of X-ray-matter interaction

This section briefly discusses the interaction of X-rays with solid-state samples. It will cover how X-rays lose energy while travelling through matter, followed by an explanation of the X-Ray Fluorescence (XRF) yield in both thin and thick samples.

Beer-Lambert law

In a homogeneous isotropic material, the decrease of the transmitted intensity I of photons with a given energy through matter can be described by a simple exponential equation. This relationship is known as the Beer-Lambert law [46, 47]:

$$I = I_0 \cdot e^{-\mu \cdot d \cdot \rho}, \tag{2.2}$$

where I_0 is the initial intensity, μ the mass attenuation coefficient, and d and ρ the sample thickness and density respectively. Bragg's addition rule continues to hold true in the case of compound materials. μ is related to the absorption cross section of the material σ_i, which is an energy dependant factor. Using copper as an example, Figure 2.5 shows how the mass attenuation coefficient varies for different photon energies. One can identify a sharp edge that corresponds to the energy level of the K-shell. This edge corresponds to the binding energy of the K-shell; at this energy threshold, incident photons are able to eject K-shell electrons, causing a sudden increase in absorption [46].

Figure removed due to copyrights issues

Figure 2.5 The mass attenuation coefficient $\frac{\mu}{\rho}$ (solid line) and the mass energy-absorption coefficient $\frac{\mu_{en}}{\rho}$ (dotted line) in relation to the photon energy in MeV. Extracted from Krause et al. [48]

Cross sections

For a better understanding of the calculations related to the X-ray yield, the importance of cross sections is briefly explained. A cross-section quantifies the probability that a specific interaction will occur between particles. The concept can be simplified by imagining an effective target area presented by a target particle to an incident projectile. However, the physical processes at the quantum level are more complex than this classical analogy suggests. The calculations in this work solely utilize total cross sections, which represent the sum of the cross sections for all possible interaction channels, such as elastic and inelastic scattering, absorption, and nuclear reactions.

Principles of XRF Yield Calculation

When calculating the X-ray yield generated by X-Ray Fluorescence (XRF), the sample thickness is an important consideration. A distinction is generally made between "thick" and "thin" samples. A "thick" sample is one in which the incident radiation is fully attenuated, either through absorption or backscattering. In contrast, a "thin" sample is one where the energy lost by incident photons as they traverse the sample is negligible [9, 31]. For the purposes of this work, a layer is considered "thin" if this energy loss is below 5%. In the case of characteristic copper radiation (8.058 keV), this criterion corresponds to a thickness of ∼1.25 µm for a Cu layer, or ∼570 nm for a Ti layer.

As explained, the thickness of the sample is related to the distance within the sample until which the particle is completely absorbed and not the actual thickness. This distance is called the effective thickness of the material. Therefore, it depends heavily on the nature and energy of the incoming particle as well as the material of the sample. Thick samples bring various aspects of consideration with them, such as secondary fluorescence (described in the next section), self-absorption, and the scatter mass thickness [9]. These characteristics can be described via various cross sections, stopping powers, and attenuation coefficients. The values for these coefficients are well tabulated for multiple energies and materials and are publicly available. Alternatively, they can also be calculated using various free-to-use software like XCOM and SRIM [49,50]. Overall, thick samples deliver a better sensitivity since the intensity of the element is directly related to the element. Thin samples, on the other hand, have the advantage that self-absorption can be neglected and the cross sections stay constant [9]. In the calculations of this thesis, the differentiation between the two formalisms is utilized to calculate the yield in different layers depending on their effective thickness.

The calculations used for the analysis of this thesis are based on the so-called elemental mass concentrations. The fundamental parameter approach is used to relate the measured intensities N_{ij} (number of counts) of the characteristic X-ray lines (K_α,K_β,...) i to the mass m_j of the element j present in the sample [9]:

$$N_{ij} = I_0 G \epsilon_{ij} \beta \cdot m_j \cdot \sigma_{ij}(E). \tag{2.3}$$

G is the geometry factor, ϵ_{ij} the camera efficiency of excitation and detection of the X-rays, σ_{ij} the X-ray fluorescence cross-section, and β the correction term for self-absorption:

$$\beta = \frac{1 - \exp\left[-(\mu_i \csc\phi - \mu_f \csc\psi)\right] M}{(\mu_i \csc\phi - \mu_f \csc\psi) M}, \tag{2.4}$$

with M being the total mass of the sample, μ_i/μ_f the mass absorption coefficient at incident and fluorescent energy and ϕ/ψ the grazing angle of incidence/fluorescence. *csc* stands for cosecant, one of the six trigonometric functions.

The fluorescence cross-section for the K-shell is then calculated according to [51]:

$$\sigma_{ij} = \sigma_K \cdot \omega_K \cdot F_{Kj}, \tag{2.5}$$

where σ_K is the photoionization cross-section, ω_K the fluorescence yield and F_{Kj} the fractional emission rate. ω_K is defined as the probability that radiation occurs during the filling of a vacancy by an electron of a higher shell. F_{ij} gives the ratio of the transition of interest compared to all possible sub-shells. All values for the calculations are available in different databases. According to Krause et al. [51], the combined uncertainty for the yield calculations based on the K_α intensity lies around 5%.
The formalism for thick-target X-Ray Fluorescence (XRF) is applied when the incident X-rays are fully attenuated within the sample. As previously mentioned, the analysis only needs to consider the effective depth. This is the depth beyond which incident X-rays are absorbed, or any generated fluorescent X-rays are unable to escape the sample due to subsequent attenuation. The effective depth is defined as [9]:

$$t_{\text{eff}}(h\nu_{K\alpha/\beta}) = \beta \cdot t = \frac{1 - \exp\left(-\left(\frac{\mu_\gamma}{\cos\theta_1} + \frac{\mu_x}{\cos\theta_2}\right)\right)}{\left(\frac{\mu_\gamma}{\cos\theta_1} + \frac{\mu_x}{\cos\theta_2}\right)} \cdot t, \tag{2.6}$$

with t being the thickness of the sample and β the correction term for self absorption introduced in Equation 2.4. Equation 2.6 results from the integration of the previously mentioned Beer-Lambert law over the sample's thickness. μ_γ and μ_x are the mass absorption coefficients for the incoming and outgoing X-rays, respectively. The thick target yield can then be calculated as follows [9]:

$$Y_{x,i} = \frac{\Omega}{4\pi} N_A \frac{m_j}{M_j} \epsilon_{ij} \left[N_{K\alpha}\sigma_j(h\nu_{K\alpha}) t_{\text{eff}}(h\nu_{K\alpha}) + N_{K\beta}\sigma_j(h\nu_{K\beta}) t_{\text{eff}}(h\nu_{K\beta})\right]. \tag{2.7}$$

For the calculations, a homogeneous and isotropic material is assumed. It is also important to note that characteristic X-rays can only be produced from elements in the sample that have a relevant binding energy lower than the energy of the incident radiation used for XRF.

Elastic diffraction

Instead of penetrating the sample and getting absorbed, the X-rays can also be diffracted by the sample back into the detector. The process depends on the wavelength and angle of the incoming photons and requires a crystalline structure of the surface material. It is based on constructive interference of the reflected beams, with the process being either inelastic or elastic. During previous experiments, it was observed that the X-ray spectrum shows peaks of the element of the laser-interaction target, even though this element is not present in the sample itself. The reason for this is the elastic diffraction of X-rays

back into the detector. While for the mentioned case, these peaks can be safely ignored in the analysis of the sample, this is not the case if the sample contains the same element as the laser-interaction target. Here, the yield of the sample and the diffracted X-rays are indistinguishable from each other, which leads to an overestimation of the element proportion in the sample. To guarantee an accurate quantitative analysis, the diffracted intensity needs to be calculated and accounted for [52, 53].

For the calculations, a monochromatic beam irradiating a powder sample, defined by a large number of small crystals with random orientation, is assumed. Hence, all different hkl (Notation according to Miller indices [52]) planes at which the diffraction can happen are also randomly oriented. Therefore, there will always be a set of planes that satisfy the condition of a Bragg reflection (see Equation 2.9) with the incoming beam. Using copper as an example, since it is a routinely used target material in the ALLS laboratory, and a difference of 90° between the incoming and exiting beam, Bragg's rule shows that the 311 and 131 planes (shown in Figure 2.6) will satisfy the condition.

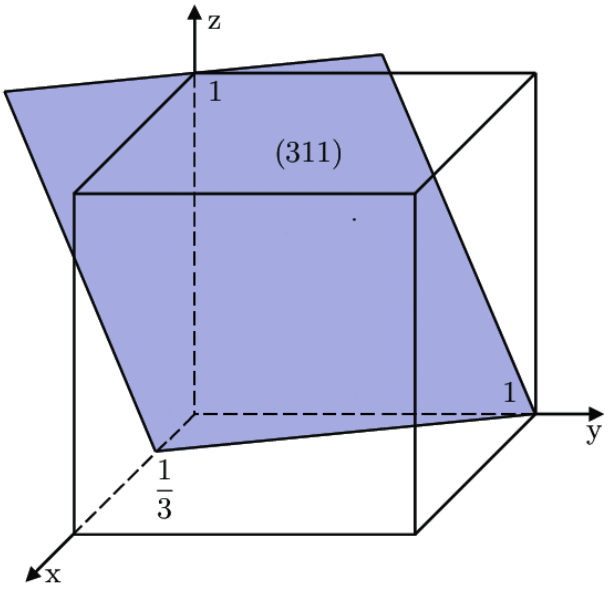

Figure 2.6 Orientation of the crystallographic 311 plane. The 113 plane will have a $\frac{1}{3}$ length in the z-direction instead of the x-direction [54]

$$2d \cdot sin(\theta) = n \cdot \lambda \tag{2.8}$$

$$d_{hkl} = \frac{a}{\sqrt{h^2 + k^2 + l^2}} \tag{2.9}$$

In theory, the 113 plane will generate a peak at a higher incident angle since its interplanar distance is also higher. The total diffracted power of a reflection at a given hkl plane

can be described by multiplying the intensity by the number of crystals and the incident area [52]:

$$P = \frac{I_0}{16\pi R} \cdot (\frac{e^4}{m^2c^4}) \cdot \frac{V\lambda^3 m_{hkl} F_{hkl}^2}{v_a^2} \cdot (\frac{1 + cos^2(2\theta)}{2\, sin(\theta) sin(2\theta)}), \tag{2.10}$$

with V being the effective volume of the crystalline material, I_0 the initial intensity of the photons, m_{hkl} the multiplicity factor, e and m the electron charge and mass, respectively, F the structure factor, v_a the length of a unit cell, and λ the wavelength of the incoming X-rays. The second term, $\left(\frac{e^4}{m^2c^4}\right)$, originates from the Thomson scattering equation, which describes the classical scattering of electromagnetic radiation by a single free electron. The multiplicity factor accounts for the number of symmetry-equivalent crystallographic planes that contribute to the intensity of a single observed diffraction peak. In the case of copper with its face-centered cubic (fcc) structure (shown in Figure 2.7), the multiplicity factor equals 24, which is the amount of combinations with different ± h, ± k and ± l indices of the planes 311, 131 and 113.

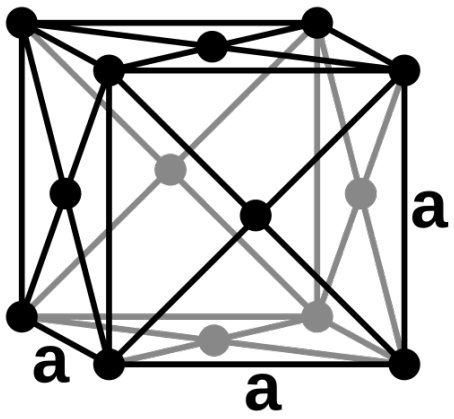

Figure 2.7 Depiction of a cell with the fcc structure, extracted from [55].

The structure factor F_{hkl} represents the resultant wave, combining amplitude and phase, scattered by all atoms within a single unit cell for a specific reflection defined by the Miller indices. For the mentioned Bragg reflection in copper, it is calculated by simply using the crystal structure factor f [52]:

$$F = 4 \cdot f. \tag{2.11}$$

where the prefactor is equivalent to the number of atoms in the cubic cell. The fcc-structure in Figure 2.7, shows that the factor is indeed 4 (8 corner atoms and 6 atoms in the faces, contributing $\frac{1}{8}$ and $\frac{1}{2}$ each to the total number of atoms of the primitive cubic cell). Thermal vibrations are neglected in the calculations in this thesis. The final term in Equation 2.10 introduces the polarization of the incoming beam due to the scattering into the calculations. Equation 2.10 calculates the power per unit length. However, the detector detects the overall intensity of the diffracted photon beam. Therefore, the calcu-

lations need to be adjusted by taking into account the camera distance from the sample and the cone area of the diffracted beam at this distance by multiplying with $2\pi R{\cdot}sin(2\theta)$.

In addition to elastic scattering, inelastic scattering, also known as Compton scattering, can occur as well. The classical theory currently utilized for the calculations only predicts the unmodified scattering (i.e, no change in the wavelength of the material). Contrary to its counterpart, unmodified scattering is incoherent and will therefore produce a diffuse background in the X-ray spectrum, which will be drowned out in the noise and reduce its effects on the measurement. Computing the Compton scattering can be done using the wave mechanical treatment of diffraction and assuming that the intensity of un- and modified scattering equals the intensity of classical scattering for each individual electron [52].

Secondary fluorescence

Another source of X-ray yield while performing PIXE and/or XRF is the so-called secondary fluorescence. In essence, secondary fluorescence describes the process where characteristic X-rays, initially produced by the interaction of the primary beam (made of electrons, protons, or photons) with one element, are then absorbed by another element in the sample, causing the second element to emit its own characteristic X-rays. This phenomenon is especially important when analyzing materials composed of elements with close atomic numbers, like alloys or layered samples. Considering an iron-chromium material: the primary Fe K_α fluorescence (6.40 keV) is energetic enough to eject a K-shell electron from chromium (requiring > 5.989 keV). Consequently, secondary Cr K_α X-rays (5.41 keV) are produced. This enhances the measured Cr signal but means that some Fe K_α photons are absorbed internally, potentially reducing the detected Fe intensity and complicating quantitative analysis [9, 56]. This needs to be taken into account, especially in multilayer systems, since neglecting this effect can lead to an error when estimating the theoretical X-ray yield of a sample. It can either enhance an existing PIXE peak or introduce a completely new line in the spectrum, falsifying the analysis by generating errors in the trace element analysis.

2.3.2 Mechanisms of proton-matter interaction

In this section, the relevant theory of proton interaction with solid matter will be introduced. This will lay the groundwork for the considerations and calculations which become important when discussing the spectrum analysis by the *MATLAB* code in chapter 3.

Energy deposition and stopping power

The process of ions slowing down when traversing hot matter (e.g., at temperatures exceeding 1000°C) is a well-established subject, and its underlying physics are very well understood. The phenomenon is of great importance when using ion beams for the probing of materials, since the information on the energy lost depending on the depth inside the sample is closely tied to the success of a quantitative and compositional analysis. It is a physical interaction that can be very precisely mathematically described [44]. However, for the work of this thesis, the more detailed calculations are not needed for a sufficiently precise analysis.
The calculations are focused on the stopping power S of the sample material, which relates the energy loss dE of the charged particle to the depth travelled in the material x [31, 57]:

$$S(E) = -\frac{d\epsilon}{dx}. \tag{2.12}$$

Charged particles lose their energy in matter in three different ways (1) inelastic collisions (electronic stopping), (2) elastic collisions with nuclei, and (3) radiative stopping via Bremsstrahlung. For particles with high energies above 0.4 MeV and more mass than electrons, the contribution of nuclear stopping power or Bremsstrahlung interactions is relatively small (typically $\sim 0.1\%$ of the total stopping power) [58], and the loss due to radiation becomes negligible. Because of their high comparative mass to electrons, heavy charged particles lose the majority of their energy due to interaction with the orbital electrons of the sample material. In this case, the stopping power can be described by the well-known Bethe-Bloch formalism. The classical derivation, based on the Coulomb force, was originally developed by Bethe and was later improved by Bloch, resulting in [59]:

$$S = -\frac{d\epsilon_K}{dx} = 4\pi\frac{N_A\rho}{M}(\frac{e^2}{4\pi\epsilon_0})^2\frac{z^2Z}{m_e v^2\beta^2}[ln(\frac{2m_e v^2\beta^2}{I(1-\beta^2)}) - \beta^2 - \frac{C}{Z} - \frac{\delta}{2}], \tag{2.13}$$

where N_A is the Avogadro constant, ρ the density, M the molar mass, m_e and e the electron mass and charge respectively, z and v the particle charge and velocity, Z the atomic number and β the speed of light in vacuum. This version of the formalism uses $\frac{C}{Z}$ for the shell correction and $\frac{\delta}{2}$ for the density correction. The first correction accounts for the fact that the particle velocity will be much greater than the velocity of the orbital electrons, and the second term accounts for the dielectric polarization of the target [60].

The stopping power is then used to calculate the macroscopic dose deposition D by protons in the sample, as described by:

$$D = \frac{\epsilon_{dep}}{m} = S(\epsilon_{K,0}, x, z, Z) \cdot \phi. \tag{2.14}$$

The calculations of Equation 2.13 for photons, electrons, neutrons, heavy charged particles, and protons, in the form of the Percentage Depth Dosage (PDD) in water, are depicted in Figure 2.8. Water is often the subject of experiments as well as simulations of proton beams because it is used to model the influence of irradiation on the human body, for example, in tumour treatment procedures [22].

Figure removed due to copyrights issues

Figure 2.8 PDD of different types of particle beams in water, extracted from [22]. Part **(a)** shows the case of photons, **(b)** electrons, **(c)** neutrons, and **(d)** heavy charged particles including protons. The y-axis shows the PDD in percent, and the x-axis displays the penetration depth.

Figure 2.8 shows that the depth-dose characteristic heavily depends on the type of beam used for probing the sample. The main difference of protons compared to electrons, neutrons, or photons is, as seen in Figure 2.8(d), that protons deposit most of their energy at the end of the motion after penetrating the sample. The other particles deposit most of their energy at the beginning of their motion shortly after entering the material. While Figure 2.8 shows the relation between depth and PDD in water, this behaviour does not change significantly in other materials. However, even though the heavily charged particles do lose energy through the previously mentioned Coulomb interactions, it is not accompanied by significant angular scattering. Instead, as the particle slows down, its

energy loss per unit distance increases sharply near the end of its trajectory, causing it to deposit the remainder of its kinetic energy over a very short distance. The consequent peak of the PDD is called a Bragg peak [22] and is of major importance to the work of this thesis. Its location depends on the initial energy of the impinging proton, making it possible to control where the energy is deposited and the characteristic X-rays are generated. One can notice that the final falloff is not instantaneous. The width of the Bragg peak is caused by an effect called range straggling. Since the stopping of protons in matter involves multiple random scattering events, not all protons stop at exactly the same distance. Additionally, the proton beam will be debunched inside the material due to the multitude of individual Coulomb interactions. The straggling results in a Gaussian distribution of the Bragg peak, even if the initial beam is mono-energetic.

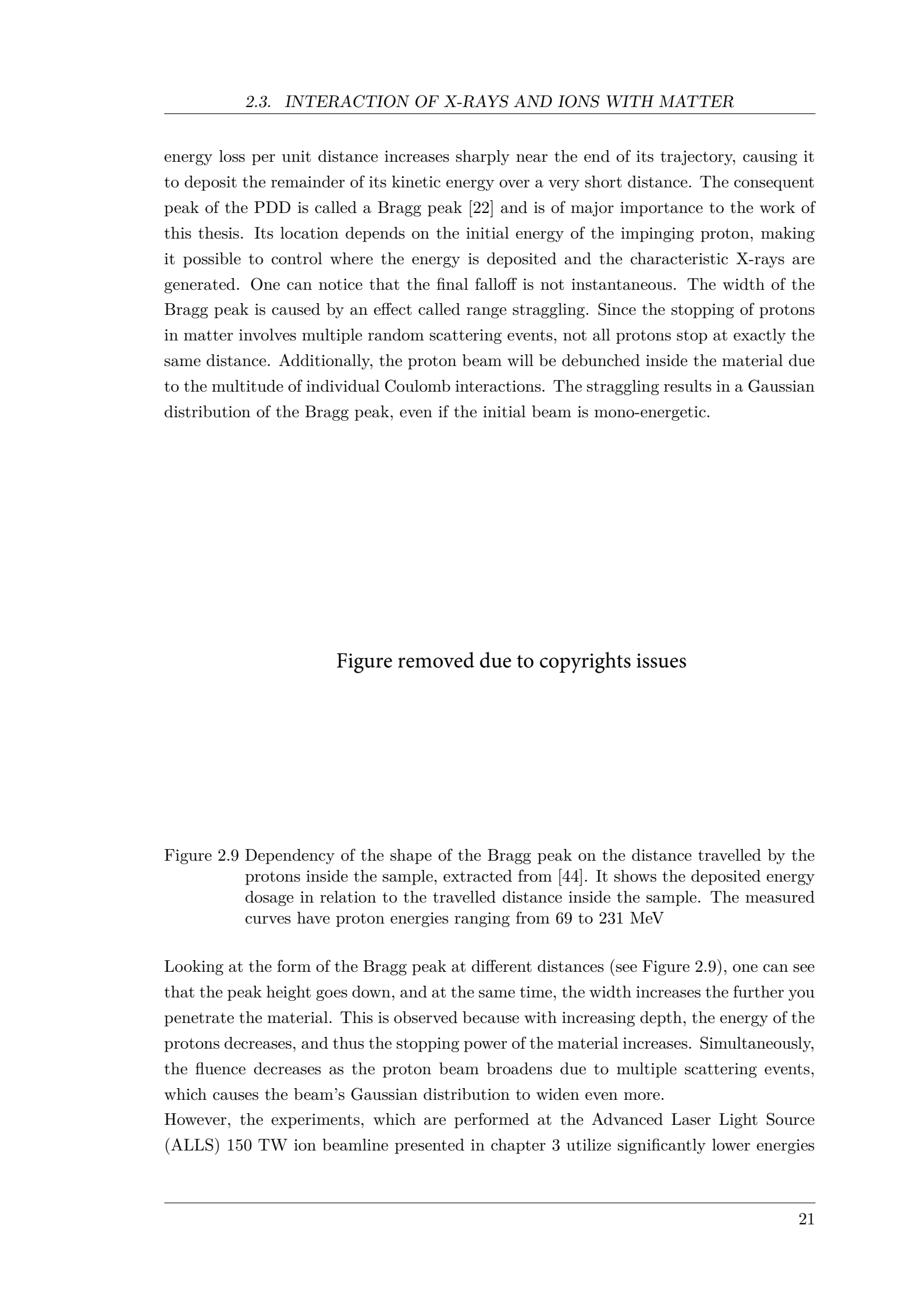

Figure 2.9 Dependency of the shape of the Bragg peak on the distance travelled by the protons inside the sample, extracted from [44]. It shows the deposited energy dosage in relation to the travelled distance inside the sample. The measured curves have proton energies ranging from 69 to 231 MeV

Looking at the form of the Bragg peak at different distances (see Figure 2.9), one can see that the peak height goes down, and at the same time, the width increases the further you penetrate the material. This is observed because with increasing depth, the energy of the protons decreases, and thus the stopping power of the material increases. Simultaneously, the fluence decreases as the proton beam broadens due to multiple scattering events, which causes the beam's Gaussian distribution to widen even more.
However, the experiments, which are performed at the Advanced Laser Light Source (ALLS) 150 TW ion beamline presented in chapter 3 utilize significantly lower energies

than the ones presented in Figure 2.9. The setup achieves a routine production of proton beams with energies up to 6.5 MeV, ensuring sharp peaks and therefore a good accuracy of the depth control.

Principles of PIXE Yield Calculation

For the X-ray yield calculation of the PIXE process, the same fundamental parameter approach as for XRF, which assumes an X-ray yield proportional to the elemental mass concentration, is used. The solid angle, camera efficiency, and self-absorption in the yield calculation are also taken into account. In thin samples, again, only a fraction of the particle energy is deposited while traversing the sample. The yield is then calculated according to [9, 31]:

$$Y_{x_i}(Z, E_0) = \sigma_{x_i}(Z, E_0) \cdot (nt') \cdot N_p \cdot \epsilon_{x_i}, \tag{2.15}$$

where σ_{x_i} is the X-ray production cross-section induced by protons. Different datasets for PIXE calculations, including cross sections, have been summarized by Cohen and Harrigan [61]. In this thesis, a dataset by the same author [62] is used for the calculations. nt' is the area density, which consists of the effective sample thickness and is solely based on the produced X-rays trying to leave the sample, as well as its number density n. Finally, N_p is the number of protons impinging on the sample. If, like in the case of this study, a continuous proton spectrum is used, this calculation needs to be done for each proton energy for which the thin target definition applies.

In the case of thick samples, the protons will deposit all of their energy in the sample. The further they travel in the sample, the more energy they deposit, which results in a decrease of the ionization cross section and stopping power. The resulting integral for calculating the thick PIXE yield looks as follows [9]:

$$Y_{p,i} = \frac{\Omega}{4\pi} N_A M_j m_j \int_{E_0}^{E_1} f_p(E_p) \int_{E_p}^{0} \sigma_j(E) \omega_j T_j(E) \frac{dE}{S(E)} dE_p \tag{2.16}$$

$$T_j(E) = \exp\left(-\mu_j \int_{E_p}^{E} \frac{dE'}{S(dE')} \frac{\cos\theta_1}{\cos\theta_2}\right), \tag{2.17}$$

where Ω is the solid angle, N_A the Avogadro constant, M_j the molar mass, and m_j the mass concentration as explained in the section on XRF yield. $f_p = \frac{d^2N}{dEd\Omega}$ is the broadband distribution of protons, which is generated by the setup described in chapter 3. For the ionization cross section σ_i, values tabulated in the work of Pia et al. [63] that are calculated according to the plane wave Born approximation and Energy-loss Coulomb-Repulsion Perturbed-Stationary-State Relativistic (ECPRSSR) theory [64] are utilized. $S(E)$ is the proton stopping power, which for compounds is again calculated using Bragg's additivity rule, and $T_j(E)$ describes the attenuation of the generated photons inside the sample. For the stopping power, a software called *SRIM* developed by Zielger [50], which

calculates values for various materials and energies, is employed.
An analysis of X-ray spectra using the presented set of equations for the yield calculation is expected to achieve a confidence level of ∼5% [9]. Of course, the results depend on various factors such as the setup, including filters, camera efficiency, and the stability of the proton yield generated by TNSA. While it is possible to have thin layers, generally, the absorption of all available protons somewhere inside the sample is assumed.
The objective of this thesis is to analyze samples of unknown composition. While the yield calculations described previously can be performed without prior knowledge of the sample, other analyses, such as those for elastic diffraction, require compositional information to be performed accurately. Therefore, multiple iterations of measurements are necessary for a correct assessment of the chemical composition. The same limitation occurs when analyzing samples composed of multiple layers with unknown compositions and thicknesses. Potential solutions to this problem are discussed in the following chapter.

Bremsstrahlung

In addition to characteristic X-rays, electrons within the laser-target interaction volume can also generate a continuous spectrum via the Bremsstrahlung mechanism. This type of electromagnetic radiation occurs when a charged particle (most commonly an electron) is deflected by another charged particle (typically the atomic nucleus inside a solid sample). The result is an overlap of the continuous spectrum, which follows a Maxwellian distribution, with the characteristic X-ray lines, as shown in Figure 2.10 [2,9,31,57]. The additional X-rays can also be used to probe the material using standard XRF techniques.

Figure removed due to copyrights issues

Figure 2.10 Typical emission spectrum of an X-ray tube. The less energetic X-rays from the continuous spectrum are reabsorbed inside the target material [65].

The contribution of Bremsstrahlung rises with increasing atomic number. In previous experiments from Jarott et al. [66] it was shown that the Bremsstrahlung spectrum (1 to 100 keV) is roughly the same order of magnitude as the K_α yield for a laser interaction target made from copper. This material will also mainly be used for the experiments presented in this thesis. However, the XRF cross-section is 3 magnitudes smaller at 200 keV (8.44×10^{-1} $\frac{\text{barns}}{\text{atom}}$) than at 10 keV ($5.05 \times 10^{3}$ $\frac{\text{barns}}{\text{atom}}$) for the materials probed in this thesis. Therefore, for the first calculations of the XRF yield, the Bremsstrahlung contribution is neglected. For the aerosol experiments, presented later in this thesis, a tantalum target is used instead of copper. Here, the X-ray yields due to Bremsstrahlung can not be neglected anymore. While no quantitative analysis was performed, the influence and evaluation of the generated Bremsstrahlung will be discussed in more detail in the next chapter.

3 Experimental setup and methodology

In this chapter, the experimental setup as well as the *MATLAB* code used for the analysis of the measurement data are presented. Together, the implementation of both components into the setup forms the basis for the multilayer analysis from both the hardware and software side. The measurement setup is composed of four main components: The main chamber containing the parts producing the proton beam via Target Normal Sheath Acceleration (TNSA), the "energy selector" for controlling the proton energies, the experimental chamber housing the sample, and the diagnostics for monitoring both X-rays and protons. The section regarding the *MATLAB* code covers the peak identification procedure, the implementation of the previously mentioned equations for the various physical events, and how those calculations lead to a quantitative result.

3.1 Experimental setup

The core of the ALLS ion acceleration beam line is the 150 TW Ti:Sapphire laser. It operates at a central wavelength of 800 nm and has a repetition rate of 2.5 Hz. After compression, a pulse length of 22 fs at Full Width Half Maximum (FWHM) is achieved. The beam is then guided into the main chamber, which contains the target for laser interaction. The entire setup is shown in Figure 3.1 and Figure 3.2.

3.1.1 Main chamber

After entering the chamber, the p-polarized beam with a diameter of 100 mm (at e^2) is focused down by a f/3 off-axis parabola at an angle of 20°, achieving a spot diameter of 5 µm (FWHM) when hitting the laser interaction target. The laser interaction target is a very thin foil (typically ∼5 µm) with high purity (>99.9%). In order to perform multiple shots in repetition and take advantage of the fast repetition rate of the ALLS system, a special target holder was developed. It takes 5x5 cm^2 foils and divides them into a matrix of 400 target holes, which are then individually irradiated by the laser. A motorized stage moves the holder to the next position after each shot. The vacuum in the main chamber is held at $<10^{-6}$ mbar. The proton beam, produced by the previously explained TNSA mechanism, is propelled in the normal direction away from the target. The co-mooing electrons, which ensure the stability and neutrality of the beam in the beginning, are being deflected by two magnets (placed 20 cm from the source), with a field strength of ∼0.1 T. This configuration should prevent electrons with energies up to

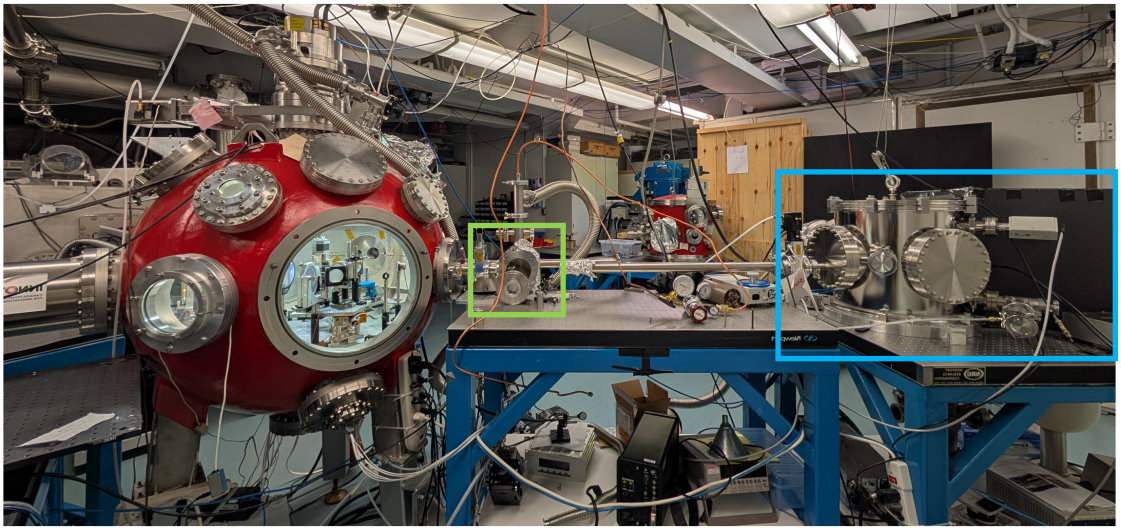

Figure 3.1 Picture of the experimental setup used for proton acceleration and XPIF. The big red housing on the left side of the image is the main experimental chamber, containing the laser-interaction target. In the middle, marked in green, one can see the chamber containing the samples, and the Thomson parabola located on the right-hand side (blue).

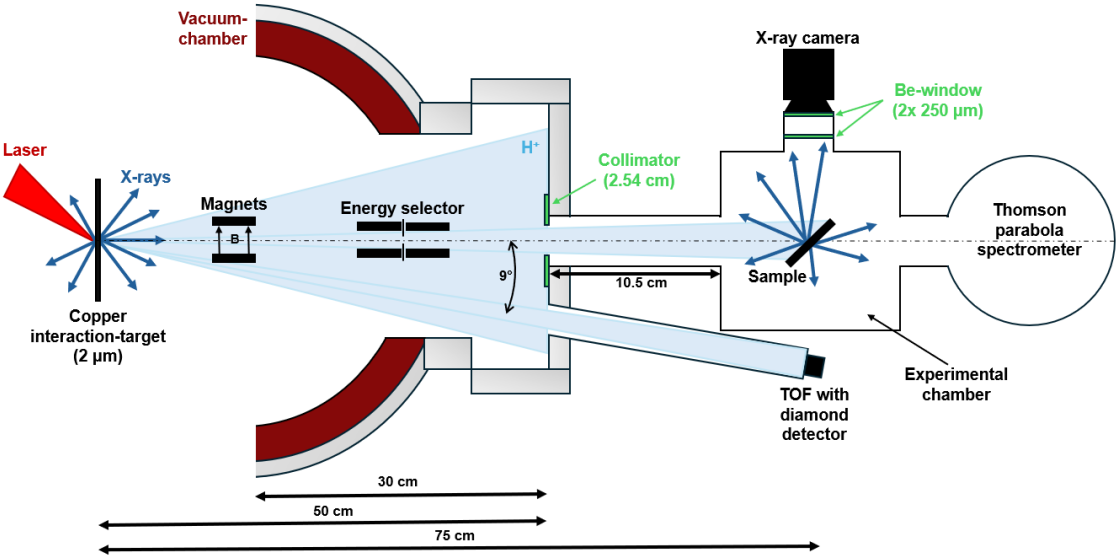

Figure 3.2 Schematic depiction of the main components of the experimental setup shown in Figure 3.1

10 MeV from reaching the experimental chamber. Protons have a larger charge-to-mass ratio and are thereby not affected as strongly by the magnetic field.

Before irradiating a sample, the optical setup is aligned using a red laser, simulating the propagation of the proton beam. After the alignment of the system, the laser is directed into the chamber. The optimization after each shot of the laser beam is done by adjusting the voltages on a deformable mirror inside the compressor. The parameters

are adjusted to achieve a flat wavefront, equalling a Gaussian beam. The wavefront is monitored by a wavefront sensor, quantifying the optical aberrations of the beam as well as a Charge Coupled Device (CCD) camera. Once a set of parameters is found that results in a consistently flat wavefront, the target and sample can be introduced to the setup. After the measurement started, the parameters were not changed anymore during the entire XPIF experiment during this pumping cycle.

3.1.2 Energy selector

The laser-generated proton beam, as produced at the source, can not be used for a layer-by-layer analysis due to the large energy spread of the protons and ions (close to 100%) [67]. The protons are interacting with the entire sample volume, making it difficult to control where the PIXE process takes place and to pinpoint where in the sample a certain element is detected. To select the appropriate proton energies from the continuous spectrum (shown in Figure 3.8), multiple different solutions have been suggested in the past. Some of these solutions require complex preparation of the laser-interaction target [67], utilize gas jets [68,69], or require additional laser beams that trigger small electromagnetic lenses [70], requiring significant changes to the overall experimental setup at the ALLS facility. Other solutions implement external focusing [71,72] and manipulation of the beam by external magnetic fields [73]. This is most often achieved by quadrupoles or solenoids placed between the target and the sample [74]. The use of small coils has also been suggested [75]. However, these methods are more complex in their implementation, requiring large external beam transport lines [76, 77] or complicated target alignment, while the ability to control energy selection additionally proves to be a very intricate task in itself [75]. Due to the limited space inside the main vacuum chamber (depicted in Figure 3.2) and in order to simplify the alignment within our high repetition targetry system, we chose a different method utilizing two sets of dipole magnets. The setup is characterized by its simplicity of implementation and ease of accurately selecting the corresponding proton energies without the need for a complicated setup and calculations.

The ”energy selector” (shown in Figure 3.3) is positioned after the magnets. It is a compact passive device to control the energy bandwidth of the proton beam, making it a perfect fit for the experimental setup, which only has limited space inside the main vacuum chamber. The hardware was designed by Chen et al. at LULI, École Polytechnique [78]. The basic working principle disperses the proton beam in space, after which a setup of slits is used to define the central energy and bandwidth of the beam. Then the beam is redirected to travel again along the same axis as it entered. The device encompasses 4 identical sets of magnets (shown in Figure 3.3), each possessing a magnetic field strength of 1 T. After passing through the first stainless steel slit, which reduces the beam’s divergence and hence unfortunately, also the proton number, the protons

then enter the first set of dipole magnets. These magnets are oriented vertically (in the y-direction) relative to the beam's propagation path. The magnets cause a dispersion of the beam in the horizontal (x-axis) direction. The second set of magnets, immediately after the first one but with opposite polarization, induces another dispersion of the protons; however also guides them back in their original travel direction. The strength of the bending of the trajectory is dependent on the proton energy and governed by the Lorentz force [79]:

$$F = q \cdot v \times B, \tag{3.1}$$

where q is the proton charge, v is the velocity of the charged particle in the direction tangential to its path, and B is the magnetic guide field. The magnetic field causes a separation of protons in the beam according to their energy. Lower energetic protons diverge more compared to higher energy protons. After two magnets, the protons enter through a second slit. The second slit is the part where the beam tuning happens. The slit is made of 3 mm thick tantalum (Ta), ensuring that no unwanted protons pass through, with two stainless steel razor blades forming the actual slit. The position of the slit controls the central energy of the final beam and the slit width manipulates the bandwidth of the beam spectrum. Both parameters are controllable by micrometer screws; however, since the entire setup is put under vacuum, motors are used to adjust the position in between shots. After the final slit, the proton beam enters the third and fourth sets of magnets. They are symmetric to the first four magnets and divert the trajectory of the beam back onto its original path/axis with which it entered the device.

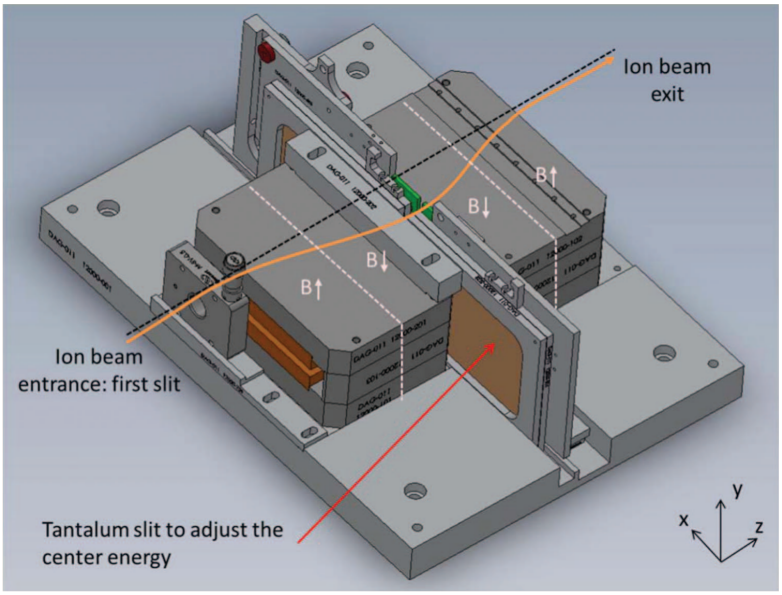

Figure 3.3 CAD drawing of the energy selector showing the orientation of the magnetic fields and the predicted flight path of the ions, extracted from the work of Chen et al. [78].

The selector is designed to be able to tune beams with energies ranging from 100 keV up to 10 MeV and achieves a bandwidth of $\sim 10\%$ of the central energy [78]. While the target of the design was a $\sim$5% bandwidth, factors such as the asymmetric setting of the magnets and the natural divergence of the beam cause a discrepancy from the ideal conditions. It will be shown later, in chapter 4, that the observations made by Sophia Chen et al. [78] can be reproduced on the ALLS beamline at ALLS. This demonstrates the versatility of the proposed method, as the two setups differ in target material, pulse length, focal spot diameter of the laser beam, and numerous other parameters. Figure 3.4

Figure removed due to copyrights issues

Figure 3.4 SIMON simulation showing the proton trajectories between 100 keV and 1 MeV, extracted from the work of Chen et al. [78].

shows a SIMON simulation for proton trajectories of different energies, between 100 keV and 1 MeV. In accordance with Equation 3.1 it can be observed that protons with a lower energy are deflected more due to the Lorentz force. Similarly, it can be seen that since the Lorenz force does not scale linearly with particle energy, the protons with higher energy are bunched more closely together. These observations will be verified in chapter 4, where experimental data of the energy selector will be presented.

3.1.3 Experimental chamber

The samples are mounted in a small auxiliary aluminum chamber. It is connected to the main chamber via a tube made of the same material and has its own separate vacuum ($\sim 10^{-6}$mbar) to reduce the time to change a sample. It is isolated by a 7.5 µm Kapton® window and a gate-valve, which ensures a separation of the vacuum and has a negligible effect on the proton beam. The valve allows venting of the experimental chamber without the need of having to reestablish the vacuum in the large main chamber, a very time-consuming procedure. One side of the experimental chamber, shown in Figure 3.5 is connected to the X-ray camera and separated by two 250 µm thick Beryllium windows. The backside (concerning the beam direction incoming from the right-hand side) leads to the Thomson parabola, whose working principle will be explained in more detail in the next section.

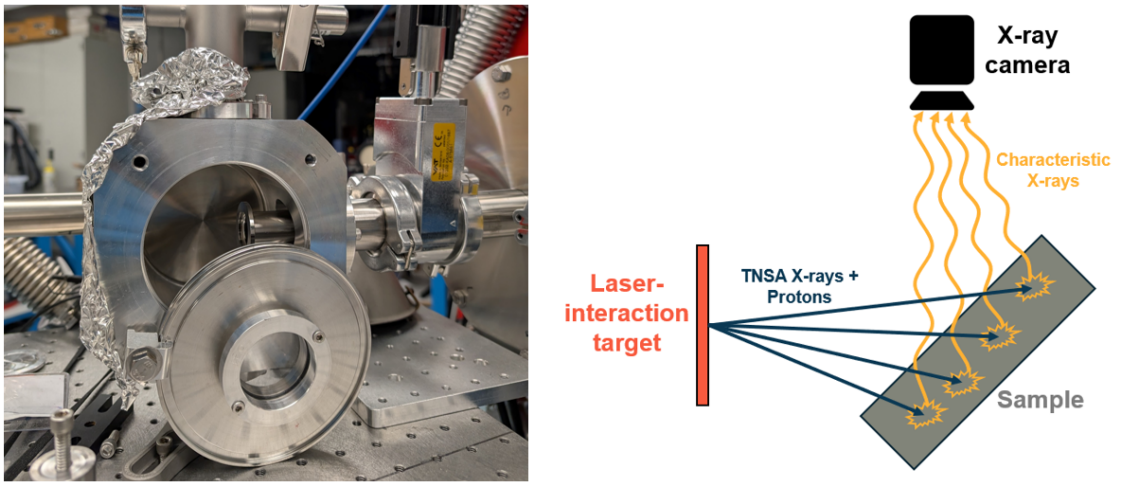

Figure 3.5 Left: Picture of the sample chamber. The top shows the inlet for the gas. Solid samples are mounted in the center using the described method. The X-ray camera for measuring the spectrum is mounted on the window facing towards the viewer. Right: Schematic of the sample orientation in regard to the laser-interaction target and the X-ray camera.

The solid samples are put on an L-shaped holder and secured with a screw. In some cases, special L-shaped samples are used, where no further preparation is needed. After being placed inside the chamber, the samples are rotated such that their surface is oriented at a 45° angle with respect to both the X-ray camera and the incident proton axis. The proton axis is defined by the direction of the proton beam's propagation (i.e., normal to the surface of the laser-interaction target).

When testing aerosols or gas mixtures, the sample preparation is more complex. At the point of writing, only experiments using krypton (Kr) have been performed. However, it is expected that the same procedure also works when using argon (Ar) and other gases. The chamber is first evacuated to a pressure of 10^{-3} mbar, and then gradually filled with Kr using a manual valve. By evacuating the chamber a second time, the desired Kr fraction can be set more accurately. Afterwards, the chamber is pressurized with nitrogen back up to ambient pressure. Kr concentrations were monitored via a Pfeiffer Vacuum gauge, which provides a linear response below 1 mbar [80]. The Kr-to-air ratio was estimated using the ideal gas law and partial pressures [81]:

$$pV = nRT. \tag{3.2}$$

Following the described procedure, a 4% Kr mixture corresponds to a 25% increase compared to the initial pressure. For the lowest Kr concentration ($\sim$ 0.04%), air was used instead of nitrogen, as it naturally contains 1 ppm of Kr [82], enabling more precise low-percentage mixtures.

3.1.4 Diagnostics

Thomson Parabola

There are various laser-accelerated ion beam diagnostics, including radiochromic films, image plates, prompt inline scintillators, and more. in this work a Thomson parabola spectrometer (Thomson Parabola (TP)), invented in 1911 by Thomson [83], is utilized for acquiring the proton spectrum generated by the TNSA process. It enables the acquisition of an almost continuous spectrum with a high repetition rate for a quick analysis. The basic functionality is depicted in Figure 3.6. The setup is able to provide particle distribution, momentum, and mass ratio as a function of energy. It consists of three main components: Parallel electric and magnetic fields, as well as a detector.

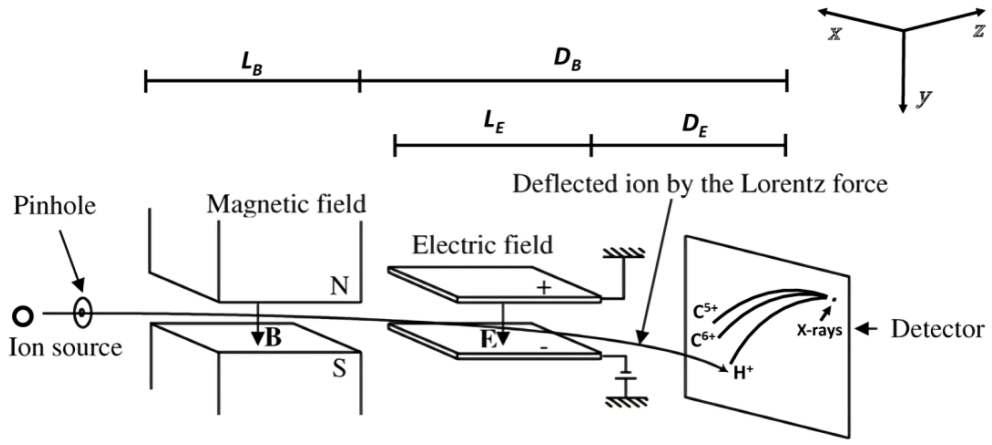

Figure 3.6 Schematic and working principle of a Thomson parabola spectrometer, extracted from Vallieres [40].

The incoming ions will enter through a pinhole and are deflected by the external fields according to the small deflection approximation [84]:

$$x = Ze \cdot \frac{E}{E_i} \frac{L_{B,E} \cdot D_{B,E}}{2}, \tag{3.3}$$

$$y = Ze \cdot \frac{B}{\sqrt{ME_i}} \frac{L_{B,E} \cdot D_{B,E}}{\sqrt{2}}, \tag{3.4}$$

where E_i is the particle energy, L is the length of the electric and magnetic plates, and D is the distance of the plates from the detector. Following Equation 3.4 ions with the same charge-to-mass ratio ($\frac{Z}{M}$) will follow the same parabola in the detection plane (shown in Figure 3.7) and are therefore distinguishable. Particles with a higher energy are deviated less from their original trajectory and stay closer to the center of the detector.

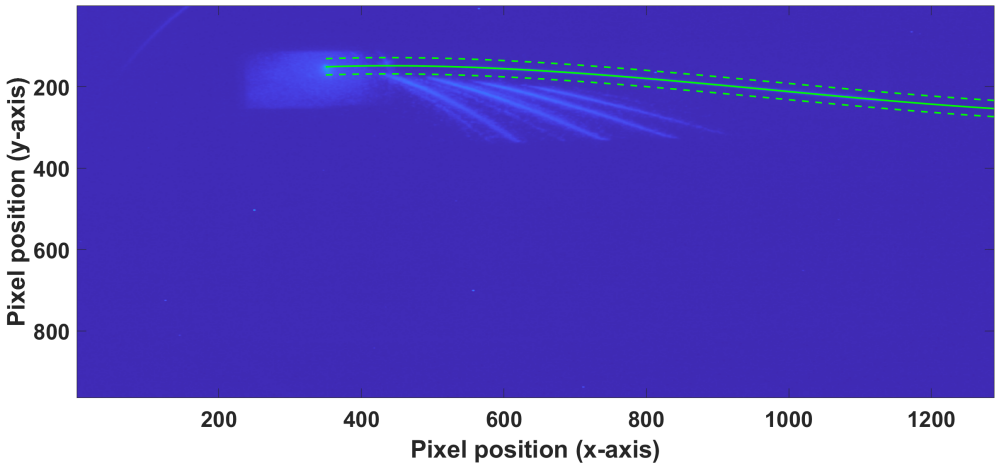

Figure 3.7 Image produced by the TP for a Ta-TNSA target. The different white streaks indicate different ions. The parabola representing the protons is fitted (green) using a *MATLAB* routine to extract the yield. The other four major lines can be attributed to different carbon ions (C^{+2})-(C^{+5})

The code used to generate Figure 3.7 and ultimately the final proton spectrum shown in Figure 3.8 uses the length and form of the proton streak to extract the energy distribution. The streak is fitted using a 3rd-degree polynomial (shown in green). The dotted lines indicate the error margin. The proton count as a function of energy is acquired by interpreting the intensity scaling of the image.

For the detector, a double Micro Channel Plate (MCP) setup for a higher electron yield, combined with a phosphor (P43) screen is employed. The MCP used in the setup was produced by *Photonics* [85], and was calibrated on the Tandem Van de Graaff accelerator from Université de Montréal, as calibration of the detector is essential for a precise measurement. An MCP is a spatially resolved high-gain electron multiplier [84]. The secondary electrons produced by the incoming protons then hit the phosphor screen, producing a photon signal. This signal is then captured by a 13 Megapixel Blackfly PoE GigE camera from *FLIR* [86]. The camera is placed outside the vacuum of the TP and inside a black box to shield it from light pollution. After each laser shot, the CCD signal is sent to the laboratory monitors as shown in Figure 3.7. The entire detection system is placed at a 0° angle compared to the target-normal axis. The combination of a TP with an MCP, phosphor screen, and CCD camera for detection enables a high sensitivity and real-time detection of the proton beam. Being able to analyze the proton yield between each individual shot makes it easy to adjust the laser parameters quickly in order to optimize the proton yield and thereby reduce the number of shots needed to optimize the system before shooting at samples. This is critical since only a limited number of multishot targets are available until the foil is completely used up. The final proton spectrum shown in Figure 3.8 is achieved through multiple shots, which are then averaged. This spectrum is later the basis for the yield calculations, which are described

in more detail in the next section. In this work, two different target elements are used: copper (Cu) and tantalum. Cu was used for the experiments on multilayer samples containing metallic elements, while Ta was used for the investigation of Kr aerosols.

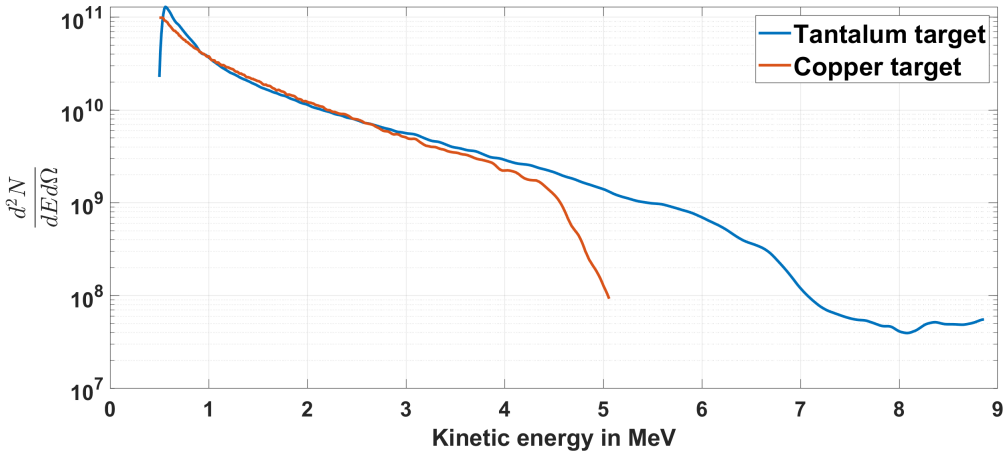

Figure 3.8 Proton spectrum for Ta and Cu accumulated and averaged over 38 and 10 shots, respectively. The error bars were removed for better clarity and lie in the region of ± 15%.

Using a Ta foil results in a 9% higher overall proton yield and higher cutoff energy of around 7 MeV compared to 5 MeV in the case of copper.

Time of flight detectors

To verify the TP measurements, the setup employs a secondary technique to retrieve information on the proton's maximum energy and distribution. Time of flight (ToF) detectors are, besides MCP coupled with a TP, another well-established method to analyze laser-accelerated ion beams. They offer a fast response time, high energy resolution, and radiation hardness. They are especially suitable when the measured protons are much quicker than the other heavy ions (TNSA regime) and when only a single ion species is targeted. Like the TP, they can deliver a proton spectrum on a one-shot basis while also being very compact, making them a perfect addition to the setup [87]. Their working principle is fairly simple. The protons hit the tube at a defined kinetic energy, and the ToF measures the time it takes for an ion to travel through the device. Based on this information and the length of the detector tube, the energy and also the mass can be calculated. However, since only protons are measured, the latter is of no importance to us. The measured ToF can be converted to the ion energy by the well-known equation [88]:

$$E_{kin} = (\gamma - 1)M_p c^2, \qquad \gamma = \frac{1}{\sqrt{1-\beta^2}}, \qquad \beta = \frac{L}{c \cdot ToF}, \tag{3.5}$$

where L is the length of the flight path inside the detector, M_p the proton rest mass, and c the velocity of light in vacuum. In the presented experimental setup (Figure 3.2), two ToF diamond detectors with an active layer thickness of 50 µm on a $4 \times 4 \times 0.5$ mm substrate are employed. Additionally, they are equipped with a CVD-DD camera [40], which in turn is connected to an oscilloscope for data readout. The setup is triggered by the main laser, inducing the TNSA process. They are located at 6° and -9° with respect to the target-normal direction. While both detectors are made of the same material, they have different electrode layouts and therefore different sensitivities for different proton energies. The detector placed at 6° is slightly slower in the response time, but has a more uniform E-field, providing a high efficiency for a wider range. The detector at -9° is well suited for moderate-low energy protons and has a high temporal resolution due to a smaller distance between the electrodes. Using two detectors with different characteristics ensures that there are no systematic errors in estimating the maximum energy or yield of the proton spectrum. A 10 µm Al-filter was placed before the ToF detectors to shield them from heavy ions. The loss of information due to the blocking of low-energy protons was accepted, since the TP is the primary monitoring device. Both detectors are calibrated prior to performing the experiment using Americium as a reference source.

X-ray camera

Over the past two decades, single-photon counting CCD have increasingly shifted their primary role from imaging to hard X-ray spectroscopic applications. This transition is largely due to the high sensitivity and excellent energy resolution of X-ray CCD cameras, which allow for effective imaging and spectroscopy even with very low X-ray fluxes. For the acquisition of the X-ray spectrum, the PI-LCX:1300 X-ray camera, cooled by liquid nitrogen and placed at 90° to the proton beam propagation axis, is implemented into the setup. It is a very popular choice, which later enables a high-accuracy quantitative analysis of the spectroscopy data. The camera has a 1340×1300 pixel array on a 50 µm silicon (Si) chip using 20×20 µm pixels. The PI-LCX:1300 is a front-illuminated camera. The X-rays hit the pixels on the front side and are collected by an array of electrodes, resulting in small charge clouds. The absorption layer is made from 50 µm thick Si. While this setup can theoretically detect X-rays with energies up to 60 keV, it to only considered to have a reasonably good detection efficiency between 2.5 and 20 keV, as shown in the quantum efficiency curve in Figure 3.9 [89].
The pixel setup of the CCD chip provides high spatial resolution. It is separated by a beryllium window (thickness 250 µm) which seals the chip away for better cooling efficiency. It also reduces background noise by filtering out low-energy photons. Including the second Be window (placed ∼4 cm in front of the camera), they transmit around 96% of the X-rays at 12.6 keV [90], which equals the K_α of Kr, which lies roughly in the

middle of the acceptable detection range. At the same energy, the X-ray detector offers a resolution of 0.222 keV calculated according to [91]:

$$\Delta E = 2.35 \cdot 3.65 \sqrt{N^2 + \frac{F \cdot E}{3.65}}, \tag{3.6}$$

with F being the Fano factor [92], N the readout noise, and E the energy. The calculations are based on the statistics of pair creation in a Si detector. The calibration procedure of the camera will be described in a later section of this chapter. The final spectrum, which gets analyzed by the *MATLAB* code, is then accumulated over multiple laser shots and saved on a laboratory PC.

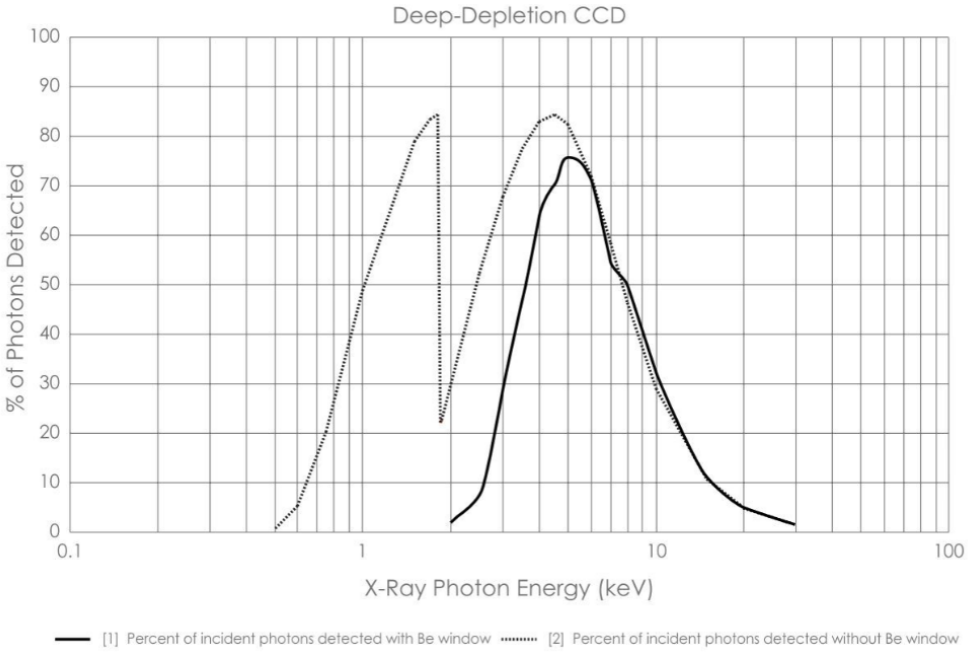

Figure 3.9 Percentage of photons detected by the PI-LCX:1300 camera for different energies, extracted from the datasheet [93]. The solid line takes the absorption by the beryllium (Be) window into account. Between 2.5 and 20 keV, the camera efficiency lies above 5%, which is considered acceptable for the XPIF experiments.

3.2 Methodology

This section will explain the main components of the custom-written *MATLAB* routine developed for both general quantitative analysis and specialized multilayer analysis. The basis of the code was initiated by Bovin et al. in 2022 [2] and was used to test homogeneous samples irradiated with a continuous proton spectrum.

While this method can be used to extract the elemental composition of the entire sample, it does not take advantage of the distinct characteristics of proton energy deposition in

matter, described in chapter 2. The existing routine can only be used for measurements utilizing a copper laser-interaction target and is limited to a few selected elements, which were of interest in previous experiments. To enable multilayer measurements on a layer-by-layer method, an extensive expansion of the original *MATLAB* code is necessary, along with the aforementioned implementation of the energy selector. Given the planned experiments, the new *MATLAB* routine needs to be able to work with different kinds of incoming particles (X-rays and protons). It also needs to work with different measurement techniques, namely layer-by-layer with narrow proton spectra or an irradiation of the entire multilayer sample using a continuous spectrum. Hence, the complexity of the calculations increases significantly.
Therefore, in this thesis, a new routine to achieve multilayer analysis was developed and implemented into the original code. Additionally, some code clean-up, rework, and bug fixing were performed. Since the procedure to analyze multilayer samples will consist of multiple measurements, a method was created that will loop over all presented measurements, taking the results of the first layers as a basis for additional attenuation and yield calculations for the next layer. The yield calculations consist of the yield produced by PIXE and XRF as well as diffraction of the incoming X-rays into the detector. The procedure was designed so that it can work with both a full continuous proton spectrum (as shown in Figure 3.8) as well as the narrowed-down spectra produced by the energy selector. Since multiple layers consisting of different materials and composites increase the possible elemental combinations, a system using look-up tables has been implemented. The implemented additions make the code more versatile and readily scalable, laying the groundwork for the addition of more elements and targets for future experiments.
However, before going into the details of the *MATLAB* code, the difference between qualitative and quantitative analysis of samples is briefly explained to establish a foundational understanding of the experimental and analytical goals of this work.

3.2.1 Qualitative and quantitative analysis

Qualitative and quantitative analysis serve distinct objectives, with the latter often presenting greater complexity. Qualitative analysis primarily aims to identify the constituent elements within a sample and represents an essential requirement for conducting quantitative analysis. In the case of XPIF, the recorded spectrum in the form of characteristic X-ray $K_{\alpha,\beta}$ lines, is used to find the fingerprints of each element.
The main difficulty that arises from this task is the differentiation between overlapping peaks. The K_β peaks can be overshadowed by stronger K_α peaks from another element. On the other hand, if the sample for example contains trace elements of iron (Fe) and huge amounts of Manganese (Mn), the Mn K_β lines (5.887 keV) can overshadow the Fe K_α (6.403 keV) information. It is also possible for the L-peaks of heavy elements to get dominated or drowned by K_α lines of light elements in the same sample. Therefore, the

detector's energy resolution critically influences the range of samples amenable to analysis. While the analysis of entirely unknown samples remains feasible, prior knowledge regarding the potentially present elements significantly streamlines the identification process. To distinguish and analyze overlapping peaks, fitting algorithms using the Gaussian function and reference measurements of pure samples are used [9].
The main goal of quantitative analysis is to precisely determine the concentration or amount of identified components within a sample, making its implementation much more complex. The calibration using samples with reference standards is a requirement for performing this kind of analysis. In this thesis, calibration of the camera was performed using the elements titanium (4.51 keV), nickel (7.48 keV), copper (8.05 keV), zinc (8.64 keV), niobium (16.62 keV), molybdenum (17.48 keV) and argon (22.16 keV) [90]. The samples have a purity of 99.99% (produced by *Goodfellow*) and are irradiated with the same proton/X-ray source used for the experiments. The reference measurements are used to perform a linear regression fit, which is later applied to the data. In total, a lot more information on the sample and the setup is needed for an accurate estimation of the sample's chemical composition. Additionally, different effects such as diffraction, escape peaks, and pile-up events, which are described in more detail in the next section, need to be taken into account. The *MATLAB* code presented in this chapter aims to perform both types of analysis.

3.2.2 Data analysis using *MATLAB*

The basic procedure of the code routine written in *MATLAB* takes three inputs: The measured characteristic X-ray spectrum of the sample, the proton and X-ray yield from the TNSA process and the sample as well as the setup parameters. The experimental parameters include: Thickness, area, and orientation of the sample relative to the proton beam axis, attenuation of the Be windows, the camera efficiency, and solid angle of the proton beam. The basic working principle of the code is shown in Figure 3.10.

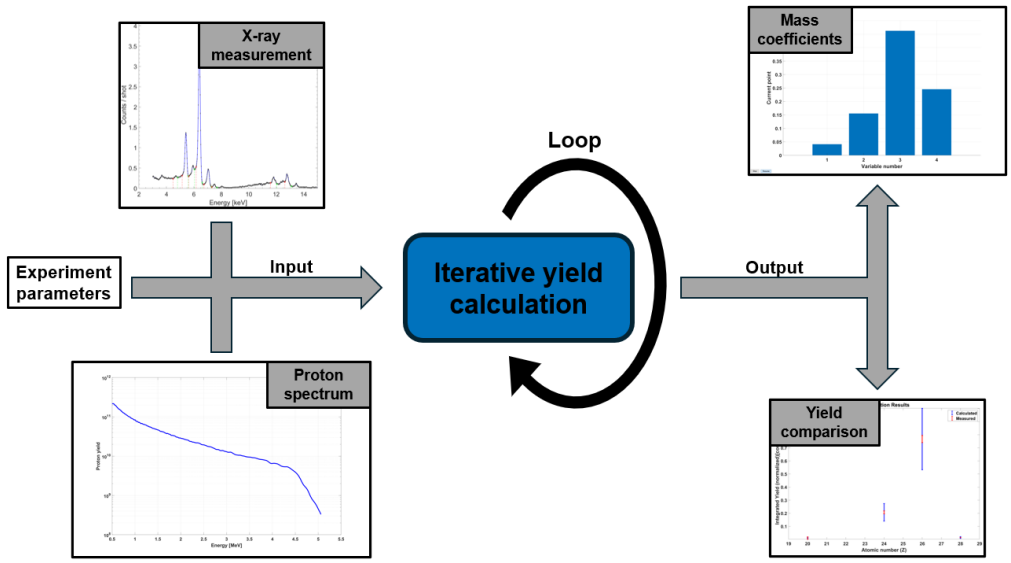

Figure 3.10 Schematic of the custom-written *MATLAB* code depicting the input and output of the procedure

Before going into the details of the important steps, a quick overview of the different building blocks of the code is given. First, the measured X-ray spectrum has to be read in. Besides the spectrum, the code also requires information on the setup as well as the proton spectrum and the X-rays produced by the TNSA. The data will then be analyzed for which elements are contained in the sample, and the theoretical yield based on the input parameters will be calculated for each found element. The code employs an iterative procedure to optimize a loss function based on the previously introduced mass ratios and the normalized yields, to find an optimal set of parameters that best describes the experimental data. In the case of multilayer analysis, the basic calculations are repeated in a loop going through the sample layer by layer, with additional calculations taking into account the different kinds of interactions of the protons and phonons with the material above the layer under examination. In the end, the user will be presented with the mass ratios and a comparison of the theoretical and measured normalized yields. The latter indicates the quality of the calculations compared to the experimental data.

Data processing of the X-ray camera

As previously stated, the X-ray detector delivers a 1300×1340 image with 16-bit grayscale values. These values need to be converted back into the intensity as a function of energy. Figure 3.11 shows the input and result of this conversion.

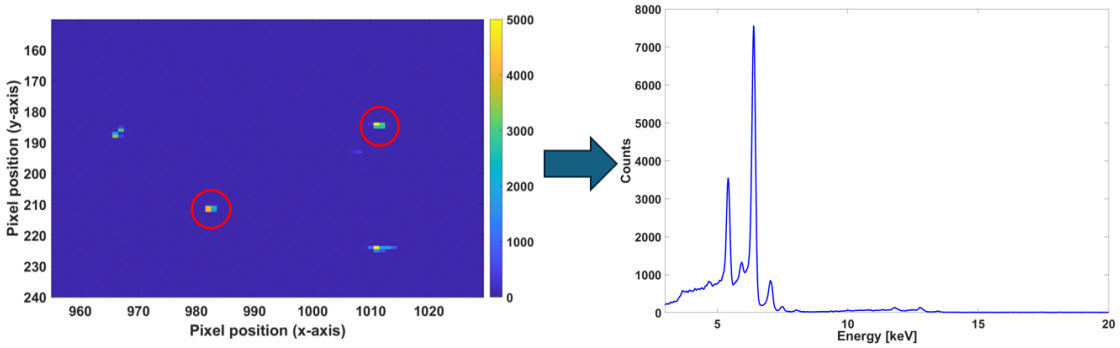

Figure 3.11 The right-hand side shows a snipped from the recorded CCD camera image, which is converted into an X-ray spectrum shown on the left. Marked in red are two examples of what is not considered an Single Pixel Event (SPE) since the incident pixels are too close together.

First, an ".SPE" (X-ray Spectrum) file containing the spectroscopy data recorded by the *Princeton Instruments* X-ray camera, along with a file containing the background noise get read out by the code. The background is typically measured over multiple seconds to get a good estimation of the average noise level. Its signal then gets adjusted for the measurement time and subtracted from the main camera file. Afterwards, the data gets filtered using the Single Pixel Event (SPE) algorithm, not to be confused with the file extension. The algorithm is described in detail by Fourment et al. [94] and Fourmaux et al. [95]. The algorithm looks at a photon hitting a single pixel of the camera and compares the value to the surrounding pixels (3x3 matrix). However, the code only considers directly adjacent pixels since the contribution by the corner pixels is below 1% [2]. If the pixel is not adjacent to another illuminated pixel and its value is greater than the threshold defined by Equation 3.7, where $\overline{Y}_{background}$ is the mean background signal, the pixel is considered a "true" event:

$$\text{threshold} = \overline{Y}_{background} + 3\sigma. \tag{3.7}$$

Utilizing this algorithm results in an improved photon energy resolution [94]. However, it comes at the cost of a reduced overall photon count, which has a negative impact on the photon statistics. After filtering, the grayscale value is converted into the information on photon energy by using the calibration data described in section 3.1.4. The

transformation is done according to Equation 3.8 [95]:

$$\frac{dN}{dE} = \frac{a}{k_1(E) \cdot QE(E) \cdot T(E) \cdot \Omega_c} \frac{dN_{SPE}}{dE}, \tag{3.8}$$

with $QE(E)$ and Ω_c being the quantum efficiency and solid angle of the camera, $T(E)$ the transmission of the Be window, and $k_1(E)$ the probability of SPE being detected from one single photon. a is a dimensionless parameter that ensures that the amount of SPE counts is the same as the total amount of detected events. It usually ranges between 1 and 3.

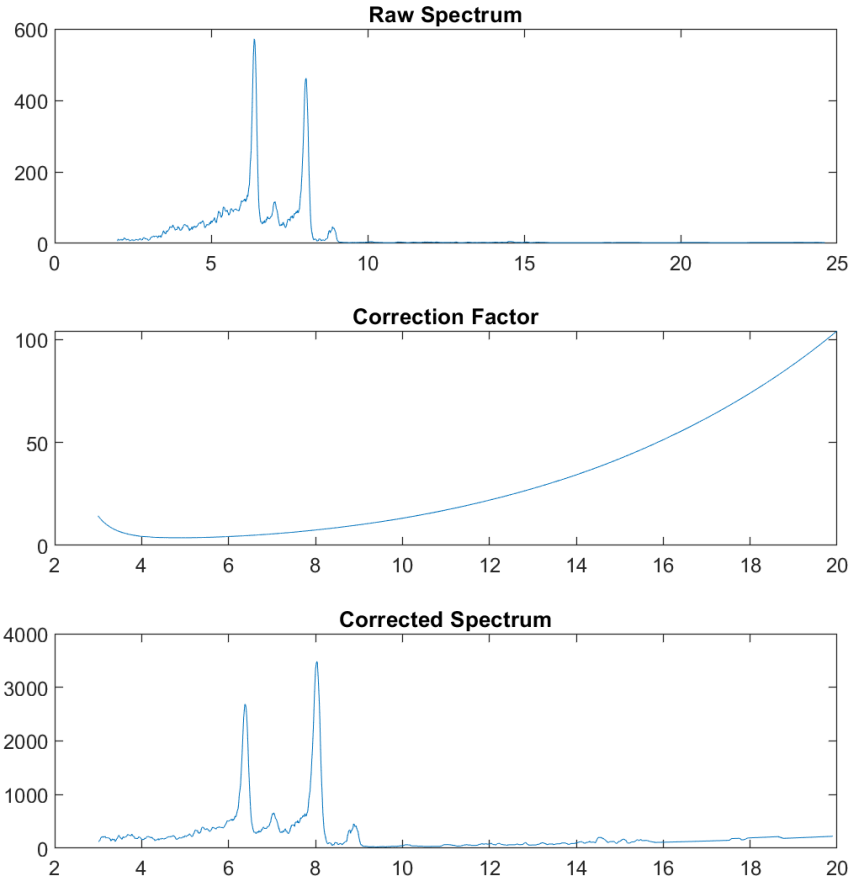

Figure 3.12 The optional correction curve which gets applied to the measured X-ray spectrum, taking into account camera efficiency, SPE probability, and attenuation of the Be window and camera sensor

Before the automatic filtering, the user also has the option to manually delete iron or chromium (Cr) K_α lines, which can be the result of specific sample holders or the chamber windows. It is also possible to choose between the analysis of a ”raw” and ”corrected” spectrum. The ”corrected” spectrum applies a curve to the measured spectrum (seen in Figure 3.12), which corrects for the camera efficiency, attenuation of the Be window and

camera sensor, as well as the SPE probability. Additionally, the spectrum gets cut down to the aforementioned acceptable energy range.

The peaks in the obtained spectrum, as shown in Figure 3.11 (right-hand side), now need to be associated with the corresponding elements. This is done via a simple comparison procedure of the peak location to recorded values from the X-ray Booklet database [90]. The analysis gets more complicated when X-ray lines of multiple elements in the sample are close together and overlap and/or cover the K_β information. An extreme example of this would be the K_β of titanium at 4.93 keV and the K_α line of vanadium (V) at 4.95 keV. The difference between the peaks is below the resolution of the X-ray detector mentioned in section 3.1.4 and can thus not be differentiated. Other common sources of misinterpretation are escape peaks and pileup events, which can be mistaken for peaks in the spectrum. An escape peak happens when the energy from an incoming X-ray is lost due to the escape of a characteristic X-ray generated within the detector itself. In this case, it means that a Si K_α transition is excited and the spectrum will show two additional peaks: The first one being at 1.7 keV [96] (not detectable with the current X-ray camera) and the second one at $h\nu$ minus the mentioned 1.7 keV. Compared to that, a pile-up event (also known as a sum peak or coincidence peak) is an artifact that occurs when two or more X-ray photons arrive at the same pixel nearly simultaneously, so close in time that the detector's processing electronics cannot distinguish them as separate events. Instead, it registers them as a single, higher-energy event. The last source of misinterpretation is the previously discussed elastic scattering of the laser-interaction target's characteristic X-rays. This can lead to the assumption that trace elements of the target element like copper are present in the sample, even though in reality this is not the case. Every record peak gets checked for potential overlaps by looking at tabulated values and verifying the existence of K_α peaks if a K_β peak is found, and the yield relation ($K_\alpha > K_\beta$) holds true. To lower the chance of a misidentification of peaks, the code only checks for elements that have characteristic X-ray lines of the K-shell within the camera's detection range. If a pileup event is detected at twice the energy of a detected element, the amount of simultaneous events on the same pixel is added to the integrated yield of the corresponding peak (explained in further detail in the next section). This same principle applies in the case of a detected escape peak.

To calculate the integrated yield of the characteristic K_α peaks, each identified peak is fitted with three different functions: Gaussian, Lorentzian, and Triangular. The fitting procedure is performed using a non-linear least-squares method. The uncertainty in the resulting fit parameters is determined from their 68% confidence interval, which corresponds to one standard error σ. If none of the three functions yield a satisfying fit, the peak is integrated using the *trapz*-function in *MATLAB*. The background under the peak is estimated using integration between the FWHM limits of the fitted function, as shown in Figure 3.13.

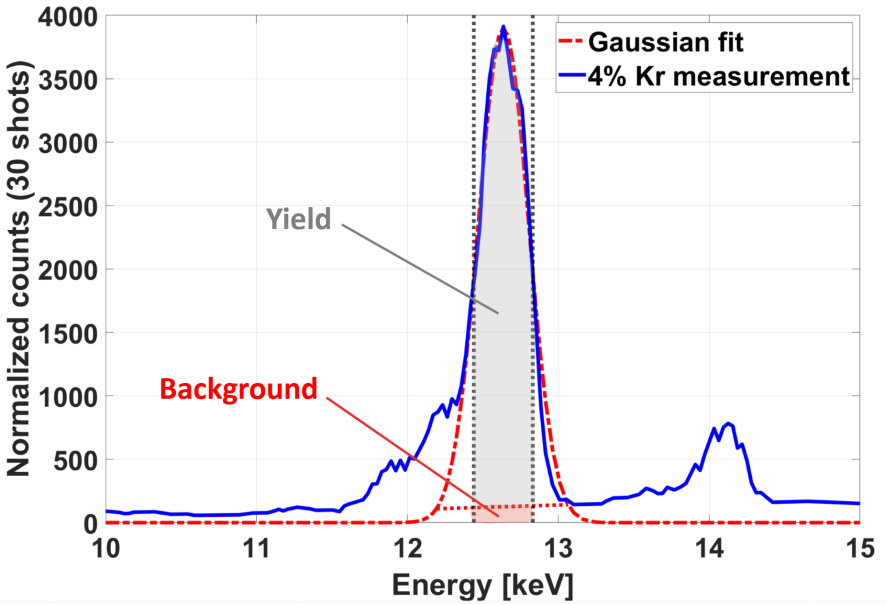

Figure 3.13 Gaussian peak fitting (red dotted line) of a Kr K_α measurement (blue). The area within the FWHM (dotted black lines) defines the yield (gray area) and the background (red area), based on the noise of the measurement.

After the initial filtering of the photon count data, each identified spectral peak must be validated as a characteristic X-ray line. To ensure the correctness of the peaks within the spectrum, the code utilizes the Minimal Detectable Limit (MDL) method to define a threshold after which a peak is considered a characteristic X-ray line. Otherwise, the peak can not be statistically associated with the corresponding element and is just considered background noise. Typically, the minimal detectable yield (area under the peak) under a peak is defined as [97]:

$$Y_{MDL} = 3 \cdot \sqrt{Y_{background}}, \tag{3.9}$$

where Y_{MDL} is the minimal detectable yield. The background yield ($Y_{background}$) is defined within the FWHM of the peak, which is related to the standard deviation of a Gaussian curve via: FWHM $= 2.35 \cdot \sigma$ [57]. If the sum of Y_{Peak} and $Y_{background}$ is higher than Y_{MDL}, the peak can be considered a verified K_α peak. Following the automated filtering and identification procedure, the user is given the option to manually delete or correct the identified peaks based on any prior knowledge of the sample. They can also confirm if the automatic assessment of a potential elastic diffraction peak from the laser-target is correct and should be excluded from the analysis.

Procedure for yield calculation

At the beginning of the program, the user can decide which part of the proton spectrum they want to use, based on the setting of the energy selector. The intensity of the co-

produced characteristic X-rays from the laser-interaction target is input as a single input value representing the photon count at the K_α and K_β energies. As stated in chapter 2, the fundamental parameter method (FPM) [9] is used to calculate the theoretical X-ray yield of the sample. Although it's not as precise as other empirical methods, such as internal standardization [9] (which uses reference standards for elemental analysis), this technique allows for the analysis of samples with entirely unknown compositions. This is especially useful for initial investigations of samples that require quick and precise results without any complicated sample preparation, which consists of altering the sample's surface or geometry [98]. For the analysis, only the K_α line of all detected elements needs to be considered. Even though K_β lines are detected in the identification process, they are not required for a sufficiently accurate material analysis. The K_α lines provide all the necessary parameters for calculating yield based on the mass ratios. The impact of secondary fluorescence is also not yet considered in the code calculations. Compared with the shot-to-shot fluctuations of the laser source, its effects are currently seen as negligible [96]. However, once these restrictions have been improved, the implementation of secondary fluorescence into the yield calculations is planned as it can potentially improve the accuracy of the analysis.

For the analysis of the material, an iterative procedure adjusts the mass ratios used for the yield calculations (as described in detail in chapter 2) in each iteration to minimize the loss function shown in Equation 3.10. As a starting point, an equally distributed concentration of all identified elements with a present K_α line in the spectrum is assumed. Afterwards, the mass ratios are used to calculate the theoretical yield of the sample. After summing up the yield from both the X-Ray Fluorescence (XRF) and Particle-Induced X-ray Emission (PIXE) contributions for all elements, the result is normalized (according to $Y = \frac{Y_i}{\sum_i Y_i}$) and used as the input for the optimization procedure. Finding the optimal parameter set is done utilizing the *fmincon* function integrated in *MATLAB* and comparing the normalized theoretical yield $Y_{theoretical}$ to the normalized measured yield $Y_{measured}$. For the loss function, the standard χ^2 parameter is defined as:

$$\chi^2 = \sum_i \frac{(Y_{measured} - Y_{theoretical})^2}{Y_{measured}}. \tag{3.10}$$

The best fit for the experimental data is found when χ^2 lies below 10^{-10} for two iterations in a row, providing sufficient precision while still providing a reasonable computation time (especially when multiple layers are analyzed). The set of mass ratios is restricted to: $0.8 < \sum_i w_i < 1$. These limits are chosen based on the assumption that while the identified elements constitute the majority of the sample, other elements may be present that cannot be detected with the current X-ray setup. These primarily include light element impurities such as hydrogen, oxygen, and carbon, but also aluminum and silicon. If the concentration of a non-detectable element in the sample is too high, a

quantitative analysis is not possible anymore due to a lack of information. An example of this is the carbon concentration in wood samples. Therefore, it is determined that the sum of all mass ratios c_i has to lie between 0.8 and 1, and the optimization process decides the optimal set of parameters.

The progress of this iterative procedure is visualized for the user in the form of bar graphs. After the completion, the results for all c_i are presented along with a comparison between the theoretical and measured normalized yields, as shown in Figure 3.14. The comparison indicates the goodness-of-fit between the model and the experimental data.

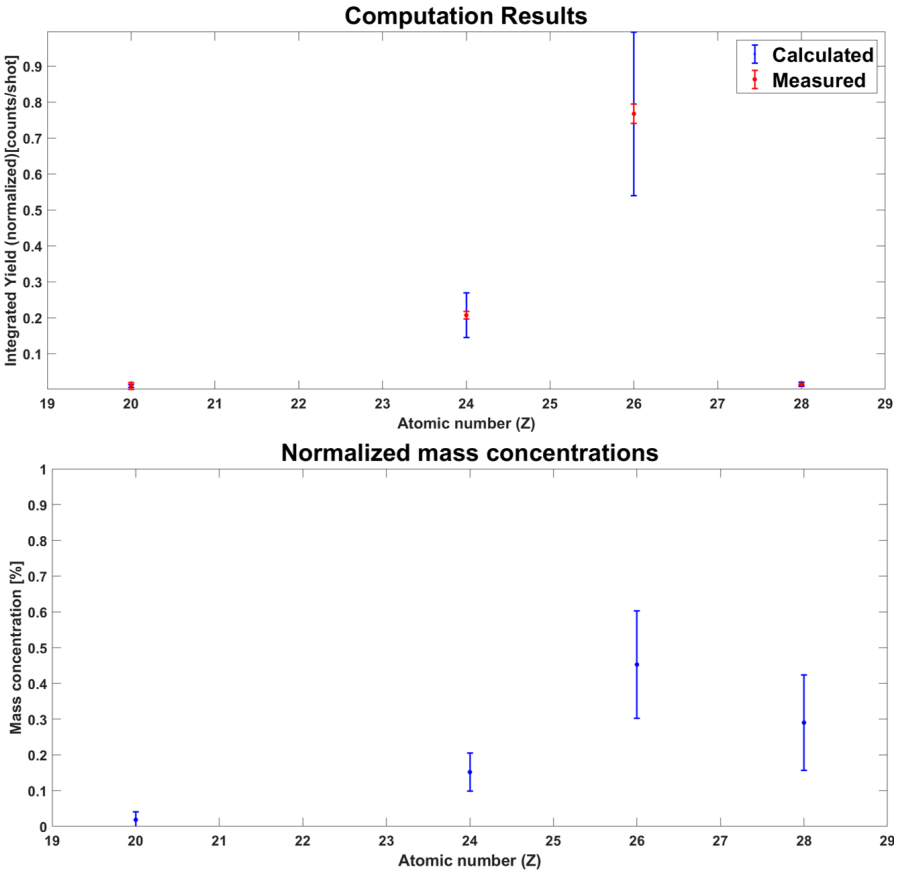

Figure 3.14 Results of he *MATLAB* computation routine for a stainless steel sample. The top graph depicts the comparison of the measured and calculated normalized yields. While the error of the calculations is higher than the yield estimation based on the experimental data, the fit yields a perfect match in every case. The bottom graph shows the normalized mass coefficients c_i of each element in the sample.

As previously stated, the setup exhibits shot-to-shot fluctuations of both the proton yield and the X-ray yield produced by the TNSA. To account for these effects, two parameters are introduced in the code. Parameter a ranges from 0.75 to 1.25, quantifying the proton fluctuations, and parameter $0.85 \leq b \leq 1.15$, representing the X-ray fluctuations. Both

are implemented by being multiplied by the corresponding physical object during the yield calculations. They are changed in increments of 0.05 inside a nested loop, which contains the *fmincon* function. The results are compared based on the relative root mean square (RMS) error with respect to $a = b = 1$. Even in the worst-case scenario ($a = 1.25$, $b = 0.85$), the average error was 16%, suggesting the mass coefficient calculations are not highly sensitive to cumulative errors from the source [2].

3.2.3 Implementation of layer-by-layer analysis

The procedure described thus far was originally designed for homogeneous bulk samples irradiated by the entire proton spectrum. In order to accurately analyze samples composed of multiple layers or to perform a layer-by-layer analysis, the code requires modification. The interactions of incident and emergent protons and X-rays within the different layers significantly alter the measured yield and must therefore be calculated accurately. For protons, the primary point of interest is their energy deposition in the different layers. When traversing the first layer, protons lose part of their kinetic energy in an amount dependent on their current energy, while simultaneously generating an X-ray yield inside the sample. The initial step involves calculating the energy deposition in the top layer, resulting in an attenuated spectrum. Figure 3.15 schematically illustrates this process for a 10 µm thick copper layer with a bulk of titanium underneath.

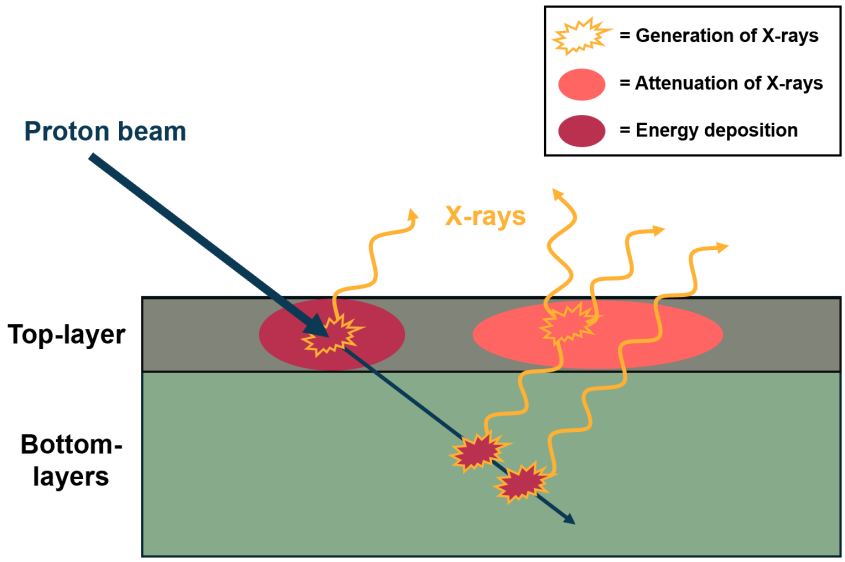

Figure 3.15 Schematic representation highlighting all relevant interactions of incoming protons and outgoing X-rays with the sample. The schematic only shows two layers. However, the concept can be scaled to any number of layers.

In the simplified case of Figure 3.15 the sample gets separated into two parts. By calculating the predicted range of the protons in the top layer material, the *MATLAB* code can differentiate the part of the spectrum that deposits its entire energy in the top layer.

After separation, the thick PIXE formalism, described in chapter 2, is applied to this part of the spectrum, while the thin PIXE formalism is used for the remainder of the spectrum, since only a fraction of the incident particle's energy is lost. For the bottom layer, the thick PIXE formalism is applied using the proton spectrum corrected for energy deposition. The attenuation in the bulk is accounted for in the yield calculations introduced in chapter 2.

For X-rays, the attenuation of the produced X-rays in the bottom layer and the elastic diffraction of the incoming beam must also be considered. All relevant processes are highlighted in the schematic shown in Figure 3.16. Before the XRF yield of the top layer can be calculated, the percentage of incident X-rays diffracted at the surface must be determined. The number of diffracted photons and the resulting yield detected by the camera are calculated according to the methods described in chapter 2. It is important to mention that the calculations are based on information on the chemical composition of the first layer. Therefore, preliminary measurements are necessary to obtain the required information on the multiplicity, the structure factor, and the lattice constant. The remaining X-rays are used for further calculations of the XRF yield.

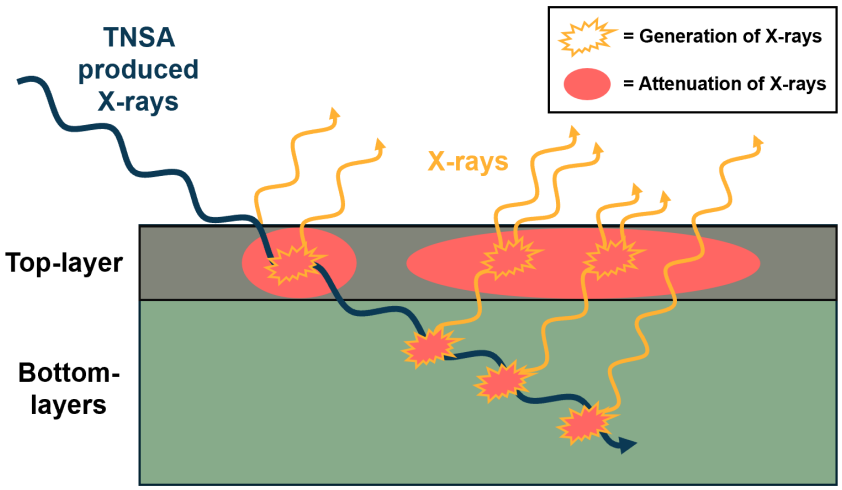

Figure 3.16 Schematic representation highlighting all relevant interactions of incoming and outgoing X-rays with the sample.

If the energy loss of the incoming X-rays is $\leq 5\%$ the XRF thin target formalism gets used. Otherwise, the thick target formalism is applied. Following the calculation of the yield for the first layer, the attenuation of the X-rays by the top layer is determined using the Beer-Lambert law and Bragg's additivity rule. The information on the mass attenuation coefficients is well documented in literature [28]. However, the code employs a *MATLAB* package called *PhotonAttenuation* written by Jaroslaw Tuszynski for the calculations due to the ease of implementation. It returns the reduction in intensity based on the element and thickness of the sample, as well as the incoming photon energy.

In the case of the presented two-layer sample, the reduced photon count and the thick PIXE formalism are then used to calculate the yield in the bottom layer. Looking at the bottom layer, to calculate the correct mass concentrations of the targeted area inside the sample, the yields of the layers above are added on top of the yield of the bottom layer. The mass concentrations are then adjusted, taking into account all contributions by all layers for the next iteration. This process is shown schematically for two layers in Figure 3.15 and Figure 3.16, but can be scaled to any number of layers. The coefficients of the top layers are not adjusted during this iteration procedure since their chemical composition has already been determined.

The produced characteristic X-rays of the sample's bottom layer will again interact with the top layer on their way to the detector. Since the X-ray radiation is distributed isotropically in all directions, the camera solid angle is important for the calculations. For the outgoing X-rays, two different processes have to be considered: Attenuation and secondary fluorescence. The effect of attenuation can significantly reduce the yield of X-rays. As an example, a 10 µm copper layer already reduces the photon count by 99% of characteristic Ti X-rays. Secondary fluorescence only happens if the X-rays have sufficiently high energy to excite the electrons in the top layer. In the same case, the Ti X-rays ($K_\alpha = 4.51$ keV) are not energetic enough to overcome the binding energy of Cu with 8.04 keV.

For samples with more than two layers, the process of calculating attenuation, energy deposition, and evaluating whether the thick or thin yield formalism has to be used has to be repeated for each layer. In a three-layer sample, for instance, incoming and outgoing X-rays are attenuated twice before reaching the bottom layer or the detector. The same principle applies to the deposition of proton energy.

To analyze multilayer samples, the previously described code was modified. In the beginning, the user has to choose how many layers the sample contains and the corresponding thicknesses. Afterwards, the code will perform the calculations for every layer starting from the top layer, with the user choosing the corresponding ".SPE" (X-ray Spectrum) file and proton spectrum. The results of the first loop are then saved and used for the attenuation calculations of the following spectrum until the final layer is reached. Theoretically, this enables us to measure an infinite number of layers. However, the penetration depth of protons and X-rays is limited, resulting in measurements of typically up to four layers. This is because at one point the attenuation of incoming/outgoing X-rays and protons is too strong, so that no signal can be detected anymore, and/or the incoming particles won't reach the desired depth in the first place. The information on the layer thickness and size is needed in every iteration. The user also has to validate the peak identification for each layer.

Notably, the aforementioned calculations for any overlying layers rely on their chemical composition and thickness. The procedure, therefore, requires this information to be

available at the start of the analysis process. However, as previously stated, the goal of the XPIF technique is the analysis of completely unknown samples, where this information is gathered sequentially, layer by layer. To resolve this apparent contradiction, the following measurement procedure was implemented: First, the sample's layer thicknesses must be determined. If no prior information about the sample is available, a scan is performed by varying the position of the energy selector. By gradually increasing the central energy of the plateau in the proton spectrum, the peaks in the X-ray spectrum are observed to change. As the probe depth is increased, some peaks will disappear while others emerge from the background noise. From this process, an initial estimate of each layer's thickness can be obtained. While this method does not yield precise thicknesses, the information is considered sufficient to target the proton probing depth to the approximate center of each identified layer, thereby reducing unwanted excitation of characteristic X-rays in adjacent layers. However, having the required information beforehand significantly reduces the measurement time and increases the accuracy of the process. Once the user has acquired the thickness information of the sample, using the calibration data of the selector, the corresponding slit position can be chosen in order to probe the different layers. This process yields the chemical composition of each individual layer. If no layer-by-layer method is used, and the entire sample is irradiated with the continuous proton spectrum, the user still can enter the top layer information manually, including the elemental composition and mass ratios of the layer as well as its total thickness. Afterwards, the routine will proceed in the same way as if the layer-by-layer method with different selected proton spectra is used.

3.2.4 Modelling of the Bremsstrahlung spectrum

As mentioned in chapter 2, when using copper as a laser-interaction target, the excitation due to Bremsstrahlung is neglected due to the small cross-section compared to the characteristic X-rays of copper. However, when using a target with a higher atomic number, the generated Bremsstrahlung cannot be neglected anymore. To accurately estimate the XRF yield in the sample, additional calculations are required. For Ta, it is estimated that roughly 50% of the generated X-rays lie in the continuous spectrum, with the other 50% being contained in the characteristic radiation. Since only the K_α and K_β yield were measured, the energy distribution of the continuous spectrum has to be reconstructed.
As a starting point, the electron number produced by the TNSA process is estimated by using the measured proton spectrum and the charge neutrality of the ion beam [99]. Charge neutrality means that the proton beam must be compensated by the co-moving electron bunch. Dividing the proton spectrum (shown for Ta in Figure 3.17) by the mass ratio of protons and electrons and integrating yields the total electron number. The energy of the hot electrons inside the target foil can be estimated by calculating the second derivative (slope) of the proton spectrum [100]. Using this technique, a hot

electron energy of 915.8 ± 15.5 keV is obtained. This value is consistent with findings from previous experiments and simulations performed under similar conditions [101,102].

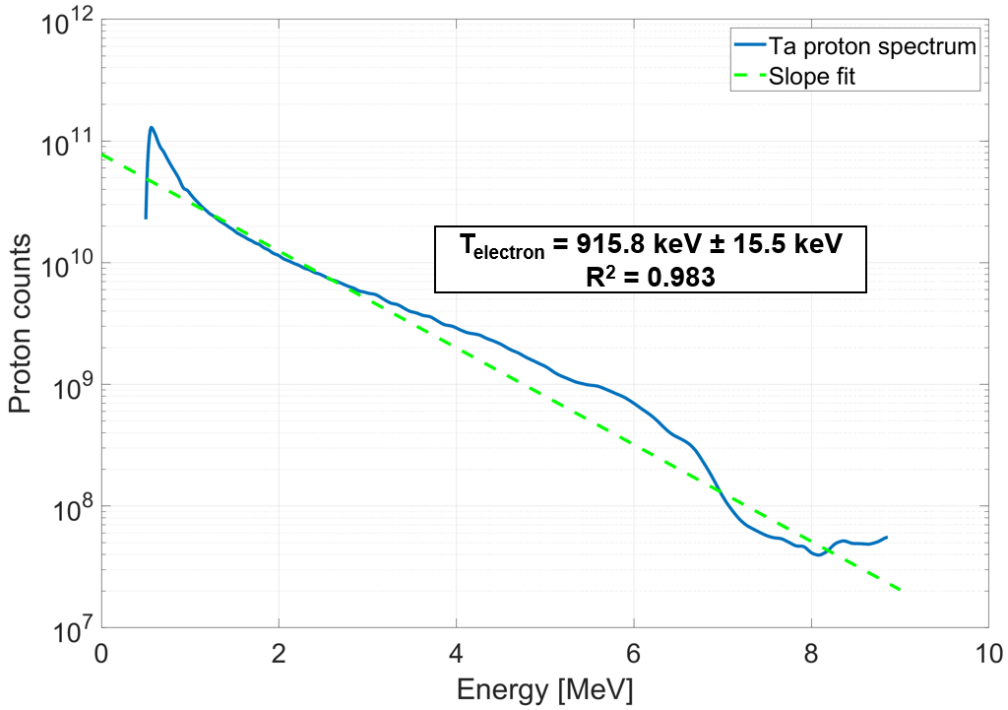

Figure 3.17 Fit of an exponential function (green) to a Ta proton spectrum (blue) to estimate the hot electron energy inside the laser-interaction target. The slope of the fit in a semi-logarithmic representation results in an energy of 915.8 ± 15.5 keV with an R^2 of 0.983.

The total photon energy due to Bremsstrahlung is calculated using the radiation yield [27]. As a first approximation of the electron distribution during the TNSA process, the well-known Maxwell distribution as it is commonly used in this context is employed [103,104]. However, the electrons in this energy range are subject to recirculation, which will cause a deviation from the Maxwell distribution [103,105]. In these cases, the distribution can be described by other functions such as the Maxwell-Jütter or a bi-Maxwellian distribution function. For a first approximation, the normal Maxwell distribution is sufficient since the lower energy part dominates the Bremsstrahlung yield [36, 105]. The normalized probability density function is calculated between zero and the hot electron energy:

$$f(x) = \sqrt{\frac{2}{\pi}} \frac{x^2}{a^3} e^{\frac{-x^2}{2a^2}}, \tag{3.11}$$

with a being the distribution parameter. The result of the reconstruction is shown in Figure 3.18.

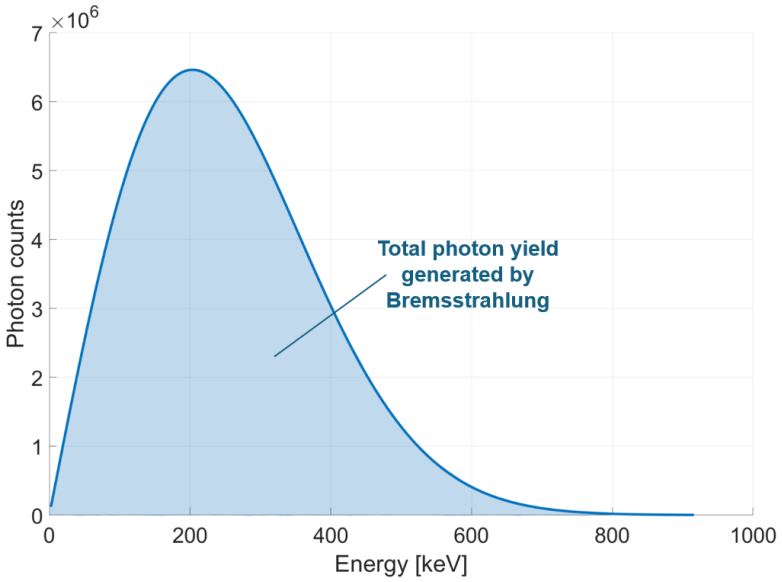

Figure 3.18 Calculated Bremsstrahlung for Ta, based on the proton spectrum (Figure 3.17) and the assumed Maxwellian distribution described in Equation 3.11.

Estimating the K_α and K_β yield of the Ta foil is done in the same way. However, instead of using the radiation yield, the X-ray production Cross section of the Ta K_α and K_β lines tabulated in the NIST Standard Reference Database 164 [106] is used for the calculation. The calculations show a total generated photon count of 6.04×10^{11} for the Bremsstrahlung and 1.09×10^{11} in the case of characteristic X-rays. Therefore, 84.7% of all produced X-rays during the TNSA process are contained in the Bremsstrahlung spectrum. However, when looking at the irradiation of Kr, which will be described in more detail in the next chapter, it can be observed that the contribution of Bremsstrahlung to the total XRF yield of the sample is lower than one would expect from the photon count. Multiplying the photon count at each energy with the corresponding cross section (literature only proved values between 14.36 and 200 keV [107]) shows that the XRF yield produced by Bremsstrahlung per atom ($\sim 4.69\times10^{-13}\,\frac{\mathrm{MeV\cdot cm^2}}{\mathrm{atom}}$) is two magnitudes lower than the yield induced by the characteristic Ta X-rays ($\sim 1.34 \times 10^{-11}\,\frac{\mathrm{MeV\cdot cm^2}}{\mathrm{atom}}$).

4 Results and Discussion

After understanding the theory behind the yield calculations in multilayer samples, as well as the experimental setup and processing of the measurement data, the data gathered by the experiments can be fully analyzed and interpreted. The presentation of the results is divided into three parts. First, the experimental results of testing and calibrating the energy selector discussed in chapter 3 are presented. The second section aims to try to validate the calculations and performance of the presented *MATLAB* code for the analysis of the X-ray spectra. The combination of the results of sections 4.1 and 4.2 lays the groundwork for future experiments utilizing a layer-by-layer method, from the basis of a continuous proton spectrum. The energy selector is crucial for targeting different layers inside the sample, and the presented *MATLAB* code will take over the analysis of the gathered data. Hence, both components need to be calibrated, verified, and tested for a successful implementation of the developed multilayer methodology. Lastly, the results from the application of X-ray and Particle Induced X-ray Fluorescence (XPIF) on gas mixtures are presented. To this end, the dilution of Kr aerosols in air was measured at various dilution levels.

4.1 Implementation of the energy selector

Before commencing with the experiments, the functionality of the energy selector from Chen et al. [78] (see chapter 3) needs to be verified at the present beamline and experimental setup at ALLS. Afterwards, the selector can be calibrated to determine the necessary slit positions for various central energies and bandwidths. Since the Thomson Parabola (TP) can not be used during the experiment, it is crucial to gather this information beforehand to allow for accurate knowledge of the penetration depth during the layer-by-layer procedure.

4.1.1 Verification and calibration

Figure 4.1 shows the central energy of the proton spectrum as a function of the slit position. The first slit, through which the protons enter the selector, was kept fully open, while the second slit, made from tantalum (Ta), was maintained at a constant opening of 1 mm. With this configuration, the slit was moved step by step over the entire range until the maximum proton energy was reached. The red line is solely used for the visualization of the nonlinear relationship between the two parameters. The main

observation is that for achieving increasing central energies the slit needs to be moved by an increased distance. This is because, as discussed in chapter 3, the electrons are deviated more strongly for lower kinetic energies.

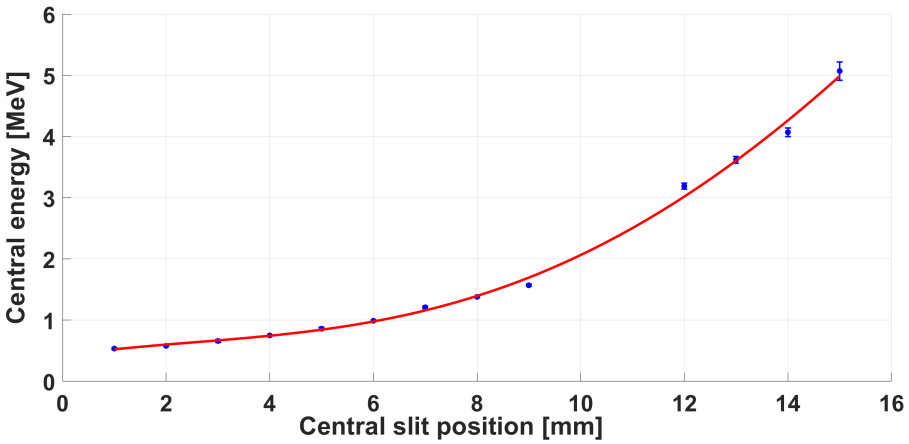

Figure 4.1 Central proton energy of the protons that the selector let through as a function of the location of the secondary tantalum slit relative to the incident beam axis (blue). The red line is a visualization for the changing relation between the central energy and the central slit position. The opening of the tantalum slit was kept at 1 mm.

Figure 4.2 depicts the relation of the central energy to the bandwidth of the let-through proton spectrum as seen in Figure 4.3. The experimental procedure was the same as employed for the acquisition of the data in Figure 4.1. Following the visualization of the dependency between central energy and bandwidth (red), it can be seen that the bandwidth increases with increasing central energy. The non-linear behaviour is the result of the Lorentz force, which scales non-linearly with the particle energy, resulting in a bunching together at higher proton energies.

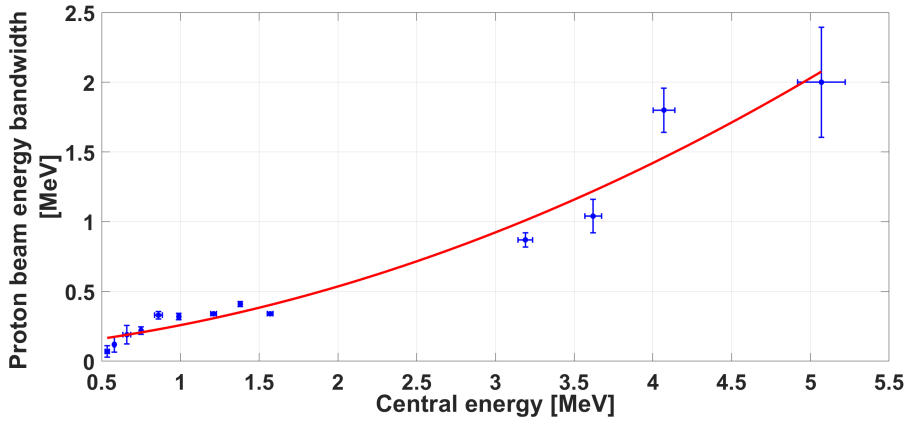

Figure 4.2 Energy bandwidth of the proton spectrum after passing through the selector as a function of the central energy (blue). The opening of the tantalum slit was kept at 1 mm.

Figure 4.3 shows the proton spectra, produced during the experiments, which were used to generate Figure 4.1 and Figure 4.2. The spectra exhibit both characteristics found in the preceding figures as well as the SIMON simulations (Figure 3.4) by Chen et al. [78]: The increased distance necessary for higher central energies, as well as the larger bandwidth for an increasing central energy.

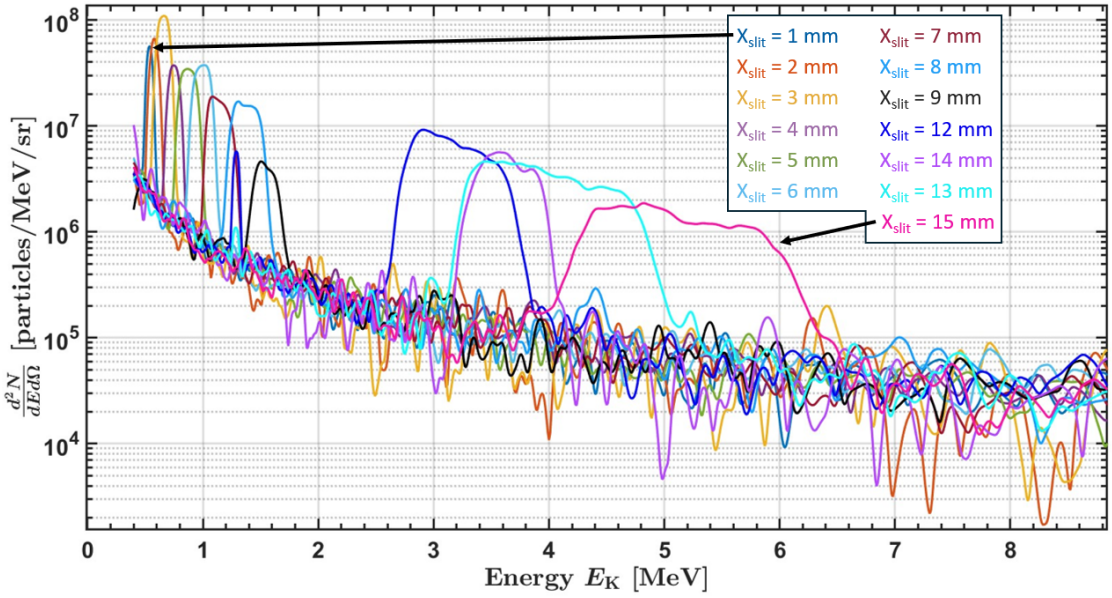

Figure 4.3 Proton spectrum after the deployment of the energy selector. The different curves correspond to different positions of the tantalum (Ta) slit and spectra were averaged over 10 shots each. The plateaus correspond to an increasing slit position from left to right, as indicated by the two arrows.

The results shown in Figure 4.1, Figure 4.2, and Figure 4.3 demonstrate that the observations made by Chen et al. [78] can be reproduced using the beamline at ALLS, highlighting the versatility of the proposed method. The verification is an important step since the two experimental setups differ in their key parameters, such as target material, laser pulse length, and focal spot diameter. Confirming that the energy selector can be effectively utilized to control the proton energy enables a layer-by-layer analysis of solid samples.

The selection of the central energies works well, enabling us to fine-tune the proton beam. However, instead of the ∼10% bandwidth observed in the work of Chen et al. [78], the setup at ALLS exhibits a more strongly increasing trend for higher central energies with an increased value across the board as shown in Table 4.1. At 0.99 MeV, the ALLS measurements show a bandwidth of 34.7% while at 5.07 MeV it increased to 47.2%. This decreases the ability to accurately probe thin layers deep into the material. In cases where multiple thin layers coat the bulk material, this should, however, not limit the capabilities of multilayer Particle-Induced X-ray Emission (PIXE) too much, since the

bandwidth is minimized at lower central energies, which mainly deposit their energy in the first few material layers. The reason behind the discrepancy between the bandwidth percentages is the increased distance between the selector and the source in the different setups used for the experiments. A greater source-selector distance allows the proton beam to diverge more before entering the selector, therefore distorting the diffraction of the protons, resulting in a broader bandwidth.

Table 4.1 Measurement data of the proton bandwidth for different central energies, shown in Figure 4.2.

Central energy	Bandwidth
0.54 MeV	20.7%
0.99 MeV	34.7%
1.57 MeV	22.3%
2.01 MeV	28.9%
3.19 MeV	28.9%
4.07 MeV	48.1%
5.07 MeV	47.2%

The overall average transmission ($T = \frac{\text{Proton yield with the selector}}{\text{Proton yield without the selector}}$) of the energy selector within the corresponding bandwidth region, overall measured central energies is $20 \pm 9\%$. As expected, a majority of protons are lost for the benefit of selecting the energies out of a continuous spectrum, resulting in a lower X-ray yield per shot. However, this limitation can be compensated for by performing an increased number of shots for the acquisition of a single characteristic X-ray spectrum.

The average proton count of the selected plateau is between one and, in the best case, two magnitudes higher than the rest of the spectrum. However, a consistent background spectrum (average magnitude $\sim 10^5$) is observed across all settings of the energy selector, ranging over the entire energy spectrum. The background was found to be the noise of the camera setup and is present even without the selector being installed. Figure 4.4 shows how the energy range (minimum to maximum of the plateau shown in Figure 4.3) depends on the position of both slit edges. The slit position gives the distance of the edge from the fully retracted position of the corresponding edge. The observed characteristic is the same as in Figure 4.2. At a higher slit position, and hence higher central energies, the spatial difference between protons of different energies decreases, increasing the energy range for an identical travel distance of the slit. Once the edge of the plate comes close to the center of the original proton beam axis, the width of the proton spectrum increases drastically. The two datasets, shown in Figure 4.4, display a slight difference due to the different starting positions of the upper and lower edge of the slit. This again confirms the results of the simulations and observations performed by Chen et al. [78].

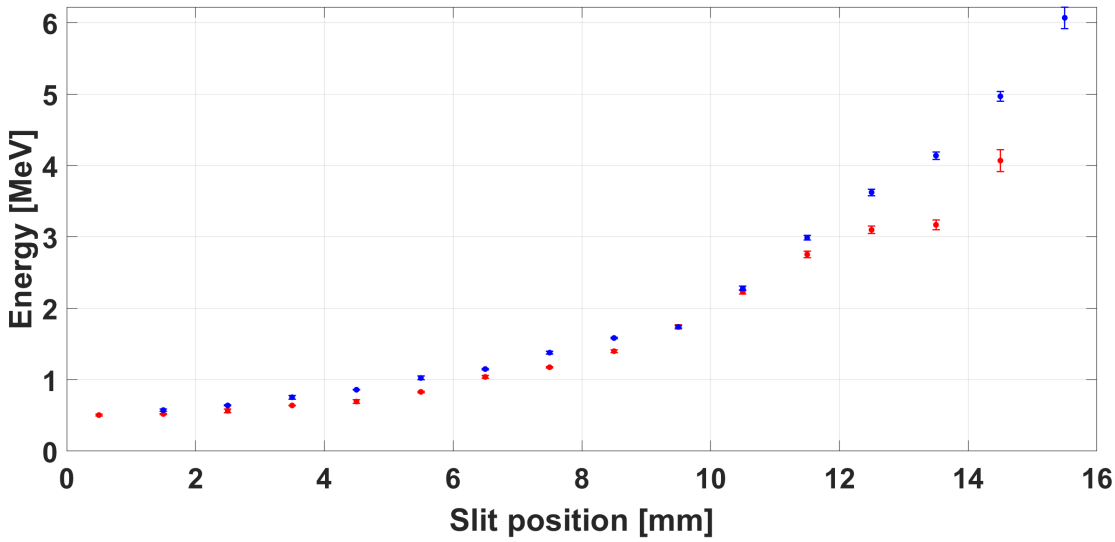

Figure 4.4 Proton energy for different positions of both individual slit edges. The edges were moved at the same time with a fixed distance of 1 mm between them.

4.1.2 Future experiments

The presented calibration measurements are particularly valuable, as the data in Figure 4.4 allows us to calculate the expected energy range ΔE for various slit openings and positions and vice versa. The calculation depends only on the specific location of each edge, as described Equation 4.1, where E_{lower} and E_{upper} are the energies of the corresponding edge positions:

$$\Delta E = E_{lower} - E_{upper}. \tag{4.1}$$

For future experiments, three different samples are proposed for future experiments, as schematically shown in Figure 4.5. The two-layer and 3 layer samples are the same as those used in the work of Puyuelo-Valdes et al. in 2021 [1], which will be discussed in a bit more detail in the next section. Using the data gathered from the measurements of section 4.1.1, one can calculate the necessary slit positions to probe each layer. The results are shown for the 4-layer sample in Table 4.2. With the proposed energy selector settings, based on the calibration measurement data, the overall procedure of the multi-layer analysis will be verified. The utilized laser interaction target will be made of 2 µm thick tantalum. While the sample will not experience any X-Ray Fluorescence (XRF), since the Target Normal Sheath Acceleration (TNSA)-produced X-rays are blocked by the selector, it is important to note that the combination of 5 µm nickel and 5 µm copper attenuate 98.28% and 98.69% of characteristic iron X-rays. Therefore, it can be assumed that no characteristic X-rays from the bulk will reach the detector even after multiple shots. Similarly, only 4.1% of characteristic X-rays from the second nickel layer will reach

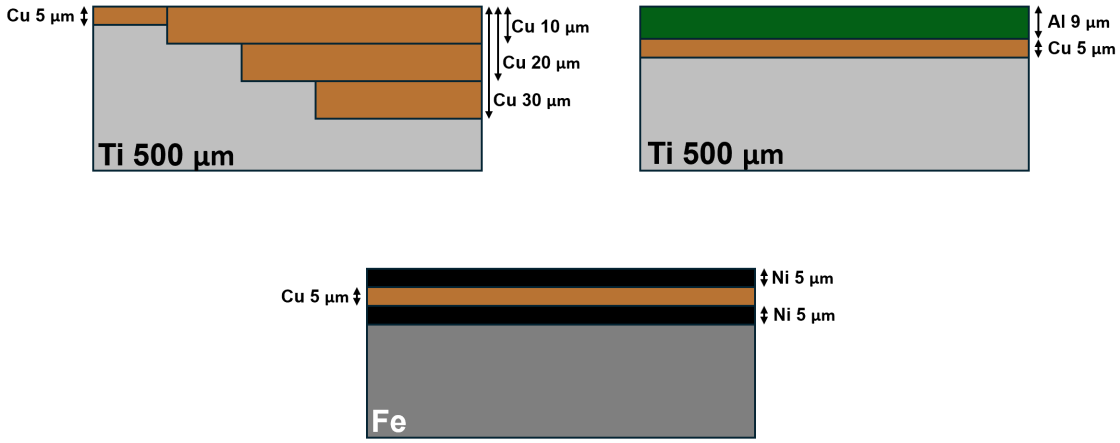

Figure 4.5 Schematic of three proposed samples for future multilayer experiments. Top left: Different thicknesses of copper (Cu) on a 500 µm thick titanium (Ti) substrate. Top right: A three-layer structure made of aluminum (Al), Cu, and a 500 µm thick Ti bulk. Bottom: 4-layer sample made of 5 µm nickel (Ni), 5 µm copper, 5 µm Ni, followed by a bulk made of iron (Fe).

Table 4.2 Proposed slit positions, based on the proton energy deposition, for a multilayer analysis of a 4 layer sample composed of 5 µm Ni, 5 µm Cu, 5 µm Ni, and a Fe bulk.

Layer	Last proton energy which deposits a Bragg peak	Slit position		
		Upper edge	Lower edge	Slit width
5 µm Ni	0.86 MeV	1 mm	3.8 mm	2.8 mm
5 µm Cu	2.05 MeV	6 mm	10 mm	4 mm
5 µm Ni	3.18 MeV	10.2 mm	11.6 mm	1.4 mm
Fe bulk	Up to cut-off energy	13.8 mm	15.5 mm	1.7 mm

the detector. Secondary fluorescence is possible between the K_α and K_β X-rays of copper and the top layer made of nickel. This result again highlights how crucial the ordering of layers and elements is for a successful XPIF analysis, as a suboptimal arrangement can severely limit the capabilities of the technique. These predictions will require experimental verification in forthcoming experiments to provide better insight into the limitations of this multilayer procedure.

4.2 Verification of the multilayer yield calculations

At the time of writing, experimental data of the tested multilayer samples with the energy selector were not yet available. Although these experiments were initially planned, scheduling constraints at the laser facility prevented their completion. There are, however, scheduled experiments on multilayer samples to be conducted in the near future, using the samples shown in Figure 4.5.

Instead, it is attempted to evaluate the code's performance, including the calculations for multilayer samples based on an old measurement performed in the same laboratory in 2021. In the work of Puyuelo-Valdes et al. [1], a bulk sample composed of pure titanium was covered with copper layers of varying thickness (5, 10, and 20 µm, schematically shown in Figure 4.5), and was irradiated using the XPIF method. The target material used for the laser acceleration was copper, which is currently the only element fully implemented in the code. For targets with higher atomic numbers like gold (Au) or tantalum, Bremsstrahlung and characteristic $L_{\alpha,\beta}$ have to be included in the calculations. While the first calculations for Bremsstrahlung are already completed, they need to be verified along with the $L_{\alpha,\beta}$ intensities.

While the *MATLAB* code presented in the previous chapter is ready for deployment, verifying its calculations remains challenging due to the lack of data. For the code's verification, the amount of titanium under the different copper layers, irradiated by a continuous proton spectrum, is estimated. Ideally, the calculations will yield a ∼100% pure titanium bulk since the yield from the detected copper peaks will be accounted for by the top layer calculations. The measurements performed by Puyuelo-Valdes et al. [1] are shown in Figure 4.6. It can be seen that with an increasing thickness of the copper layer, the size of the titanium K_α line is decreasing. This behaviour is aligned with the expectations, since a thicker copper layer results in the absorption/blockage of more X-rays and protons.

Table 4.3 Transmission of characteristic K_α X-rays of copper and titanium through copper layers of various thicknesses, along with the projected range of electrons for the same thickness and the proton count which does not escape the top layer (total proton count before energy deposition: 6.6×10^{10}).

	5 µm thickness	10 µm thickness	20 µm thickness
X-ray transmission Cu_{K_α}:	77.6%	60.8%	36.3%
X-ray transmission Ti_{K_α}:	29.1%	9.1%	0.7%
Proton cutoff energy	0.783 MeV	1.302 MeV	2.089 MeV
Proton number below cutoff energy	2.1×10^{10} (≙ 31.8%)	4.0×10^{10} (≙ 60.6%)	5.4×10^{10} (≙ 81.1%)

Figure 4.7 shows the decreasing proton count due to energy deposition in the top layer, and Table 4.3 shows how much the different types of X-rays get attenuated when passing through the sample. This is especially important when considering the characteristic

radiation ($K_{\alpha,\beta}$) of titanium, which is attenuated much more because those photons are less energetic than the K_α X-rays of copper. At a thickness of 20 µm almost no X-rays are able to pass through the copper layer anymore. The cutoff energy (also called projected range) in Table 4.3 is the energy at which a proton is not able to pass through the top layer anymore. Consequently, all of the energy is deposited and contributes to a yield generation via PIXE in the copper layer. In the *MATLAB* routine, the cutoff energy is used to differentiate between the usage of the thin or thick PIXE formalism as described in chapter 2.

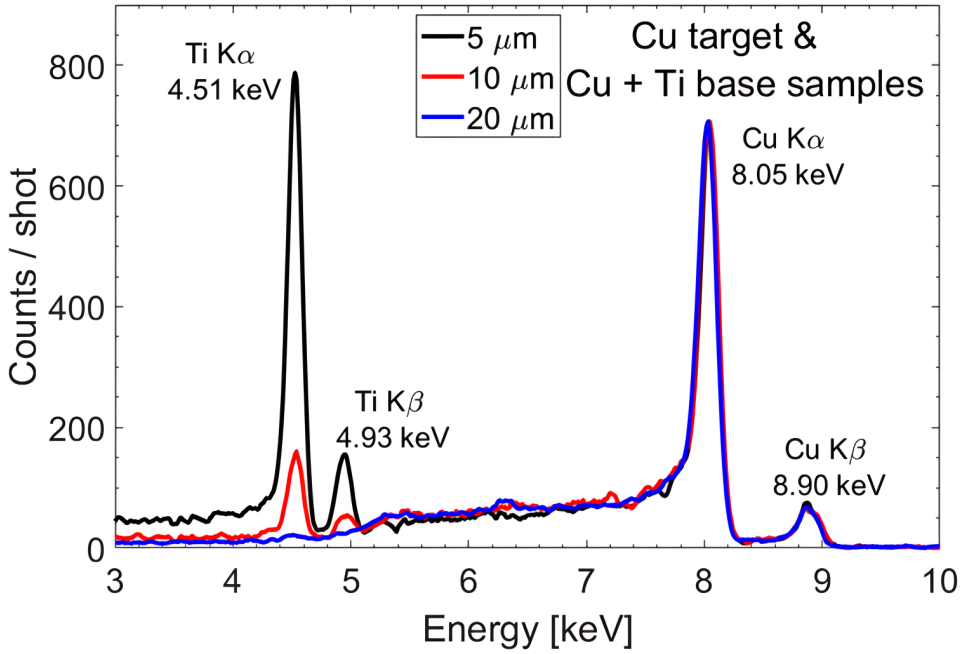

Figure 4.6 Ti-Cu measurement performed by Puyuelo-Valdes et al. in 2021 [1] for a 5, 10, and 20 µm copper layer on a titanium substrate (using the copper interaction target with the proton spectrum shown in Figure 4.9). For the calculations, the data was extracted using the *GRABIT* Add-On provided for *MATLAB*.

The calculations align with the observation in Figure 4.6, where no titanium K_α line is visible for the measurement with a 20 µm thick layer. Even though some of the protons are able to reach the titanium bulk, the excited characteristic X-rays of titanium are not energetic enough to penetrate the top layer on their way to the detector. This limitation is a crucial factor when handling multilayer samples, since it limits the detection depth of the XPIF method, even when provided with incoming TNSA X-rays and protons of sufficiently high energies. If the combination of elemental composition and thickness of the top layer is disadvantageous, the X-rays will not be detected. An observation from Figure 4.6, not aligning with expectations, is the constant height and area of the Cu K_α line. Instead, an increase in height with increasing thickness of the layer is expected, because more X-rays and protons will deposit their energy in the top layer.

This finding is not further discussed in the work of Puyuelo-Valdes et al. [1] and was originally interpreted as elastic diffraction of the incoming TNSA generated copper X-rays. The assumption of elastic diffraction originally led to the implementation of the diffraction calculations presented in chapter 2 into the *MATLAB* code. The results of the implementation are presented along with the impact of the multilayer calculations in the following paragraphs.

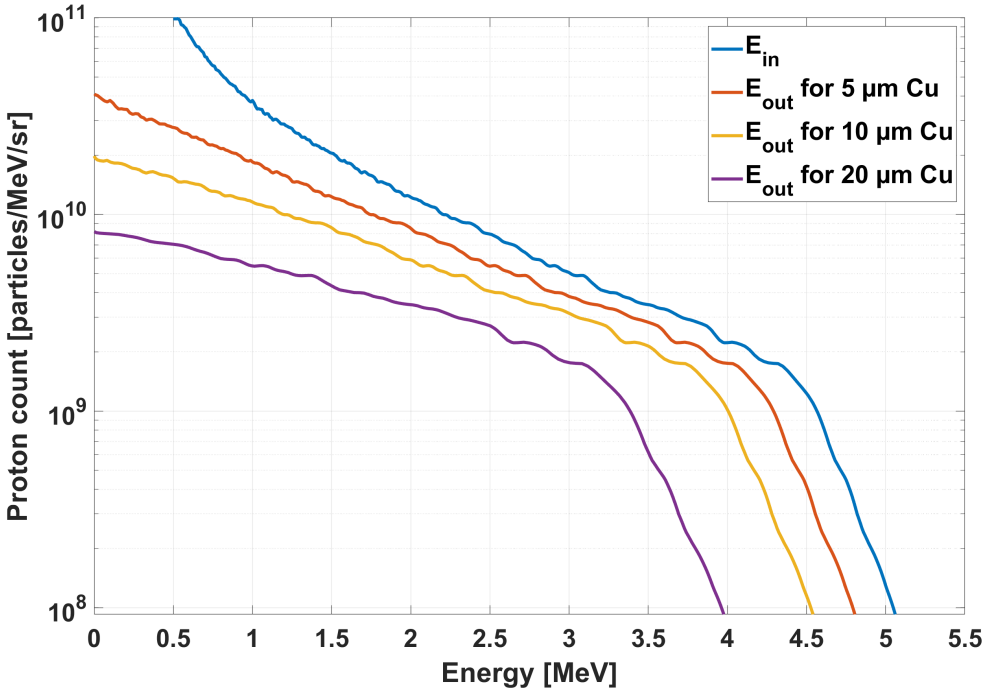

Figure 4.7 Proton spectrum after different thicknesses of copper (5, 10, and 20 µm). The calculations are performed using the equations presented in chapter 2

The original sample is 500 µm thick and has an area of 2×2 cm^2. In the following, the results of three different versions of the *MATLAB* code, described in the following paragraph, for both the 5 µm and 10 µm measurements are compared. The measurement presenting a 20 µm thick copper layer has no identifiable Ti K_α lines and was therefore excluded from the analysis:
The first code version, named "initial", represents the initial code structure before this work and does not contain any additional yield calculations for samples composed of multiple layers. The second version ("initial + top layer") implemented only the calculations for the yield produced in different layers as well as the attenuation of X-rays and protons, as described in chapter 3,. The last and "current" version of the code additionally includes the consideration of elastic diffraction by the sample back into the detector.

In the performed simulations, the comparison of the theoretical yield to the experimental yield is always a perfect fit. No post-processing was applied to the extracted data since

this was already applied to the data presented by Puyuelo-Valdes et al. [1]. The sum of the mass concentrations was limited to a range of 0.8 to 1, and the area of the peaks was calculated using a differential method. The results, presented in Table 4.4, show an

Table 4.4 Result for the mass concentrations (equivalent to percentage of that element in the sample) of the spectrum shown in Figure 4.6, as calculated by different versions of the code. The restriction $0.8 \leq \sum_i w_i \leq 1$ was applied to the simulation.

Code version		5 µm Cu layer	10 µm Cu layer
initial	w_{Cu}:	0.830	0.864
	w_{Ti}:	0.052	0.012
initial + top layer	w_{Cu}:	0.775	0.812
	w_{Ti}:	0.116	0.075
current	w_{Cu}:	0.63	0.684
	w_{Ti}:	0.264	0.214

increase in the estimated amount of titanium inside the sample when implementing more calculations in the multilayer routine. While the estimation of the "initial" code assumes only a few percent of titanium, the "current" version calculates amounts >20%. However, since a titanium bulk is investigated, these values are far from the aimed-for results. Due to the unavailability of the raw data from the work of Puyuelo-Valdes et al. [1], and the exact experimental conditions, only assumptions on the shortcomings of the calculations and the potential reasons for the low estimation of titanium in the sample can be made. The incoming copper X-rays, produced by the TNSA, do not have sufficient energy to excite characteristic X-rays in the presented copper layer. Consequently, there can be no XRF contribution resulting from this layer, and the entire copper yield must be produced by PIXE. Following this fact, one would expect that with an increasing layer thickness, the $K_{\alpha,\beta}$ counts of copper to increase, and at the same time the total $K_{\alpha,\beta}$ counts of titanium to decrease. However, while the titanium peaks follow the expected behaviour due to the increased attenuation of X-rays and protons, the copper peak does not follow the opposite trend. In the presented data (Figure 4.6), a copper peak with a constant height and area is observed for layer thicknesses up to 20 µm. This observation suggests that there is another physical interaction taking place inside the sample. This led to the assumption of elastic diffraction being the cause, which was later implemented into the yield calculations. While the inclusion of diffraction improved the estimation of the titanium amount by a large margin ($\sim$ 15%), it is not enough to explain the observed results in Figure 4.6. Otherwise, the calculations would estimate a titanium concentration close to 100% inside the sample. As mentioned in the previous chapter, the same samples will be irradiated again in future experiments to confirm the findings, find the cause of the presented phenomenon, and fine-tune the code.

Using the equations introduced in chapter 2, the contribution of the elastic diffraction

by the 5 µm and 10 µm copper layer lies at 67.3% and 71.2%, respectively. The rest of the measured Cu X-rays are assumed to be generated by PIXE since XRF does not occur inside the copper layer. In the case of the 5 µm thick copper layer, the calculated PIXE yield amounts to 6.9% of the total yield (XRF + PIXE), equalling only 2.2% of the total area (yield + diffraction) under the Cu K_α peak. As previously stated, there is no contribution from XRF since the TNSA-generated X-rays cannot excite characteristic X-rays in copper. In the case of the 10 µm measurement, the values increase to 28.8% and 8.3%. This shows that the performed calculations in the top layer seem to be correct at first glance as with an increasing thickness, the yield increases as well. However, the calculations are not able to explain the size of the K_α line of copper. Therefore, the code must assume that the remaining yield comes from the bulk (Ti) of the sample (shown in Figure 4.8), as it is not provided with any other potential source of X-ray yield. This results in an overestimation of copper inside the titanium bulk.

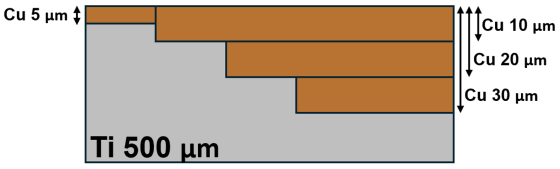

Figure 4.8 Schematic of the Cu-Ti sample used for the code validation.

Due to the observations in the measurement, it is likely that there is another factor influencing the measurement data. In the same reference, a similar experiment was conducted using gold as a laser-interaction target, shown in Figure 4.9. The sample was composed of a three-layer structure made of aluminum, copper, and a titanium bulk. Depicted left side of Figure 4.9 depicts the proton spectrum of a gold TNSA target, shown in Figure 4.5.

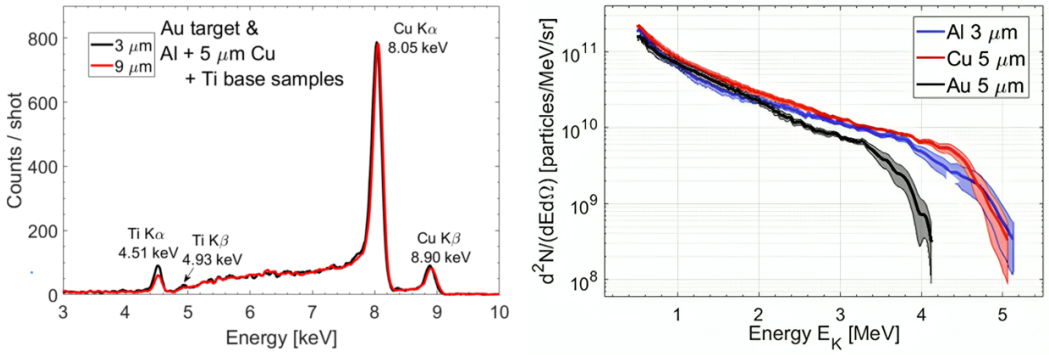

Figure 4.9 Spectra of 3 and 9 µm Al layer lying on a 5 µm Cu layer placed on a Ti substrate on the left side and the proton energy spectra as accelerated by an Al 3 µm (blue), Cu 5 µm (red) and Au 5 µm (black) thickness targets, measured by the TP spectrometer on the right. The data was extracted from [1].

The usage of a gold interaction target is not yet supported in the *MATLAB* routine, and therefore, no conclusions concerning the quantitative analysis can be drawn. Furthermore, since aluminum and gold both lie outside of the detector range, it is not possible to analyze the aluminum content or the potential elastic diffraction of gold X-rays by the top layer. Nonetheless, a constant copper peak over multiple measurements can be observed again, which in this case cannot be caused by elastic diffraction. Even considering the following factors, the observed yield can not be adequately explained:

- The slightly higher stopping power of aluminum (1.720×10^2 $\frac{\text{MeV cm}^2}{\text{g}}$ (Al) vs. 1.182×10^2 $\frac{\text{MeV cm}^2}{\text{g}}$ (Au) at 1 MeV [26]) in combination with the lower maximum energy of the proton spectrum results in PIXE being more important than XRF in the copper layer.

- Since the characteristic X-rays of gold ($K_\alpha = 68.803$ $K_\beta = 77.984$ [107]) are energetically high enough XRF is possible. However, 9 µm of aluminum transmits $\sim$ 99.95% of the incoming X-rays while the copper layer transmits 99.65%. Therefore, it can be concluded that most of the XRF happens inside the titanium bulk, and that the characteristic Ti radiation is attenuated strongly on the way to the detector, while also potentially causing secondary fluorescence in the aluminum layer. Therefore, XRF can not be the cause of the size of the copper peaks.

Thus, it is likely that the high yield observed at the K_α and K_β energies of copper is from an unaccounted-for source. Stray X-ray fluorescence from instrument components, for instance, could contribute to this signal. The last possibility is an error in the calculations of the X-ray yield. However, identifying the precise origin of the unaccounted-for counts is not possible without further experimental data for investigation.
Future work will focus on the rigorous validation of the code using a series of experiments on well-characterized samples. Although such experiments were beyond the scope of the present work due to external constraints, a comprehensive experimental plan has been established. This plan involves irradiating multilayer metallic samples, selected for their characteristic X-ray emissions within the detectable limits of the X-ray camera. The samples, shown in Figure 4.5, featuring various layer combinations and thicknesses, will be analyzed under irradiation from both a full proton spectrum and discrete, selected proton energies via the presented selector. This systematic approach will generate a robust dataset essential for verifying the code's computational accuracy and identifying any potential systematic errors.

4.3 Aerosol detection in air

The second objective of this work is to assess the feasibility of detecting aerosols in air by means of the XPIF method described in chapter 3. The chosen gas for the experiments was krypton (Kr), since it lies close to the middle of the detectable energy range of the X-ray camera and was easy to implement into the existing setup. The detection of krypton (Kr) in air was performed at three different dilution levels: 4%, 0.4%, and 0.04%. The krypton dilution was achieved using the method described in chapter 3. The measured spectra for each dilution are shown in Figure 4.10. To obtain a sufficient Signal to Noise Ratio (SNR), multiple shots were necessary: 60 shots for 4%, 100 shots for 0.4%, and 120 shots for 0.04%. Afterwards, all data was averaged to 30 shots for better comparability. The linear regression fit for the calibration of the CCD camera yields: 0.00746 ($\pm$ 0.00014) $\cdot$ x keV - 1.571 ($\pm$ 0.152) keV.

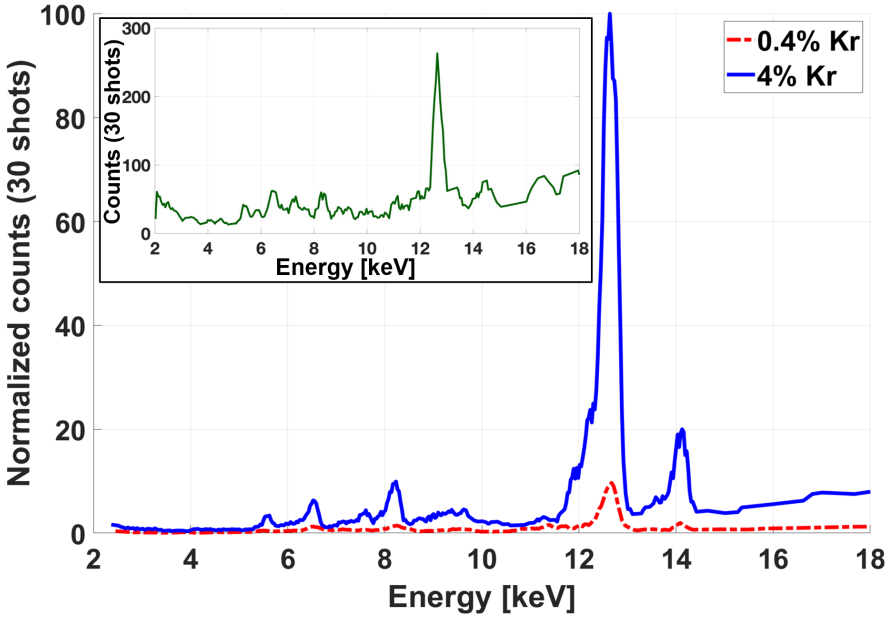

Figure 4.10 Generated X-ray spectra for the three measured proportions of krypton in air; Red: 0.4%, and Blue: 4%. The inset shows a measurement where the dilution was aimed to be 0.04%.

In all three cases, the K_α = 12.649 keV and K_β = 14.112 keV [90] peaks of krypton are identifiable without the need for post-processing. However, for the lowest dilution, it is not possible to reliably verify the krypton percentage in the gas mixture based on the measured data. While for this gas percentage, the peak satisfies the Minimal Detectable Limit (MDL) criterion introduced earlier in this work, the results of the analysis deliver unreliable information, which will be discussed in this section. It is also notable that the K_β line at 0.04% is not distinguishable from the background noise anymore. Analyzing the peaks is done by looking at the peak height and area of the K_α lines with respect to

each other.

Before investigating the peak characteristics, the recorded peak was compared to all K_α lines of elements present in the setup, confirming that the recorded signal is indeed attributed to krypton. The overlapping of different measurements additionally supports this claim. Besides the krypton peak, there are numerous other peaks (most notably at 5.62, 6.52, 7.61, 8.23, 9.63, and 11.27 keV) visible in the spectrum. The K_α lines found within the spectrum at energies lower than the nominal K_α line of krypton (12.65 keV) can be explained as follows: The generated Kr X-rays interact with the other atoms typically contained in air - mainly N_2 with an air presence of 78%, O_2 (21%), Ar (1%), and CO_2(0.04%) [82] – and lose a portion of their energy during this process. As an example, the second-largest peak at 8.23 keV can be explained by the excitation of the following X-rays by a produced K_α X-ray inside the chamber [90]: Two O_{K_α} (524.9 eV), one Ar_{K_α} (2.96 keV), and one N_{K_α} (292.4 eV) line resulting in a total energy loss of 4.40 keV. The same reasoning applies to the rest of the unidentified peaks at the aforementioned energies. It is expected that the X-rays generated by the fluorescence of krypton are the cause of the additional peaks since the X-ray cross-section of Ta-generated radiation is at least two orders of magnitude lower than that of Kr for all relevant elements [107]. This claim is further supported by the consistent intensity decrease of all peaks when the dilution level of krypton is decreased.

According to the NIST database [26], krypton exhibits a slightly lower proton stopping power than dry air across the 0–6 MeV range. This suggests that protons may induce a marginally higher X-ray yield related to air components due to increased energy deposition. However, the K_α peaks of air constituents are not detectable with the current setup, making it impossible to determine the krypton percentage based on the measurement of only one dilution level. In contrast, tantalum X-rays produced by TNSA ($K_{\alpha,\mathrm{Ta}} = 57.53\,\mathrm{keV}$) interact with krypton with cross-sections 2 to 4 orders of magnitude higher than with all air components previously listed. From this, it can be concluded that XRF indeed gives a valuable contribution to the XPIF technique. Especially in the case of krypton, XRF can help distinguish the Kr lines a bit more from background noise.

Using the TNSA proton spectrum of tantalum, as described in chapter 3, the contribution of XRF for both characteristic X-rays and Bremsstrahlung can be calculated and compared to the contribution of protons. Using the amount of radiation/protons that are hitting the sample and the respective interaction cross-sections, the yield which is generated per atom in $\frac{\mathrm{cm}^2}{\mathrm{atom}}$ is calculated. The calculations show that PIXE contributes $\sim 85\%$ to the overall signal, with the characteristic part of XRF performing the rest. The Bremsstrahlung is between two and three magnitudes lower compared to the characteristic X-rays ($K_{\alpha,\beta}$) of the laser-interaction target (Cu) and therefore considered negligible. While the XRF cross-section database only contains values up to 200 keV, the contribution is not expected to change significantly since the cross-section values decrease with

increasing incident energy of the photons [107].
To verify the quantity of krypton molecules in the gas mixture, two commonly used methods for the analysis of XRF spectra are utilized: the peak area and the peak height [108]. The results of the aerosol analysis using XPIF are recorded in Table 4.5. The area under a peak is estimated using a Gaussian fit as described in chapter 3. To quantify if a peak can be recognized as such, the MDL method described in the same section is used. Comparing the krypton peak areas in air (shown in Table 4.5), the 0.4% dilution corresponds to 8.6% of the reference peak area at a 4% dilution of krypton. The peak height is similarly reduced to 9.7%. Although it does not equal the expected 10% decrease, in correlation to the decrease in krypton dilution, both values fall within the expected error range, given the ∼18% shot-to-shot fluctuation in proton yield. In the case of the measurement of 0.04% Kr, the height and area indicated a higher krypton content than expected. This discrepancy is likely due to limitations of the measurement gauge or the method used to introduce krypton into the chamber. At low dilutions, krypton adsorption on chamber walls during evacuation and subsequent desorption upon venting can contaminate the mixture and distort the intended concentration. While negligible at 4% and 0.4%, this effect becomes significant at lower dilution levels.
Instead, the measurements at dilutions lower than 0.4% were used to refine the estimation of the SNR at low concentrations. Table 4.5 presents the corresponding SNR values and the theoretical detection limits of the setup.

Table 4.5 Summary of K_α peak characteristics for different krypton proportions in air shown in Figure 4.10. The peak height and area for the 0.04% dilution of Kr are extrapolated from the other two measurements. The values for $Y_{background}$ and Y_{MDL} are estimations based on the noise of measurements performed with a lower dilution.

Kr-proportion	Peak height [counts]	Y_{MDL} [counts · keV]	Y_{peak} [counts · keV]	$Y_{background}$ [counts · keV]
4%	3912	21	1188	49
0.4%	378	8	102	8
0.04% (estimated)	∼ 39	7	∼ 10 - 12	5

Given the presented results, it is estimated that 0.4% currently represents the lowest dilution that allows for reliable measurements with the current setup. While concentrations as low as 0.04% are most likely also detectable, the measurements are limited by the hardware and methodology of the gas mixing. At dilutions lower than ∼0.04%, a declining SNR is expected, making the analysis more challenging. However, performing more laser shots at lower dilutions could mitigate this limitation. Therefore, the setup is predicted to be able to confidently measure dilutions down to 0.01% with the current experimental setup.

5 Summary and Outlook

This chapter provides a summary of the results achieved within the scope of this thesis. Simultaneously, an outlook on future investigations is presented, discussing prospective experiments and potential modifications to the experimental setup's hardware and software. The chapter also concludes the thesis with an overview of the projected future for the X-ray and Particle Induced X-ray Fluorescence (XPIF) technique.

5.1 Layer-by-layer XPIF

In this work, the procedure of using XPIF for multilayer structured samples was introduced. After laying the theoretical groundwork by introducing the formalisms and necessary equations, the current experimental setup with its capabilities and limitations was explained. The two main components necessary for the presented method are the energy selector on the hardware side and the custom-written MATLAB procedure on the software side. It is also demonstrated that the energy selector, designed by Chen et al. [78], once installed in the ALLS facility, can allow for control of the proton energy spectrum and therefore control over the depth of proton dosage deposition. This hardware component presents the basis for a layer-by-layer scanning method. The calibration and testing of the selector show that it can generate adequate plateaus of a selected central energy. However, the bandwidth widening at higher energies poses a limitation to the accuracy of depth control deeper in the sample. This drawback arises from the distance of the selector to the source and can not be solved easily due to the limited space inside the main chamber. Based on the experimental results, the necessary slit positions for various central energies and bandwidths for future experiments are calculated for future experiments.

The original MATLAB code written by Frédéric Boivin [2], was expanded with additional calculations, lookup tables, and features enabling it to analyze samples composed of multiple layers with different elemental compositions. The modifications mainly encompass the yield calculations and attenuation by layers above the bulk material, as well as the elastic diffraction of the incoming X-rays and the implementation of lookup tables for wider coverage of elemental compositions. The first tests show that the overall routine and calculations are implemented correctly. However, due to the limited available data, validating the accuracy of the calculations remains a challenge. The measurement data of Puyuelo-Valdes et al. [1] could not be fully explained with the implemented yield calculations. Narrowing down the cause of the deviation from the expected results requires

further testing.
Therefore, a new experimental series is planned in the near future. The experiment will be composed of using XPIF on multiple metallic multilayer samples, shown in Figure 4.5. This includes the sample used by Puyuelo-Valdes et al., which was used for the validation of the MATLAB code. The new data will enable us to narrow down the source of the misidentification of the element composition. Additionally, it will provide us with more data to extensively test the *MATLAB* code. Most importantly, the new data will be complete with full knowledge of the experimental parameters and conditions. This means that finding the complications in the code can be done more efficiently and with increased precision. The samples will be irradiated with and without the energy selector installed to gather enough data for the validation of the *MATLAB* code and the functionality of the energy selector with a sample present inside the experimental chamber. This will be the first experiment performed with the selector and the irradiation of a sample at the same time. In addition to the metallic samples, there are also multiple cultural heritage mock-ups available for testing, given sufficient time during the experiment window. The samples are composed of multiple resin and varnish layers with different metallic particles embedded in them. While carbon can still not be detected with the current X-ray camera setup, the main target of these experiments is to improve the layer-by-layer scanning method and identify potential complications. The main data of interest from the experiments is the identification and location of the different particles inside the sample without the need for a quantitative analysis. Another point of interest is testing how deep inside the samples the XPIF method can probe. As discussed, this mainly depends on the composition and order of the different material layers.
Upon conclusion of the experiments, it will be possible to present and further develop a novel technique capable of analyzing multilayer samples of unknown composition and locating the elemental distribution within each layer. The accuracy and penetration depth, of course, depend on the composition of the sample. The technique can find application in various fields of research, ranging from material science [109, 110], the semiconductor industry [111], and cultural heritage [10, 112] to biomedical and environmental applications [113, 114].
There are also multiple extensions and improvements planned for the setup's hardware and software. Ongoing efforts of the ALLS team are currently directed towards [115, 116]:

- The beryllium filter of the X-ray camera is planned to be changed to increase the detection range to include elements with a lower atomic number than 14. It is also possible to add another X-ray detector with a different energetic detection range, enabling a broader coverage of the X-ray spectrum. Additionally, the addition will also increase the amount of detected X-rays, due to the isotropic nature of X-ray emission. This increases the signal-to-noise ratio as well as reduces the amount of necessary laser shots since the number of detected X-rays will nearly double.

- The energy selector is to be fitted with a better motor for a more accurate control of the slit position in the upward and downward direction.
- The team is also implementing machine learning to optimize the laser parameters before the experiment. First results show an improvement of the cut-off energy while at the same time reducing the number of shots needed to find the best parameter set. This greatly increases the efficiency of the setup.
- The multi-target holder for the thin foil laser-interaction targets is to be extended to cover more shots. This improves the efficiency since more shots can be performed during each pumping cycle.
- Before the upcoming experiments, the MATLAB code will be expanded by the calculations of secondary fluorescence as well as X-ray yield generated by the Bremsstrahlung coming from the TNSA target. Additionally, the code will be able to handle more laser-interaction targets if different materials.

Additional work is also focused on improving the shot-to-shot fluctuations of the proton and X-ray yield. Overcoming this difficulty will increase the yield significantly and make the analysis easier. The possibility of using electrons generated during TNSA for additional excitation of characteristic X-rays within the sample is also under investigation. This would mean a combination of Particle-Induced X-ray Emission and Energy Dispersive X-ray fluorescence in the same setup, further enhancing its capabilities and increasing the X-ray yield in the sample [18].

5.2 Aerosol analysis in air

This work demonstrates that the combination of laser-based PIXE and XRF enables the detection of gas concentrations down to several hundred ppm without complex sample preparation. If a reference measurement is available, relative gas concentrations can be estimated by comparing peak heights or areas using spectral fitting techniques. Although limitations in the current valve system and background X-ray noise prevent reliable quantification below 0.4%, the presence of Kr is still clearly discernible at that level. With improved laser shot-to-shot stability, signal averaging over multiple shots, and more precise gas control, the system is expected to achieve sensitivities of a few hundred ppm. This projection is based on the fact that signals corresponding to such dilutions are already detectable, but are not yet controlled with sufficient accuracy and are largely obscured by noise.
Challenges in the peak identification procedure can be addressed by narrowing down the expected element range and by integrating software-assisted analysis. This process can potentially be enhanced by AI algorithms for better peak detection [117,118]. Automated routines triggered by threshold conditions would further enable continuous monitoring of toxic aerosols or fine particulates [119, 120].

Current performance at ALLS demonstrates the feasibility of near real-time laser-XPIF for applications such as factory exhaust analysis, waste site monitoring, and urban air quality control [23, 121, 122]. The increased XRF contribution for high-Z elements also makes this method suitable for detecting radioactive species such as cesium or iodine, released during nuclear incidents. The system's resolution even allows for the distinction between isotopes such as ^{134}Cs and ^{137}Cs [123].
Although more shots are required to excite sufficient X-rays at lower Kr concentrations, the laser's 0.625 Hz repetition rate ensures this is not a limiting factor. While stable higher repetition-rate target solutions still remain a bottleneck for proton acceleration [124], some solutions already achieve 1 Hz repetition rates with cryogenic hydrogen jets having an expected scalability up to 1 kHz [125, 126]. Combined with the increasing availability of compact, cost-effective laser accelerators capable of delivering 3–5 MeV protons for PIXE [127], the scalability of laser-XPIF is looking promising [23, 120]. This fact is not only limited to environmental applications, but the for the entirety of the potential operations for XPIF.

6 Sommaire récapitulatif en français

6.1 Introduction

Au cours des dernières décennies, des efforts importants ont été consacrés à la recherche de techniques de diagnostic innovantes. Les méthodes de spectroscopie avancée, telles que Particle-Induced X-ray Emission (PIXE) et Particle-Induced Gamma-ray Emission (PIGE) [1], sont très efficaces pour la caractérisation chimique grâce à l'émission de rayons X spécifiques à chaque élément [1, 2]. Elles sont sensibles, puissantes et non destructives, mais leur dépendance à de grands accélérateurs de particules restreint considérablement leur application à plus grande échelle. Au-delà des accélérateurs, la PIXE peut aussi être réalisée à l'aide de sources laser. Cela a ouvert la voie à des applications en médecine [3, 4], en métrologie [5], pour les tests de matériaux [6, 7], le sondage de matériaux [8, 9], le patrimoine culturel [10, 11] et les études environnementales. Des installations laser comme Advanced Laser Light Source (ALLS) au Canada [12], APOLLON en France [13] et VEGA en Espagne [14] produisent de tels faisceaux de particules. Les installations conventionnelles pour le patrimoine culturel incluent AGLAE au C2RMF du Louvre [15] et le laboratoire INFN-LABEC à Florence [16, 17]. D'autres techniques similaires existent, comme la X-Ray Fluorescence (XRF) [2] et l' Energy Dispersive X-ray fluorescence (EDX) [18] basée sur les électrons. Cette thèse utilise une combinaison de PIXE et de XRF (nommée X-ray and Particle Induced X-ray Fluorescence (XPIF)) pour une analyse multi-élémentaire non destructive. Les expériences ont été menées à l'installation ALLS, en utilisant le processus Target Normal Sheath Acceleration (TNSA) pour générer des faisceaux de protons stables jusqu'à $\sim$ 6 MeV avec des rendements de 10^{10} - 10^{12} [2]. Un avantage clé de cette configuration est l'utilisation des rayons X supplémentaires produits durant la Target Normal Sheath Acceleration (TNSA), ce qui augmente le rendement en rayons X et réduit le temps de mesure nécessaire [1]. La PIXE est un domaine d'intérêt croissant, avec des lignes de faisceau dédiées dans de grandes installations comme ELI (ELIMAIA) et le C2RMF (AGLAÉ) [19, 20]. Malgré un intérêt considérable et les données disponibles, un outil d'analyse robuste pour les échantillons multicouches pour des énergies de protons entre 1 et 7 MeV fait défaut. Ce travail vise à établir un cadre fondamental pour combler cette lacune.

Objectifs

Le principal avantage d'utiliser des particules chargées comme les protons par rapport aux électrons (EDX) est leur profil unique de dépôt d'énergie. Elles déposent la majorité de leur énergie dans une région étroite à la fin de leur trajectoire, connue sous le nom de pic de Bragg. Pour des protons de 70 MeV, le dépôt d'énergie au pic est 6 fois plus élevé qu'au point d'entrée, un rapport qui augmente pour des énergies plus faibles [21]. Ce dépôt dépendant de la profondeur, combiné à une pénétration pouvant atteindre le cm [21, 22], permet de sonder des emplacements spécifiques au sein d'un échantillon. Même avec un large spectre de protons, les couches sous-jacentes peuvent être analysées. Bien qu'un large spectre augmente le rendement en rayons X, il complique l'analyse quantitative car les interactions matérielles dépendent de l'énergie. Ce défi mène aux deux principaux objectifs de cette thèse :

1. L'objectif principal est l'analyse élémentaire couche par couche d'échantillons multicouches de composition inconnue. Un code *MATLAB* personnalisé a été développé pour interpréter les données brutes, analyser le spectre et calculer les quantités élémentaires, en tenant compte des interactions dans les couches supérieures. Un "sélecteur d'énergie" sera mis en œuvre et calibré pour le balayage couche par couche. Cette méthode s'avérera particulièrement utile pour le patrimoine culturel et la science des matériaux, avec des applications potentielles dans les domaines des semi-conducteurs et de la biologie.

2. Le deuxième objectif est de démontrer la faisabilité de la technique XPIF sur les aérosols. Cela a été testé en irradiant différentes dilutions de krypton (Kr) dans l'air. La haute précision de la PIXE (environ 100 ppm) permet la détection d'éléments tracés nocifs [23]. Comparée à l'EDX/SEM pour les aérosols filtrés [24], qui implique une préparation d'échantillon complexe et dispose de données limitées sur les seuils de détection, la XPIF peut être effectuée directement dans l'air. De plus, pour les gaz courants (carbon (C), oxygen (O), hydrogen (H), nitrogen (N), argon (Ar), calcium (Ca)) et le Kr, les sections efficaces d'interaction des protons dans la gamme d'énergie de la PIXE sont de 10 à 1000 fois plus grandes que celles des électrons aux énergies typiques de l'EDX/SEM [25–28]. Cela fait de la PIXE une alternative viable.

Plan de la thèse

La thèse est structurée comme suit : D'abord, elle présente les principes physiques et les équations nécessaires aux mesures et aux calculs. Ensuite, elle détaille le montage expérimental et le code *MATLAB* utilisé pour l'analyse des données. Enfin, elle discute les résultats et les améliorations du code, suivie d'un aperçu des travaux futurs.

6.2 Théorie

Ce chapitre présente la théorie et les principes physiques nécessaires à la compréhension des expériences, du code et des données de mesure présentés plus loin dans cette thèse. Il décrit d'abord la génération du faisceau de protons et des rayons X utilisés pour sonder le matériau, puis aborde les diverses interactions de ces particules et photons au sein de la matière solide.

Particle-Induced X-ray Emission et X-Ray Fluorescence

L'approche fondamentale de la X-Ray Fluorescence (XRF) et de la Particle-Induced X-ray Emission (PIXE) est très similaire à celle de l'EDX. Cependant, le principe de la XRF et de la PIXE repose sur l'excitation des électrons d'un atome par irradiation de photons (rayons X) et d'ions (protons). L'analyse des spectres de rayons X produits permet alors de déterminer la composition chimique de l'échantillon irradié. Les deux techniques sont non destructives, capables d'identifier plusieurs éléments à la fois, rapides et offrent un seuil de détection bas (PIXE) ainsi qu'une haute sensibilité [29, 30]. Cela en fait de bons candidats pour l'analyse d'éléments tracés. La mesure peut être réalisée sur des échantillons solides, liquides et, comme nous le verrons plus tard, gazeux. Outre le mécanisme d'excitation, elles diffèrent par le volume analytique, la distribution du bruit de fond et les limites de détection [9]. La XRF peut offrir une zone d'analyse relativement grande (jusqu'à quelques mm), tandis que celle de la PIXE est plus petite (jusqu'à quelques dizaines de µm). Le bruit de fond de la PIXE diminue pour les éléments à numéro atomique élevé, alors qu'il augmente pour la XRF, la rendant plus adaptée aux éléments légers. Les deux techniques se complètent donc, le contrôle de la profondeur d'analyse étant uniquement piloté par le mécanisme PIXE [1]. Les mesures effectuées dans cette thèse produisent des spectres de rayons X, qui sont ensuite analysés par le logiciel présenté ultérieurement. Pour une bonne interprétation des données, les principes physiques de la génération de rayons X sont brièvement expliqués. Un spectre de rayons X typique est composé d'une partie continue (Bremsstrahlung) et d'un spectre de raies, dit "caractéristique" [9, 31]. Ce dernier est, comme son nom l'indique, propre à chaque élément. Ce processus est bien décrit par le modèle atomique de Bohr, montré à la Figure 6.1, qui est suffisant pour la compréhension de cette thèse [32]. L'émission de rayons X caractéristiques se produit lorsqu'un électron est retiré d'un atome par une source d'excitation externe. Cette éjection crée une lacune, laissant l'atome dans un état ionisé. Un électron d'une couche supérieure transite alors vers cet état inférieur pour combler la lacune. La différence d'énergie se traduit par l'émission d'un photon. Comme ces écarts d'énergie sont uniques à chaque élément, ce phénomène permet de caractériser les éléments constitutifs d'un échantillon à partir d'un spectre mesuré. Bien que toutes les transitions soient possibles, la plus probable est celle de la couche L vers la couche K. Les raies résultantes dans le spectre sont appelées K_α et K_β. Ces deux raies sont de loin

Figure removed due to copyrights issues

FIGURE 6.1 Génération de rayons X caractéristiques de la couche K. Un proton ou un photon incident éjecte un électron de la couche K. La lacune est comblée par un électron d'une couche supérieure, et la différence d'énergie est émise sous forme de photon. La raie résultante dans le spectre est nommée K_α ou K_β selon la transition [33].

les plus dominantes en intensité et en probabilité, et sont donc principalement utilisées pour l'analyse des spectres de rayons X. L'analyse dans ce travail se base également uniquement sur les raies K_α et K_β. Outre l'émission d'un photon, il est aussi possible que l'énergie soit utilisée pour libérer un second électron de l'atome. C'est ce qu'on appelle l'effet Auger. Il est cependant surtout présent dans les éléments à faible numéro atomique ($Z < 12$) [32] et ne sera pas détaillé davantage, car ces éléments ne sont pas dans la plage de détection du détecteur de rayons X, discutée au chapitre section 6.3.

Accélération normale par gaine à la surface de la cible

Cette section explique la génération de faisceaux d'ions par accélération laser. L'utilisation de lasers pour générer des ions n'est pas une idée nouvelle. Les premières expériences Target Normal Sheath Acceleration (TNSA) sur des cibles métalliques, stimulées par l'avènement des lasers femtosecondes, ont été publiées en 2000 [34,35]. Depuis, le domaine a connu des avancées significatives, ouvrant la voie à de nombreuses applications. Les faisceaux d'ions produits par laser sont uniques en raison de leur grand nombre de particules et de leurs rafales énergétiques et intenses. Le nom TNSA vient du fait que les ions se dilatent normalement depuis la surface arrière de la cible, en forme de cône. Cette section se concentrera sur le principe de fonctionnement du mécanisme TNSA, sans entrer dans des détails théoriques ou mathématiques excessifs, car ce n'est pas le sujet principal de cette thèse. Pour produire un faisceau d'ions à partir de l'interaction entre un laser et une feuille de métal solide, plusieurs conditions sont requises [36–38] :

- Une intensité d'impulsion laser supérieure à $10^{18} \frac{W}{cm^2}$ pour déclencher la force pon-

déromotrice.

- Une impulsion courte (< ps), plus brève que le temps d'expansion de la cible, pour maintenir la surface arrière intacte.
- Un contraste laser élevé (rapport entre l'impulsion principale et les pré-impulsions, ou ASE) [39].
- Une cible très mince (de l'ordre du nanomètre ou du micromètre).

Les systèmes modernes d'accélération par laser utilisent l'ionisation par effet tunnel. Le processus TNSA commence par la force pondéromotrice du laser qui génère des électrons chauds, ce qui modifie la distribution de charge dans la cible. Les champs de séparation de charge qui en résultent accélèrent alors les ions. Les bases de cette technique sont illustrées à la Figure 6.2 et sont résumées ici en se basant sur les travaux de M. Roth, M. Schollmeier [36] et J. Schreiber [39].

Figure removed due to copyrights issues

FIGURE 6.2 Schéma du processus TNSA, tiré de [36]. L'impulsion laser frappe la cible d'épaisseur micrométrique. Une pré-impulsion crée un pré-plasma avec lequel l'impulsion principale interagit. Des électrons de l'ordre du MeV sont ensuite propulsés à travers la cible, formant une gaine d'électrons dense à la surface arrière. Les forts champs de séparation de charge ($\sim \frac{TV}{m}$) ionisent les atomes à l'arrière de la feuille, qui sont ensuite accélérés par ce champ.

Pour une accélération efficace des protons, une surface de cible non perturbée est essentielle, ce qui signifie qu'un rapport de contraste temporel élevé ($\geq 10^6$) est nécessaire pour supprimer les pré-impulsions. Au-dessus du seuil d'intensité relativiste ($I_L > 10^{18} \frac{\mathrm{W}}{\mathrm{cm}^2}$ pour un laser de 1 µm), la force pondéromotrice pousse les électrons, ionisés par effet tunnel, vers l'avant. L'efficacité de conversion peut atteindre 90% à des intensités très élevées, générant ainsi de nombreux électrons énergétiques nécessaires. Le nombre d'électrons

chauds est estimé par $N = \frac{\eta E_L}{k_b T_{hot}}$ [36], où E_L est l'énergie du laser et T_{hot} l'énergie cinétique moyenne de l'électron. Les électrons accélérés sont chauffés par des mécanismes tels que le chauffage $\vec{J} \times \vec{B}$ et le chauffage par le vide dans la gamme d'intensité de 10^{18} - 10^{20} $\frac{\mathrm{W}}{\mathrm{cm}^2}$. Ces électrons chauds traversent la cible à des vitesses relativistes, de sorte que leur libre parcours moyen dépasse l'épaisseur de la cible, bien que seule une fraction s'en échappe. Pour contrer le champ magnétique auto-généré par les électrons en déplacement, des courants de retour se forment, comme le montre la Figure 6.3. Sans eux, le champ magnétique limiterait gravement le déplacement des électrons. Les collisions et la diffusion provoquent également une divergence de la distribution des électrons, ce qui réduit encore l'effet du champ magnétique [36, 39]. À la surface arrière, la séparation des charges piège la plupart des électrons, formant une "gaine". Cette gaine crée un fort champ électrostatique sur une distance de l'ordre de la longueur de Debye λ_D [41].

Figure removed due to copyrights issues

FIGURE 6.3 Schéma du transport des électrons rapides générés par laser dans la cible. Le courant d'électrons j_{fast} (vert) crée une filamentation (rouge clair) et des champs magnétiques (bleu). À l'arrière, la gaine d'électrons provoque une recirculation $j_{ret.}$ et confine les électrons. Figure tirée de [36].

La densité d'électrons à l'arrière est proportionnelle à l'intensité du laser et inversement proportionnelle à l'épaisseur de la cible. Le champ qui en résulte, d'une intensité de plusieurs $\frac{TV}{m}$, confine les électrons de plus faible énergie, les faisant recirculer. Cette recirculation est particulièrement importante pour les feuilles de moins de 10 nm, car elle augmente l'énergie maximale des protons [36]. Le champ électrique longitudinal ionise les impuretés à la surface arrière de la cible, et ces ions sont accélérés normalement à la surface jusqu'à des énergies pouvant atteindre des centaines de MeV. L'ionisation par le champ est le processus dominant. Ces conditions mènent à un faisceau d'ions de haute qualité, de faible divergence et orienté vers l'avant. Une impulsion laser courte est essentielle pour un champ accélérateur puissant, et un contraste laser élevé (voir Figure 6.2)

est nécessaire pour éviter la formation prématurée de plasma. Ainsi, le mécanisme TNSA repose sur un nuage dense d'électrons chauds pour le transfert d'énergie, l'accélération étant expliquée par un modèle d'expansion de plasma [38,42]. En conclusion, ce processus génère également des rayons X [2]. Les énergies des photons correspondent généralement aux raies K_α et K_β du matériau de la cible. Pour les matériaux à numéro atomique plus élevé, le Bremsstrahlung élargit le spectre [27]. Les expériences décrites dans cette thèse ne prendront en compte que les protons et les rayons X caractéristiques dans les calculs de rendement [36].

Interaction des rayons X et des ions avec la matière

Cette section examine l'interaction des protons et des rayons X avec un échantillon, en se concentrant sur la perte d'énergie et la génération de rayons X caractéristiques. Les équations clés utilisées pour l'analyse des spectres de rayons X avec un code *MATLAB* personnalisé seront détaillées.

Règle d'additivité de Bragg

Avant d'aborder les interactions, nous devons introduire la règle d'additivité de Bragg (Bragg et Kleeman 1905 [43]). Cette règle permet de calculer des propriétés comme le pouvoir d'arrêt pour les matériaux composés, souvent absentes des bases de données. Elle approxime la propriété d'un composé par la somme pondérée de ses composants élémentaires [9, 44, 45] :

$$\frac{S}{\rho} = \sum_i w_i \left(\frac{S}{\rho}\right)_i, \tag{6.1}$$

où $\frac{S}{\rho}$ est le pouvoir d'arrêt massique et w_i est la fraction massique de chaque élément. La règle, montrée à l'Equation 6.1, est une approximation qui ignore les liaisons chimiques et les états physiques [9]. Néanmoins, elle est généralement considérée comme précise [44].

Mécanismes d'interaction des rayons X avec la matière

Cette partie traite de l'interaction des rayons X avec des échantillons solides, y compris la perte d'énergie et le calcul du rendement de la X-Ray Fluorescence (XRF) dans les échantillons minces et épais.

Loi de Beer-Lambert

La loi de Beer-Lambert décrit la diminution exponentielle de l'intensité I des photons traversant un matériau homogène [46, 47] :

$$I = I_0 \cdot e^{-\mu \cdot d \cdot \rho}, \tag{6.2}$$

où I_0 est l'intensité initiale, μ le coefficient d'atténuation massique, et d et ρ l'épaisseur et la densité de l'échantillon. La règle de Bragg s'applique également ici pour les composés. Le coefficient d'atténuation massique μ dépend de l'énergie. Comme on le voit pour le copper à la Figure 6.4, il y a un front d'absorption K abrupt. À cette énergie, les photons incidents peuvent éjecter les électrons de la couche K, provoquant une forte augmentation de l'absorption [46].

Figure removed due to copyrights issues

FIGURE 6.4 Le coefficient d'atténuation massique $\frac{\mu}{\rho}$ (ligne continue) et le coefficient d'absorption d'énergie massique $\frac{\mu_{en}}{\rho}$ (ligne pointillée) en fonction de l'énergie des photons pour le copper. Tiré de Krause et al. [48]

Sections efficaces

Pour comprendre le calcul du rendement des rayons X, le concept de section efficace est essentiel. Il quantifie la probabilité d'une interaction particulière. Bien qu'on puisse l'imaginer comme une surface cible, la réalité quantique est plus complexe. Ce travail utilise des sections efficaces totales, qui somment les probabilités de toutes les interactions possibles.

Principes du calcul du rendement XRF

Pour le calcul du rendement XRF, l'épaisseur de l'échantillon est cruciale. Un échantillon "épais" atténue complètement le rayonnement incident, tandis qu'un échantillon "mince" entraîne une perte d'énergie négligeable (définie ici comme <5%) [9, 31]. Pour des rayons X de 8.058 keV, cela correspond à une couche de Cu de ∼1.25 µm ou une couche de Ti de ∼570 nm. L'"épaisseur" pertinente est l'épaisseur effective, où la particule est complètement absorbée. Elle dépend de la particule, de son énergie et du matériau

de l'échantillon. Les échantillons épais nécessitent de considérer la fluorescence secondaire et l'auto-absorption, mais offrent une meilleure sensibilité. Les échantillons minces ont l'avantage que l'auto-absorption peut être ignorée et que les sections efficaces restent constantes [9]. L'analyse de cette thèse utilise les deux formalismes en fonction de l'épaisseur effective de la couche. Les calculs sont basés sur les concentrations massiques élémentaires. Une approche par paramètres fondamentaux relie les intensités mesurées des raies X N_{ij} (comptes) à la masse m_j de l'élément j dans l'échantillon [9] :

$$N_{ij} = I_0\, G\, \epsilon_{ij}\, \beta \cdot m_j \cdot \sigma_{ij}(E). \tag{6.3}$$

Ici, G est un facteur géométrique, ϵ_{ij} l'efficacité de détection, σ_{ij} la section efficace de fluorescence, et β le terme de correction pour l'auto-absorption :

$$\beta = \frac{1 - \exp\left[-(\mu_i \csc\phi - \mu_f \csc\psi)M\right]}{(\mu_i \csc\phi - \mu_f \csc\psi)M}, \tag{6.4}$$

avec M étant la masse totale de l'échantillon, $\frac{\mu_i}{\mu_f}$ les coefficients d'absorption massique à l'énergie incidente et fluorescente et $\frac{\phi}{\psi}$ l'angle rasant d'incidence/fluorescence. La section efficace de fluorescence de la couche K est calculée comme suit [51] :

$$\sigma_{ij} = \sigma_K \cdot \omega_K \cdot F_{Kj}, \tag{6.5}$$

où σ_K est la section efficace de photo-ionisation, ω_K le rendement de fluorescence (probabilité d'émission), et F_{Kj} le taux d'émission fractionnaire. Toutes les valeurs nécessaires sont disponibles dans des bases de données. L'incertitude combinée pour les calculs de rendement basés sur l'intensité K_α est d'environ 5 % [51]. Le formalisme de la cible épaisse pour la XRF est utilisé lorsque les rayons X incidents sont complètement atténués. L'analyse ne nécessite que la profondeur effective t_{eff}, au-delà de laquelle les rayons X sont soit absorbés, soit ne peuvent s'échapper. Elle est définie comme [9] :

$$t_{\text{eff}}(h\nu_{K_{\alpha/\beta}}) = \beta \times t = \frac{1 - \exp\left(-\left(\frac{\mu_\gamma}{\cos\theta_1} + \frac{\mu_x}{\cos\theta_2}\right)\rho t\right)}{\left(\frac{\mu_\gamma}{\cos\theta_1} + \frac{\mu_x}{\cos\theta_2}\right)}. \tag{6.6}$$

μ_γ et μ_x sont les coefficients d'absorption massique pour les rayons X entrants et sortants, respectivement. Le rendement de la cible épaisse peut alors être calculé comme suit [9] :

$$Y_{x,i} = \frac{\Omega}{4\pi} N_A \frac{m_j}{M_j} \epsilon_{ij} \left[N_{\mathrm{K}_\alpha} \sigma_j(h\nu_{\mathrm{K}_\alpha}) t_{\text{eff}}(h\nu_{K\alpha}) + N_{\mathrm{K}_\beta} \sigma_j(h\nu_{K\beta}) t_{\text{eff}}(h\nu_{\mathrm{K}_\beta})\right]. \tag{6.7}$$

Pour ces calculs, on suppose un échantillon homogène. Il est important de noter que les rayons X caractéristiques ne peuvent être produits que si l'énergie du rayonnement incident est supérieure à l'énergie de liaison des électrons de l'élément dans l'échantillon.

Diffraction élastique

Les rayons X peuvent être diffractés par un échantillon cristallin et retourner vers le détecteur par interférence constructive. Cela peut faire apparaître des pics de rayons X provenant de la cible d'interaction laser dans le spectre, même si cet élément n'est pas présent dans l'échantillon. Si l'échantillon contient le même élément, ce signal de diffraction est indiscernable de la fluorescence de l'échantillon, ce qui entraîne une surestimation. Par conséquent, l'intensité diffractée doit être calculée et soustraite pour une analyse précise [52, 53]. Les calculs supposent un faisceau monochromatique frappant un échantillon de poudre, constitué de nombreux petits cristaux orientés aléatoirement. Cette orientation aléatoire garantit que certains plans cristallins (hkl, indices de Miller [52]) seront toujours correctement alignés pour produire une réflexion de Bragg, comme décrit à l'Equation 6.9. Par exemple, avec une cible de copper (courante au laboratoire ALLS) et un angle de 90° entre les faisceaux incident et sortant, la loi de Bragg indique que les plans 311 et 131 (voir Figure 6.5) satisferont la condition de réflexion.

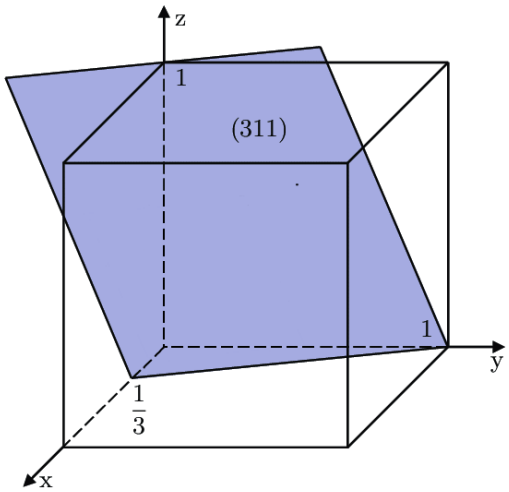

FIGURE 6.5 Le plan cristallographique 311. Le plan 113 est similaire mais orienté le long d'un axe différent [54]

$$2d \cdot \sin(\theta) = n \cdot \lambda \tag{6.8}$$

$$d_{hkl} = \frac{a}{\sqrt{h^2 + k^2 + l^2}} \tag{6.9}$$

La puissance totale diffractée P par la réflexion sur un plan (hkl) donné est décrite comme suit [52] :

$$P = \frac{I_0}{16\pi R} \cdot \left(\frac{e^4}{m^2 c^4}\right) \cdot \frac{V \lambda^3 m_{hkl} F_{hkl}^2}{v_a^2} \cdot \left(\frac{1 + \cos^2(2\theta)}{2\sin(\theta)\sin(2\theta)}\right), \tag{6.10}$$

où V est le volume cristallin effectif, I_0 l'intensité initiale, m_{hkl} le facteur de multiplicité, F_{hkl} le facteur de structure, et λ la longueur d'onde des rayons X. Le terme $\left(\frac{e^4}{m^2c^4}\right)$ provient de la diffusion Thomson. Le facteur de multiplicité tient compte de la symétrie. Pour le copper, avec sa structure cubique à faces centrées (cfc), le facteur de multiplicité pour la famille de plans 113,131 et 311 est de 24.
Le facteur de structure F_{hkl} est l'onde résultante diffusée par tous les atomes d'une maille. Pour une réflexion de Bragg sur le copper, il est simplement $F = 4 \cdot f$, où f est le facteur de structure cristallin et 4 est le nombre d'atomes dans une maille cfc. Le dernier terme de l'Equation 6.10 est un facteur de polarisation. Comme l'Equation 6.10 donne la puissance par unité de longueur, elle doit être ajustée pour la géométrie du détecteur en multipliant par la surface du cône de diffraction à la distance du détecteur. La diffusion inélastique (Compton) peut également se produire. Contrairement à la diffusion élastique, elle est incohérente et produit un fond diffus dans le spectre des rayons X, qui est souvent perdu dans le bruit. Ses effets sur la mesure sont minimes et peuvent être calculés à l'aide d'une approche de mécanique ondulatoire [52].

Fluorescence secondaire

La fluorescence secondaire est une autre source de rendement en rayons X en PIXE et XRF. Ce phénomène se produit lorsque les rayons X caractéristiques d'un élément excitent un autre élément de l'échantillon, qui émet à son tour ses propres rayons X. Par exemple, dans un alliage iron-chromium, les rayons X Fe K_α (6.40 keV) peuvent exciter le chromium (énergie de liaison de la couche K > 5.989 keV), produisant des rayons X secondaires Cr K_α (5.41 keV). Cela augmente le signal Cr mesuré tout en réduisant le signal Fe détecté, ce qui complique l'analyse [9,56]. Négliger cet effet, en particulier dans les systèmes multicouches, peut entraîner des erreurs importantes dans l'estimation de la composition élémentaire.

Mécanismes d'interaction des protons avec la matière

Cette section présente la théorie de l'interaction des protons avec les solides, établissant les bases pour les calculs utilisés dans l'analyse de spectre par *MATLAB* discutée au section 6.3.

Dépôt d'énergie et pouvoir d'arrêt

Le ralentissement des ions dans la matière chaude est bien compris et essentiel pour le sondage des matériaux, car la perte d'énergie en fonction de la profondeur est la clé de l'analyse quantitative. La physique peut être décrite avec précision [44], mais des calculs détaillés ne sont pas nécessaires pour cette thèse. Les calculs se concentrent sur le pouvoir d'arrêt S, qui relie la perte d'énergie $d\epsilon$ d'une particule à la distance parcourue x dans le matériau [31, 57] :

$$S(E) = -\frac{d\epsilon}{dx}. \tag{6.11}$$

Les particules chargées perdent de l'énergie par collisions inélastiques (arrêt électronique), collisions nucléaires élastiques et Bremsstrahlung. Pour les particules massives > 0.4 MeV, l'arrêt électronique domine, car l'arrêt nucléaire et le Bremsstrahlung sont négligeables ($\sim 0.1\%$) [58]. Ce processus est décrit par la formule de Bethe-Bloch [59] :

$$S = -\frac{d\epsilon_K}{dx} = 4\pi\frac{N_A\rho}{M}\left(\frac{e^2}{4\pi\epsilon_0}\right)^2\frac{z^2Z}{m_e v^2\beta^2}\left[\ln\left(\frac{2m_e v^2\beta^2}{I(1-\beta^2)}\right) - \beta^2 - \frac{C}{Z} - \frac{\delta}{2}\right], \tag{6.12}$$

où N_A est la constante d'Avogadro, ρ la densité, M la masse molaire, m_e et e la masse et la charge de l'électron respectivement, z et v la charge et la vitesse de la particule, Z le numéro atomique et β la vitesse relative à celle de la lumière dans le vide. Cette version inclut des corrections de couche ($\frac{C}{Z}$) et de densité ($\delta/2$), tenant compte respectivement de la vitesse élevée des particules et de la polarisation diélectrique [60]. Le pouvoir d'arrêt est utilisé pour calculer la dose macroscopique déposée D à l'aide de la fluence des particules

ϕ :

$$D = \frac{\epsilon_{\text{dep}}}{m} = S(\epsilon_{K,0}, x, z, Z) \cdot \phi. \tag{6.13}$$

Le calcul de l'Equation 6.12 pour les protons résulte en une perte d'énergie en fonction de la profondeur, illustrée à la Figure 6.6.

Figure removed due to copyrights issues

FIGURE 6.6 Percentage Depth Dosage (PDD) de différents types de faisceaux de particules dans l'eau, tiré de [22]. **(a)** photons, **(b)** électrons, **(c)** neutrons, et **(d)** particules lourdes chargées. L'axe y est la PDD en pourcentage, et l'axe x la profondeur de pénétration.

Comme le montre la Figure 6.6, la caractéristique dose-profondeur dépend du type de particule. Contrairement aux photons ou aux électrons, les particules lourdes comme les protons déposent la majeure partie de leur énergie à la fin de leur parcours (Figure 6.6(d)). Ce pic dans la PDD est appelé pic de Bragg [22]. Sa position est contrôlée par l'énergie initiale du proton, ce qui permet de cibler précisément l'endroit où les rayons X sont générés. La largeur du pic est due à la fluctuation de parcours ("range straggling"), un effet statistique dû aux événements de diffusion aléatoires.

Figure removed due to copyrights issues

FIGURE 6.7 Forme du pic de Bragg en fonction de la distance parcourue par les protons dans un échantillon, tiré de [44]. Il montre la dose d'énergie déposée en fonction de la distance pour des énergies de protons de 69 à 231 MeV.

Comme le montre la Figure 6.7, avec une profondeur de pénétration croissante, le pic de Bragg devient plus bas et plus large. Cela est dû au fait que l'énergie du proton diminue, ce qui augmente le pouvoir d'arrêt du matériau, tandis que la diffusion multiple élargit la fluence du faisceau. Les expériences à l'Advanced Laser Light Source (ALLS) (voir section 6.3) utilisent des énergies plus faibles (jusqu'à 6.5 MeV) que celles présentées, ce qui garantit des pics plus nets et un meilleur contrôle de la profondeur.

Principes du calcul du rendement PIXE

Le calcul du rendement PIXE utilise la même approche par paramètres fondamentaux que la XRF, où le rendement est proportionnel à la concentration massique. Pour les échantillons minces, où les particules perdent peu d'énergie, le rendement est calculé comme suit [9, 31] :

$$Y_{x_i}(Z, E_0) = \sigma_{x_i}(Z, E_0) \cdot (nt') \cdot N_p \cdot \epsilon_{x_i}, \tag{6.14}$$

où σ_{x_i} est la section efficace de production induite par les protons [62], nt' la densité surfacique, et N_p le nombre de protons. Pour un spectre de protons continu, ceci doit être intégré sur la gamme d'énergie pertinente. Pour les échantillons épais, où les protons s'arrêtent complètement, le calcul du rendement nécessite une intégration sur la perte

d'énergie [9] :

$$Y_{p,i} = \frac{\Omega}{4\pi} N_A M_j m_j \int_{E_0}^{E_1} f_p(E_p) \int_{E_p}^{0} \sigma_j(E)\, \omega_j\, T_j(E)\, \frac{dE}{S(E)} dE_p \tag{6.15}$$

$$T_j(E) = \exp\left(-\mu_j \int_{E_p}^{E} \frac{dE'}{S(dE')} \frac{\cos\theta_1}{\cos\theta_2}\right), \tag{6.16}$$

où $f_p = \frac{dE\, d\Omega}{d^2 N}$ est la distribution large en énergie des protons de l'installation décrite au section 6.3, σ_i la section efficace d'ionisation [63], $S(E)$ le pouvoir d'arrêt du proton (calculé avec *SRIM* [50]), et $T_j(E)$ le terme d'atténuation des rayons X.
Cette analyse devrait avoir un niveau de confiance d'environ 5%, bien que cela dépende de facteurs expérimentaux [9]. L'objectif est d'analyser des échantillons de composition inconnue. Comme certains calculs (comme la diffraction) nécessitent cette information, un processus itératif de mesure et d'analyse est nécessaire, en particulier pour les échantillons multicouches. Des solutions potentielles sont discutées dans le chapitre suivant.

Bremsstrahlung

En plus des raies caractéristiques, les électrons génèrent un spectre de rayons X continu via le Bremsstrahlung lorsqu'ils sont déviés par un noyau atomique. Le spectre résultant se superpose aux raies caractéristiques (Figure 6.8) et peut également être utilisé pour l'analyse XRF [2, 9, 31, 57].

Figure removed due to copyrights issues

FIGURE 6.8 Un spectre d'émission typique d'un tube à rayons X. Le spectre continu de Bremsstrahlung est réabsorbé à plus basse énergie [65].

La contribution du Bremsstrahlung augmente avec le numéro atomique. Pour une cible de

copper, son rendement est comparable à celui du K_α [66]. Cependant, comme la section efficace XRF est beaucoup plus faible à haute énergie, la contribution du Bremsstrahlung est initialement négligée dans cette thèse. Pour les expériences sur les aérosols utilisant une cible de tantalum, le rendement du Bremsstrahlung ne peut plus être négligé et son influence sera discutée plus en détail dans le chapitre suivant.

6.3 Montage expérimental et méthodologie

Ce chapitre présente le montage expérimental ainsi que le code d'analyse *MATLAB*. Ensemble, ils constituent la base de l'analyse multicouche. Le montage comprend quatre parties principales : la chambre de la source de protons Target Normal Sheath Acceleration (TNSA), un sélecteur d'énergie, la chambre d'échantillonnage, et les diagnostics pour les rayons X et les protons. La section sur le code couvrira l'identification des pics et l'implémentation des équations physiques pour obtenir des résultats quantitatifs.

Montage expérimental

Le cœur de la ligne de faisceau ALLS est un laser Ti :Saphir de 150 TW (longueur d'onde centrale de 800 nm, taux de répétition de 2.5 Hz). Après compression, il délivre des impulsions de 22 fs (Full Width Half Maximum (FWHM)), qui sont guidées dans la chambre principale. Le montage est illustré au Figure 6.9.

Chambre principale

Le faisceau à polarisation p (diamètre de 100 mm) est focalisé par une parabole hors-axe f/3 sur une tache de 5 µm sur une cible en feuille mince de haute pureté (ex. ∼5 µm). Un porte-cible motorisé avec une matrice de 400 trous permet des tirs répétés et rapides. Le vide de la chambre est $< 10^{-6}$ mbar. Le faisceau de protons, produit par TNSA, se

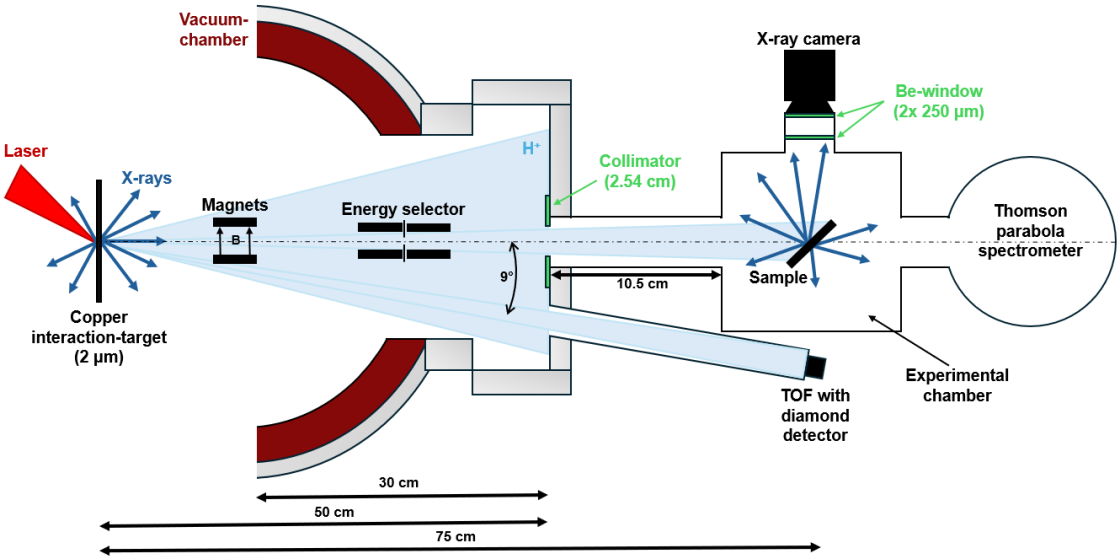

FIGURE 6.9 Schéma des principaux composants montrés à la **??**

propage normalement à la cible. Deux aimants (0.1 T), à 20 cm de la source, dévient les électrons co-mobiles jusqu'à 10 MeV, tandis que les protons plus massifs sont moins affectés. Le système est d'abord aligné avec un laser rouge. Le faisceau laser principal est ensuite optimisé à l'aide d'un miroir déformable pour obtenir un front d'onde plat,

surveillé par un capteur de front d'onde et une caméra Charge Coupled Device (CCD). Une fois réglés, ces paramètres restent fixes pour toute l'expérience XPIF.

Sélecteur d'énergie

Le "sélecteur d'énergie", montré en Figure 6.10, un dispositif passif compact conçu par Chen et al. au LULI [78], est placé après les aimants pour contrôler la largeur de bande énergétique du faisceau de protons. Il utilise quatre jeux d'aimants de 1 T et des fentes pour d'abord disperser le faisceau par énergie, sélectionner une plage d'énergie spécifique, puis le recombiner sur l'axe d'origine. La déflexion est régie par la force de Lorentz [79] :

$$F = q \cdot \vec{v} \times \vec{B}, \tag{6.17}$$

où q est la charge du proton, $\vec{v}$ sa vitesse, et $\vec{B}$ le champ magnétique.

Figure removed due to copyrights issues

FIGURE 6.10 Dessin CAO du sélecteur d'énergie montrant l'orientation du champ magnétique et les trajectoires prédites des ions. Tiré des travaux de Chen et al. [78].

La simulation SIMON de la Figure 6.11 montre les trajectoires des protons de 100 keV à 1 MeV. Conformément à la Equation 6.17, la force de Lorentz dévie davantage les protons de plus basse énergie, tandis que les protons de plus haute énergie sont regroupés plus étroitement en raison de la dépendance non linéaire de la force avec l'énergie. Ces observations seront vérifiées expérimentalement au section 6.4.

Figure removed due to copyrights issues

FIGURE 6.11 Simulation SIMON des trajectoires de protons entre 100 keV et 1 MeV. Tiré des travaux de Chen et al. [78].

Chambre expérimentale

Les échantillons sont montés dans une petite chambre en aluminium, connectée à la chambre principale mais avec un vide séparé ($\sim 10^{-6}$ mbar) pour permettre des changements rapides d'échantillons. Elle est isolée par une fenêtre en Kapton® de 7.5 µm et une vanne-porte. Les échantillons solides sont montés sur un support à un angle de 45° par rapport au faisceau de protons incident et à la caméra à rayons X, comme le montre la Figure 6.12.

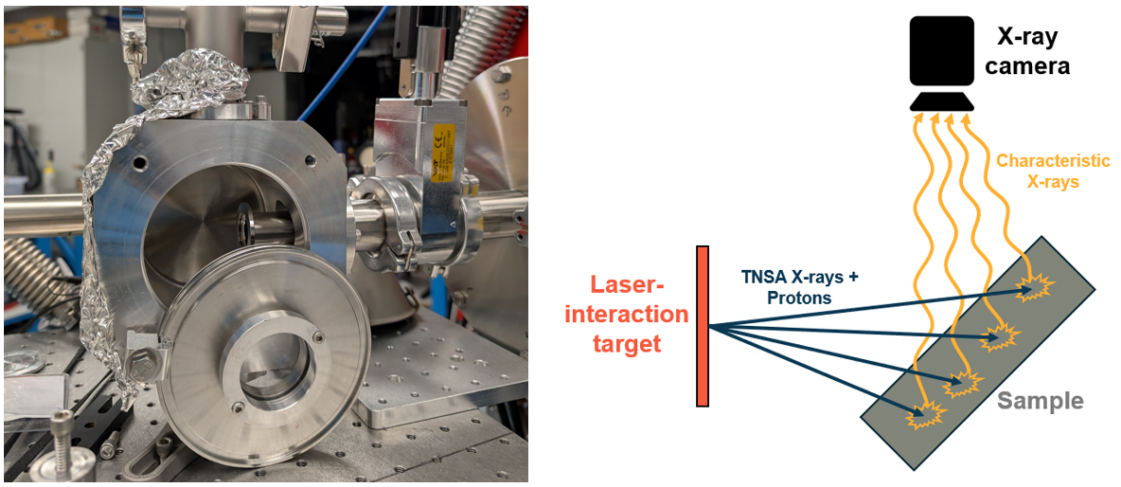

FIGURE 6.12 Gauche : Photo de la chambre d'échantillonnage. Droite : Schéma de l'orientation de l'échantillon par rapport au faisceau de protons et à la caméra à rayons X.

Pour les expériences avec des gaz, comme le krypton (Kr), la chambre est évacuée, remplie avec une pression partielle précise du gaz, puis pressurisée à la pression ambiante avec de l'azote. La concentration est surveillée avec une jauge à vide et calculée à l'aide de la loi des gaz parfaits :

$$pV = nRT. \tag{6.18}$$

Thomson Parabola

Un spectromètre à parabole de Thomson (Thomson Parabola (TP)) [83] est utilisé pour acquérir le spectre de protons du processus TNSA. Il utilise des champs électrique (E) et magnétique (B) parallèles pour dévier les ions sur un détecteur (voir Figure 6.13). Les ions ayant le même rapport charge/masse ($\frac{Z}{M}$) suivent une parabole distincte, permettant leur identification. La déflexion en x et y est décrite par [84] :

$$x = Ze \cdot \frac{E}{E_i} \frac{lD}{2}, \tag{6.19}$$

$$y = Ze \cdot \frac{B}{\sqrt{ME_i}} \frac{lD}{\sqrt{2}}, \tag{6.20}$$

où E_i est l'énergie de la particule.

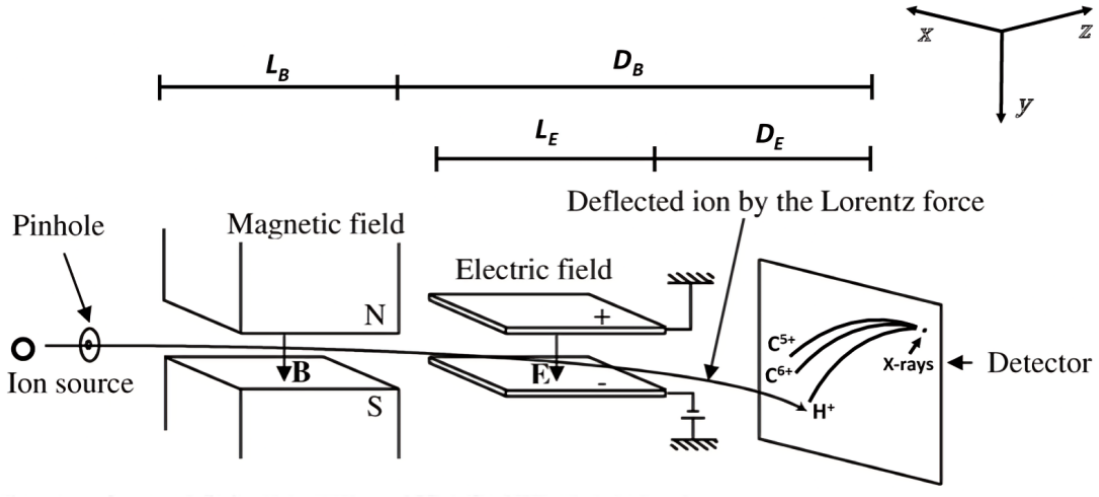

FIGURE 6.13 Schéma et principe de fonctionnement d'un spectromètre à parabole de Thomson, tiré de Vallières [40].

Le spectre final de protons, montré à la Figure 6.14, est une moyenne de plusieurs tirs et sert de base pour les calculs de rendement ultérieurs. Deux éléments de cible ont été utilisés : le copper (Cu) pour les échantillons métalliques multicouches et le tantalum pour l'étude des aérosols de Kr. L'utilisation d'une feuille de Ta a produit un rendement global de protons 9% plus élevé et une énergie de coupure supérieure d'environ 7 MeV, contre 5 MeV pour le cuivre.

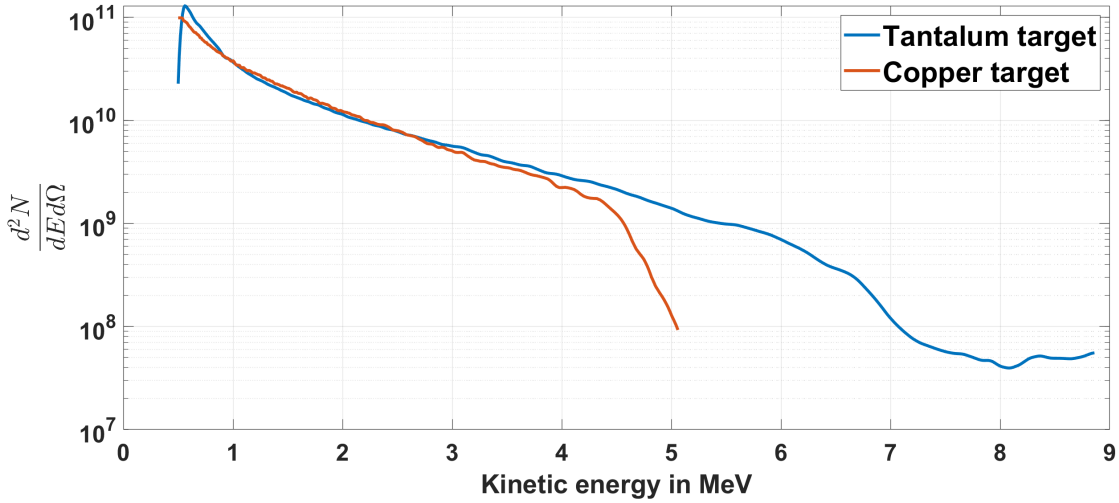

FIGURE 6.14 Spectres de protons pour le Ta (moyenne de 38 tirs) et le Cu (10 tirs). Les barres d'erreur de ±15% sont omises pour plus de clarté.

Détecteurs à temps de vol

Deux détecteurs à diamant à Time of flight (ToF) sont utilisés pour vérifier les mesures du TP. En se basant sur le temps que met un ion à parcourir une distance connue, son énergie cinétique peut être calculée :

$$E_{\text{kin}} = (\gamma - 1)M_p c^2, \qquad \gamma = \frac{1}{\sqrt{1-\beta^2}}, \qquad \beta = \frac{L}{c \cdot ToF}, \tag{6.21}$$

où L est la longueur du trajet de vol.

Caméra à rayons X

Pour la spectroscopie de rayons X, une caméra PI-LCX :1300 refroidie à l'azote liquide est utilisée, placée à 90° par rapport au faisceau de protons. Cette caméra à illumination frontale possède une matrice de 1340×1300 pixels sur une puce de silicon (Si) de 50 µm. Elle a une bonne efficacité de détection entre 2.5 et 20 keV. À 12.6 keV (la raie K_α du Kr), la caméra a une résolution de 0.222 keV, calculée comme suit [91] :

$$\Delta E = 2.35 \cdot 3.65\sqrt{N^2 + \frac{F \cdot E}{3.65}}, \tag{6.22}$$

avec F étant le facteur de Fano, N le bruit de lecture, et E l'énergie. Le spectre final analysé par le code *MATLAB* est accumulé sur plusieurs tirs.

Méthodologie

Cette section détaille le programme *MATLAB* personnalisé pour l'analyse quantitative et multicouche. Le code, basé sur une version initiale de Bovin et al. [2] pour des échantillons homogènes, a été considérablement étendu. La routine originale n'exploitait pas les caractéristiques uniques du dépôt d'énergie des protons décrites au section 6.2, était limitée à une cible en copper et ne supportait que quelques éléments. Pour permettre une analyse couche par couche, le code a nécessité des mises à jour majeures pour gérer à la fois les protons et les rayons X, ainsi que les spectres de protons continus et à bande étroite. Une nouvelle routine a été développée pour cette thèse afin d'effectuer une analyse multicouche. Elle itère sur plusieurs mesures, en utilisant les résultats des couches précédentes pour calculer l'atténuation et le rendement des couches suivantes. Les calculs incluent la PIXE, la XRF et la diffraction des rayons X, et peuvent utiliser soit un spectre de protons complet (comme dans la Figure 6.14), soit des spectres étroits du sélecteur d'énergie. Un système de tables de consultation évolutif a été implémenté pour gérer la complexité accrue des matériaux et des éléments. Cependant, la différence entre l'analyse qualitative et quantitative sera d'abord brièvement expliquée.

Analyse qualitative et quantitative

L'analyse qualitative identifie les éléments constitutifs d'un échantillon par leurs empreintes de rayons X caractéristiques (raies $K_{\alpha,\beta}$) et est un prérequis à l'analyse quantitative. Le principal défi est de différencier les pics qui se chevauchent, comme un pic K_β fort d'un élément masquant un pic K_α plus faible d'un autre, ou des pics L dominés par des pics K. La résolution du détecteur est donc essentielle. Des algorithmes d'ajustement sont utilisés pour déconvoluer ces pics [9]. L'analyse quantitative, plus complexe, détermine avec précision la concentration de chaque composant. Elle nécessite un étalonnage avec des standards de référence. Pour cette thèse, la caméra a été étalonnée à l'aide d'échantillons de haute pureté de titanium (4.51 keV), nickel (7.48 keV), copper (8.05 keV), zinc (8.64 keV), niobium (16.62 keV), molybdène (17.48 keV) et argon (22.16 keV) [90]. Cela fournit un ajustement par régression linéaire pour les données. Une analyse quantitative précise doit également tenir compte d'effets tels que la diffraction, les pics d'échappement et les événements d'empilement, qui sont détaillés dans la section suivante. Le code *MATLAB* présenté dans ce chapitre est conçu pour effectuer les deux types d'analyse.

Analyse des données avec *MATLAB*

La routine *MATLAB* requiert trois entrées : le spectre de rayons X mesuré, le rendement en protons/rayons X de la source TNSA, et divers paramètres expérimentaux (ex : épaisseur de l'échantillon, orientation, efficacité de la caméra). Le flux de travail de base est

illustré à la Figure 6.15.

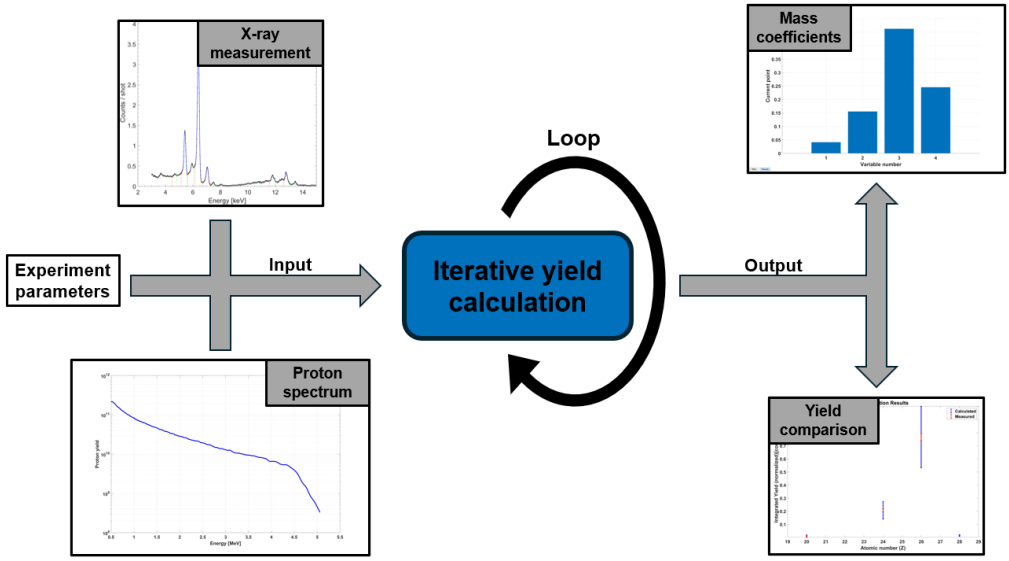

FIGURE 6.15 Schéma du code *MATLAB* personnalisé illustrant les entrées et sorties de la procédure

Le code identifie d'abord les éléments présents dans l'échantillon à partir du spectre de rayons X. Il calcule ensuite de manière itérative le rendement théorique pour chaque élément et optimise une fonction de coût pour trouver les rapports de masse qui décrivent le mieux les données expérimentales. Pour l'analyse multicouche, ce processus est répété en boucle couche par couche, en incluant les effets d'atténuation des couches précédentes. Le résultat final fournit les rapports de masse calculés et une comparaison entre les rendements théoriques et mesurés, indiquant la qualité de l'ajustement.

Traitement des données de la caméra à rayons X

L'image en niveaux de gris 16 bits du détecteur de rayons X (1300×1340 pixels) est convertie en un spectre d'énergie. La Figure 6.16 montre un exemple de cette conversion.

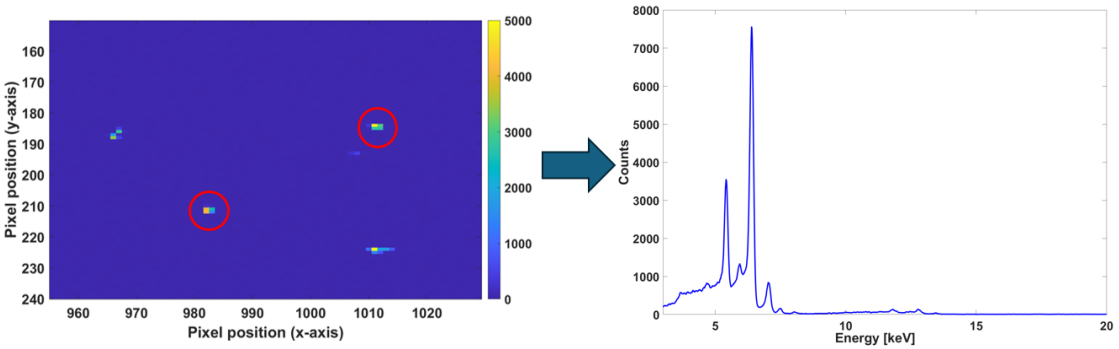

FIGURE 6.16 Droite : Un extrait de l'image enregistrée par la caméra CCD. Gauche : Le spectre de rayons X résultant après conversion. Les cercles rouges marquent des événements trop rapprochés pour être considérés comme un Single Pixel Event (SPE).

D'abord, le code lit le fichier de données ".SPE" et soustrait le bruit de fond mesuré. Ensuite, un algorithme de filtrage d'Événements à Photon Unique (Single Pixel Event (SPE)) est appliqué [94,95]. Il identifie les "vrais" photons en vérifiant si un pixel illuminé est isolé et dépasse un seuil défini par le bruit de fond :

$$\text{threshold} = \overline{Y}_{\text{background}} + 3\sigma. \tag{6.23}$$

Cela améliore la résolution en énergie au détriment des statistiques de photons. Les valeurs de gris filtrées sont ensuite converties en énergie de photon à l'aide des données d'étalonnage de la section 6.3 et de la transformation suivante [95] :

$$\frac{dN}{dE} = \frac{a}{k_1(E) \cdot QE(E) \cdot T(E) \cdot \Omega_c} \cdot \frac{dN_{\text{SPE}}}{dE}, \tag{6.24}$$

où $QE(E)$ est l'efficacité quantique, Ω_c l'angle solide, $T(E)$ la transmission de la fenêtre, et $k_1(E)$ la probabilité de détection SPE. L'utilisateur peut optionnellement appliquer une courbe de correction et supprimer manuellement les raies de contaminants connus (par ex. le iron ou le chromium (Cr) de la chambre). Les pics du spectre résultant sont identifiés en comparant leurs énergies à une base de données [90]. Ceci est compliqué par le chevauchement de pics (par ex. titanium K_β et vanadium K_α) qui peuvent être en dessous de la résolution du détecteur. Les artéfacts courants comme les pics d'échappement (à $E - 1.7$ keV pour un détecteur en Si) et les événements d'empilement (pics de somme) sont également pris en compte. Le code vérifie ces problèmes ainsi que la présence de rayons X diffusés élastiquement par la cible laser pour éviter une mauvaise identification.

Pour calculer le rendement intégré, chaque pic est ajusté avec une fonction gaussienne, lorentzienne ou triangulaire. En cas d'échec de l'ajustement, une intégration numérique est utilisée. Le bruit de fond sous le pic est estimé à partir de la surface dans les limites de la FWHM, comme le montre l'ajustement gaussien de la Figure 6.17.

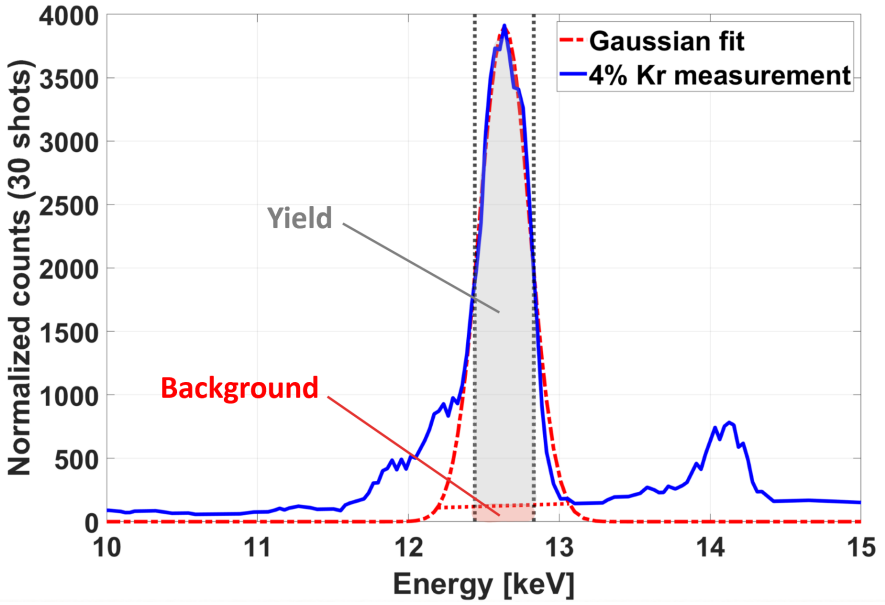

FIGURE 6.17 Ajustement de pic gaussien (ligne pointillée rouge) d'une mesure de Kr K_α (bleu). La zone à l'intérieur de la FWHM (lignes pointillées noires) définit le rendement (gris) et le bruit de fond (rouge).

Les pics sont validés à l'aide de la méthode de la Limite de Détection Minimale (Minimal Detectable Limit (MDL)), où le rendement du pic doit dépasser trois fois la racine carrée du rendement du bruit de fond pour être considéré statistiquement significatif [97] :

$$Y_{\mathrm{MDL}} = 3 \cdot \sqrt{Y_{\mathrm{background}}}. \tag{6.25}$$

Après ce processus automatisé, l'utilisateur a une dernière occasion de corriger ou de supprimer manuellement tout pic identifié sur la base de connaissances préalables de l'échantillon.

Procédure de calcul du rendement

L'utilisateur sélectionne d'abord la gamme d'énergie des protons à utiliser. Le code utilise ensuite la Méthode des Paramètres Fondamentaux (FPM) [9] pour calculer le rendement théorique en rayons X. Bien que moins précise que les méthodes empiriques, la FPM permet l'analyse d'échantillons complètement inconnus sans préparation complexe [98]. Pour l'analyse quantitative, seule la raie K_α de chaque élément détecté est considérée. Les effets de fluorescence secondaire sont actuellement négligés, car ils sont jugés faibles par rapport aux fluctuations tir à tir de la source laser [96]. L'analyse utilise une procédure itérative pour trouver les rapports de masse élémentaires qui décrivent le mieux les données. En partant d'une hypothèse de concentrations égales, le rendement théorique (provenant de la X-Ray Fluorescence (XRF) et de la Particle-Induced X-ray Emission (PIXE)) est calculé, normalisé et comparé au rendement mesuré. L'optimisation est réalisée à l'aide de la fonction *fmincon* de *MATLAB* pour trouver la composition qui décrit le mieux les données expérimentales en minimisant une fonction de coût. La fonction de coût est le paramètre standard χ^2, défini comme :

$$\chi^2 = \sum_i \frac{(Y_{\text{measured}} - Y_{\text{theoretical}})^2}{Y_{\text{measured}}}. \tag{6.26}$$

L'optimisation trouve le meilleur ajustement lorsque χ^2 est inférieur à 10^{-10} pour deux itérations consécutives. La somme des rapports de masse calculés (w_i) est contrainte entre 0.8 et 1 ($0.8 < \sum_i w_i < 1$). Cette contrainte tient compte de la présence potentielle d'éléments légers non détectés (comme H, C, O) qui pourraient constituer le reste de la masse de l'échantillon. Le processus itératif est visualisé à l'aide de diagrammes à barres. Les résultats finaux, montrant les rapports de masse (c_i) et une comparaison des rendements théoriques et mesurés, sont présentés dans une fenêtre comme celle de la Figure 6.18. Cette comparaison indique la qualité de l'ajustement.

Pour tenir compte des fluctuations de la source d'un tir à l'autre, deux paramètres sont introduits : le paramètre a pour les fluctuations de protons (0.75–1.25) et le paramètre b pour les fluctuations de rayons X (0.85–1.15). Ils sont testés dans une boucle imbriquée autour de l'optimisation principale. L'erreur moyenne résultant de ces fluctuations s'est avérée être de 16 %, ce qui suggère que les calculs de coefficient de masse sont robustes face aux erreurs cumulatives de la source [2].

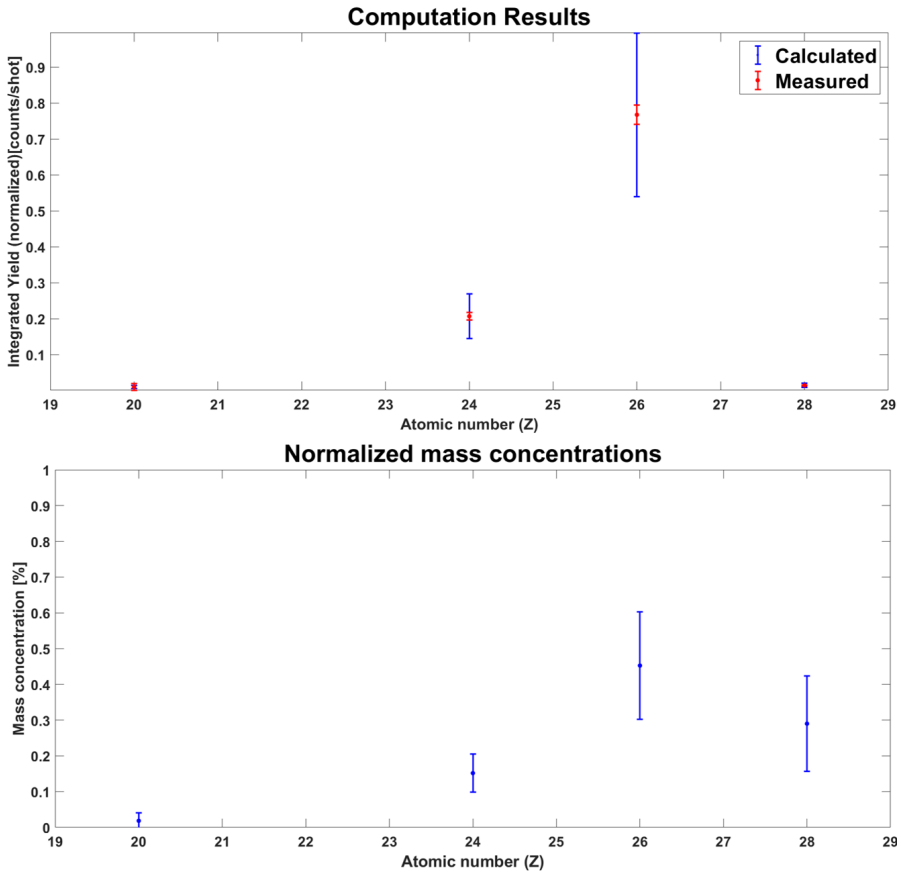

FIGURE 6.18 Résultats de la routine *MATLAB* pour un échantillon d'acier inoxydable. En haut : comparaison des rendements normalisés. En bas : coefficients de masse calculés c_i.

Implémentation de l'analyse couche par couche

Pour analyser des échantillons multicouches, le code a été modifié pour tenir compte des interactions des protons et des rayons X dans chaque couche, car celles-ci altèrent de manière significative le rendement mesuré. Pour les protons, l'élément clé est le calcul de leur perte d'énergie couche par couche. Les protons perdent de l'énergie en traversant la couche supérieure, créant un spectre atténué pour la couche suivante, comme le montre schématiquement la Figure 6.19. Le code sépare le spectre de protons en fonction du parcours calculé dans la couche supérieure. La partie qui s'arrête dans la couche est analysée avec le formalisme PIXE pour cible épaisse du section 6.2, tandis que la partie qui traverse est analysée avec le formalisme pour cible mince. La couche inférieure est ensuite analysée avec le formalisme pour cible épaisse en utilisant le spectre de protons atténué. Pour les rayons X, deux effets doivent être considérés : l'atténuation des rayons X générés dans les couches profondes et la diffraction élastique du faisceau incident par la surface supérieure, comme le souligne la Figure 6.20. Le calcul de la diffraction, détaillé au section 6.2, nécessite une connaissance préalable de la composition de la couche su-

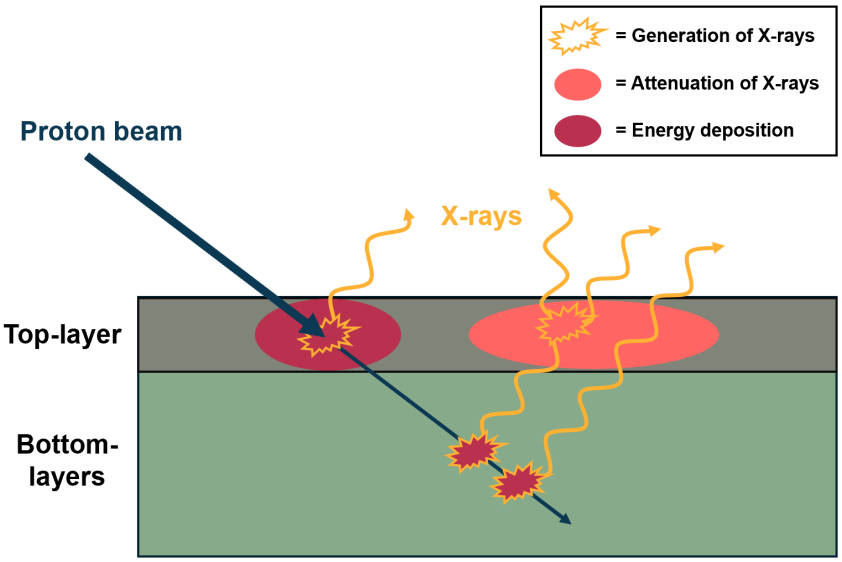

FIGURE 6.19 Schéma de toutes les interactions pertinentes des protons entrants et des rayons X sortants avec un échantillon à deux couches. Le concept est extensible.

périeure, obtenue par des mesures préliminaires. Les rayons X qui ne sont pas diffractés sont alors disponibles pour générer un rendement XRF. Le formalisme XRF pour cible mince est utilisé si la perte d'énergie des rayons X incidents est inférieure ou égale à 5 % ; sinon, le formalisme pour cible épaisse est appliqué. Après le calcul du rendement de la première couche, l'atténuation des rayons X qui la traversent est déterminée à l'aide d'un package *MATLAB* qui implémente la loi de Beer-Lambert. Le rendement de la couche inférieure est ensuite calculé en utilisant le nombre de photons atténués et le formalisme PIXE approprié. Lors de l'analyse d'une couche plus profonde, le code ajoute les rendements des couches supérieures et ajuste de manière itérative les concentrations massiques de la couche actuelle. La composition des couches supérieures est considérée comme fixe pendant ce processus. Cette procédure itérative et extensible est montrée schématiquement à la Figure 6.20. Les rayons X caractéristiques produits dans les couches profondes sont également affectés par les couches supérieures sur leur trajet vers le détecteur. Deux processus sont considérés : l'atténuation, qui peut être significative (par exemple, une couche de Cu de 10 µm bloque 99% des rayons X du Ti), et la fluorescence secondaire. La fluorescence secondaire ne se produit que si les rayons X sont assez énergétiques pour exciter les atomes des couches supérieures (par exemple, les rayons X Ti K α à 4.51 keV ne peuvent pas exciter les électrons de la couche K du Cu à 8.04 keV). Pour les échantillons de plus de deux couches, tout ce processus de calcul de l'atténuation et du dépôt d'énergie est répété séquentiellement pour chaque couche. Pour analyser un échantillon multicouche, l'utilisateur spécifie le nombre de couches et leurs épaisseurs. Le code analyse ensuite chaque couche en boucle, de haut en bas, en utilisant le fichier ".SPE" et

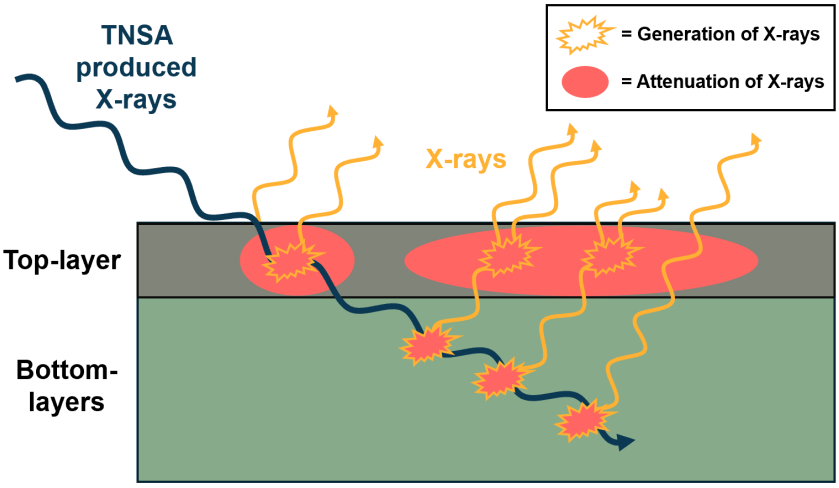

FIGURE 6.20 Représentation schématique mettant en évidence toutes les interactions pertinentes des rayons X entrants et sortants avec l'échantillon.

le spectre de protons correspondants. Les résultats d'une couche sont utilisés pour les calculs d'atténuation de la suivante. Ce processus est en pratique limité à environ quatre couches en raison de la profondeur de pénétration des particules. L'analyse des couches profondes nécessite de connaître les propriétés des couches supérieures, ce qui semble contradictoire pour des échantillons inconnus. Pour résoudre ce problème, une procédure de mesure spécifique est retirée. D'abord, un balayage en énergie est effectué avec le sélecteur d'énergie. L'observation de l'apparition et de la disparition des pics de rayons X donne une estimation initiale de l'épaisseur de chaque couche. Cela permet un sondage ciblé du centre de chaque couche pour déterminer sa composition. Avoir des informations préalables sur l'épaisseur accélère considérablement ce processus. Une fois l'information sur l'épaisseur acquise, l'utilisateur peut régler le sélecteur pour sonder chaque couche individuellement et déterminer sa composition chimique. Alternativement, si l'échantillon entier est irradié avec un spectre de protons continu, l'utilisateur peut entrer manuellement les propriétés connues (composition, épaisseur) de la ou des couche(s) supérieure(s). La routine procède alors à l'analyse des couches plus profondes de la même manière que dans la méthode couche par couche.

Modélisation du spectre de Bremsstrahlung

Comme mentionné au section 6.2, la contribution du Bremsstrahlung est négligeable pour une cible en cuivre mais doit être considérée pour une cible à Z plus élevé comme le Ta. Pour estimer avec précision le rendement XRF dans l'échantillon, le spectre continu de Bremsstrahlung, qui contient une part importante du rendement total en rayons X, doit être reconstruit.

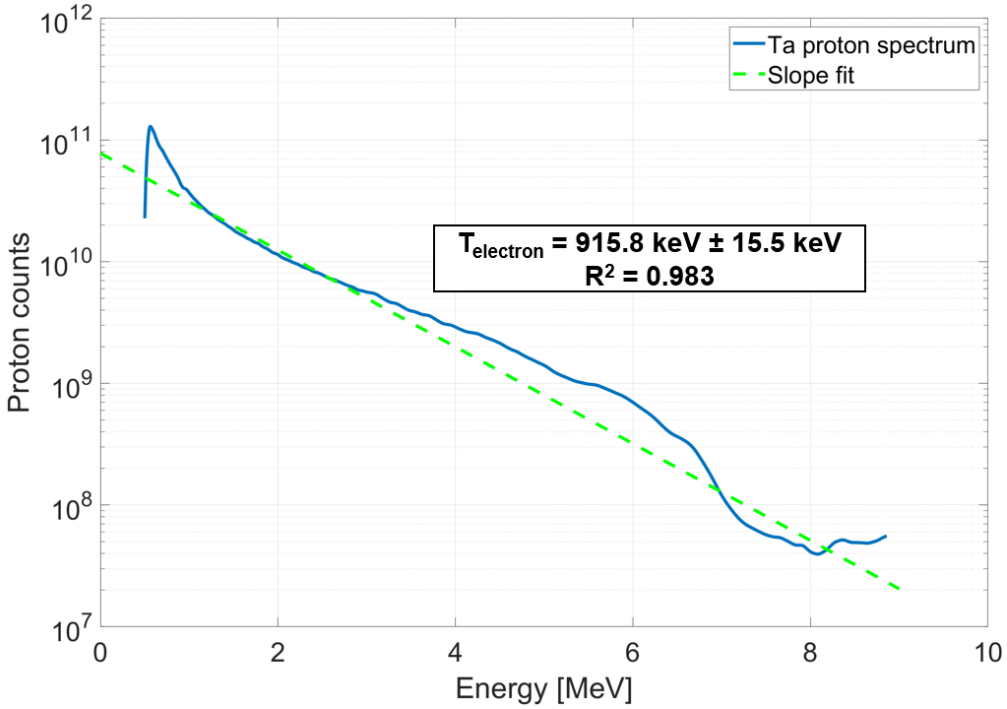

FIGURE 6.21 Ajustement exponentiel (vert) d'un spectre de protons de Ta (bleu) pour estimer l'énergie des électrons chauds. La pente donne une énergie de 915.8 ± 15.5 keV.

L'énergie des électrons chauds est un paramètre clé pour cette reconstruction. Elle est estimée à partir de la pente du spectre de protons mesuré (voir Figure 6.21), donnant une valeur de 915.8 ± 15.5 keV. Ce résultat est cohérent avec des travaux antérieurs [101,102]. La distribution en énergie de ces électrons est approximée par une distribution de Maxwell, comme le montre l'Equation 6.27, bien que d'autres distributions puissent être plus précises [103,105]. À l'aide de ce modèle, le spectre continu de Bremsstrahlung est calculé, comme le montre la Figure 6.22.

$$f(x) = \sqrt{\frac{2}{\pi}} \frac{x^2}{a^3} e^{\frac{-x^2}{2a^2}}, \tag{6.27}$$

Le paramètre a est lié à la température de la distribution. Les rendements caractéristiques K_α et K_β de la feuille de Ta sont estimés séparément à l'aide de données de section efficace

tabulées [106].

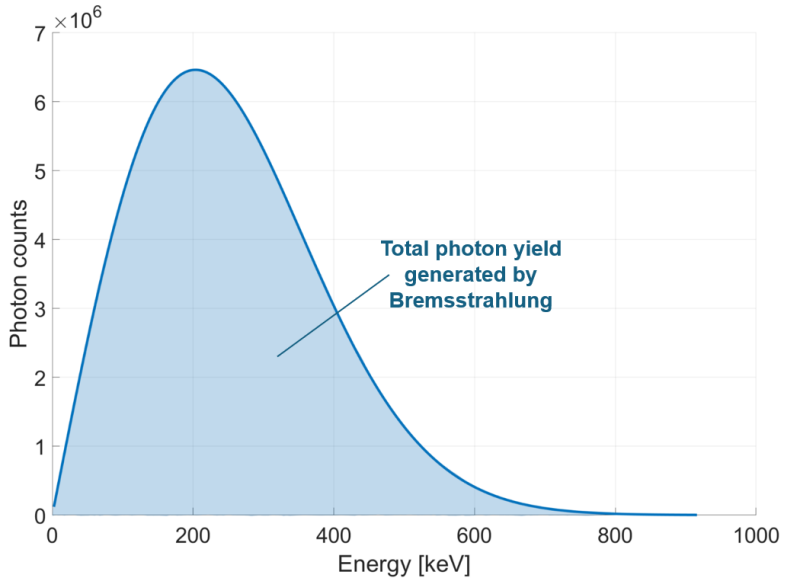

FIGURE 6.22 Spectre de Bremsstrahlung calculé pour le Ta, basé sur le spectre de protons (Figure 6.21) et la distribution maxwellienne supposée.

Les calculs montrent que le Bremsstrahlung représente 84.7 % du total des photons produits par la cible de Ta. Cependant, sa contribution au rendement XRF final dans un échantillon de Kr est beaucoup plus faible. Le rendement XRF par atome induit par les rayons X caractéristiques du Ta ($\sim 1.34 \times 10^{-11} \frac{\text{MeV}\cdot\text{cm}^2}{\text{atom}}$) est supérieur de deux ordres de grandeur à celui induit par le spectre continu de Bremsstrahlung ($\sim 4.69 \times 10^{-13} \frac{\text{MeV}\cdot\text{cm}^2}{\text{atom}}$).

6.4 Résultats et discussion

Une fois la théorie sur le calcul de rendement dans les échantillons multicouches, ainsi que le montage expérimental et le traitement des données de mesure compris, les données recueillies peuvent être entièrement analysées. La présentation des résultats est divisée en trois parties. D'abord, les résultats expérimentaux des tests et de la calibration du sélecteur d'énergie, discuté dans section 6.3, sont présentés. Ensuite, nous validons les calculs et la performance du code *MATLAB* pour l'analyse des spectres de rayons X. Ces étapes préparent le terrain pour de futures expériences utilisant une méthode couche par couche, qui nécessitent le sélecteur d'énergie pour cibler des couches spécifiques et le code pour analyser les données. Finalement, les résultats de l'application de l'X-ray and Particle Induced X-ray Fluorescence (XPIF) à des mélanges gazeux sont présentés, où la dilution d'aérosols de Kr dans l'air a été mesurée à différents niveaux.

Mise en œuvre du sélecteur d'énergie

Avant de commencer les expériences, la fonctionnalité du sélecteur d'énergie de Chen et al. [78] (voir section 6.3) doit être vérifiée sur la ligne de faisceau et avec le montage expérimental actuels à l'ALLS. Ensuite, le sélecteur peut être calibré pour déterminer les positions de fente nécessaires pour diverses énergies centrales et bandes passantes. Comme le Thomson Parabola (TP) ne peut pas être utilisé pendant l'expérience, il est crucial de recueillir ces informations au préalable pour connaître avec précision la profondeur de pénétration lors de la procédure couche par couche.

Vérification et étalonnage

la Figure 6.23 montre l'énergie centrale du spectre de protons en fonction de la position de la fente. La première fente, à travers laquelle les protons entrent dans le sélecteur, a été maintenue complètement ouverte, tandis que la deuxième fente, faite de tantalum (Ta), a été fixée à une ouverture constante de 1 mm. Avec cette configuration, la fente a été déplacée pas à pas sur toute la plage jusqu'à ce que l'énergie maximale des protons soit atteinte. La ligne rouge est uniquement utilisée pour visualiser la relation non linéaire entre les deux paramètres. L'observation principale est que pour atteindre des énergies centrales croissantes, la fente doit être déplacée sur une plus grande distance. Ceci s'explique par le fait que, comme discuté dans la section 6.3, les protons sont plus fortement déviés pour des énergies cinétiques plus faibles. la Figure 6.24 décrit la relation entre l'énergie centrale et la largeur de bande du spectre de protons transmis, comme le montre la Figure 6.25. La procédure expérimentale était identique à celle utilisée pour l'acquisition des données de la Figure 6.23. En suivant la visualisation de la dépendance entre l'énergie centrale et la largeur de bande (rouge), on observe que la largeur de bande augmente avec l'énergie centrale. Ce comportement non linéaire résulte de la force de

Lorentz, qui varie de manière non linéaire avec l'énergie des particules, entraînant un regroupement à des énergies de protons plus élevées.

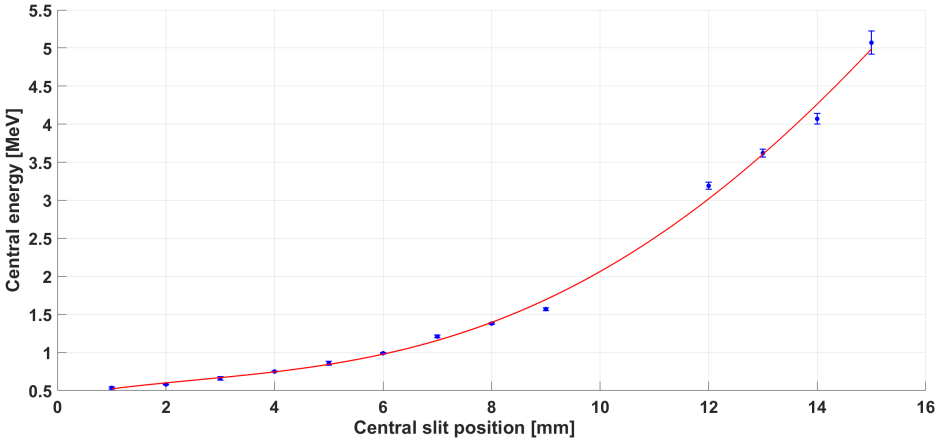

FIGURE 6.23 Énergie centrale des protons que le sélecteur laisse passer en fonction de l'emplacement de la fente secondaire en tantalum par rapport à l'axe du faisceau incident (bleu). La ligne rouge est une visualisation de la relation changeante entre l'énergie centrale et la position centrale de la fente. L'ouverture de la fente en tantalum a été maintenue à 1 mm.

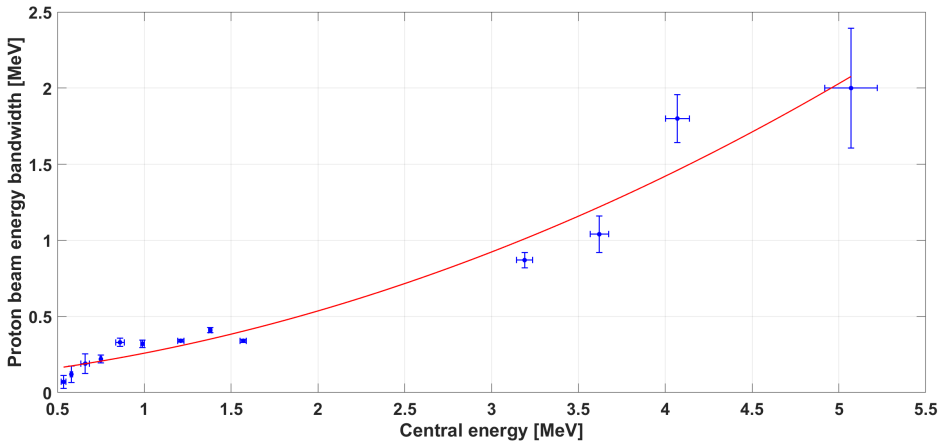

FIGURE 6.24 Largeur de bande énergétique du spectre de protons après passage à travers le sélecteur en fonction de l'énergie centrale (bleu). L'ouverture de la fente en tantalum a été maintenue à 1 mm.

la Figure 6.25 montre les spectres de protons, produits durant les expériences, qui ont été utilisés pour générer les figures Figure 6.23 et Figure 6.24. Les spectres présentent à la fois les caractéristiques observées dans les figures précédentes ainsi que dans les simulations SIMON (Figure 6.11) par Chen et al. [78] : la distance accrue nécessaire pour des énergies centrales plus élevées, ainsi qu'une largeur de bande plus importante avec l'augmentation

de l'énergie centrale.

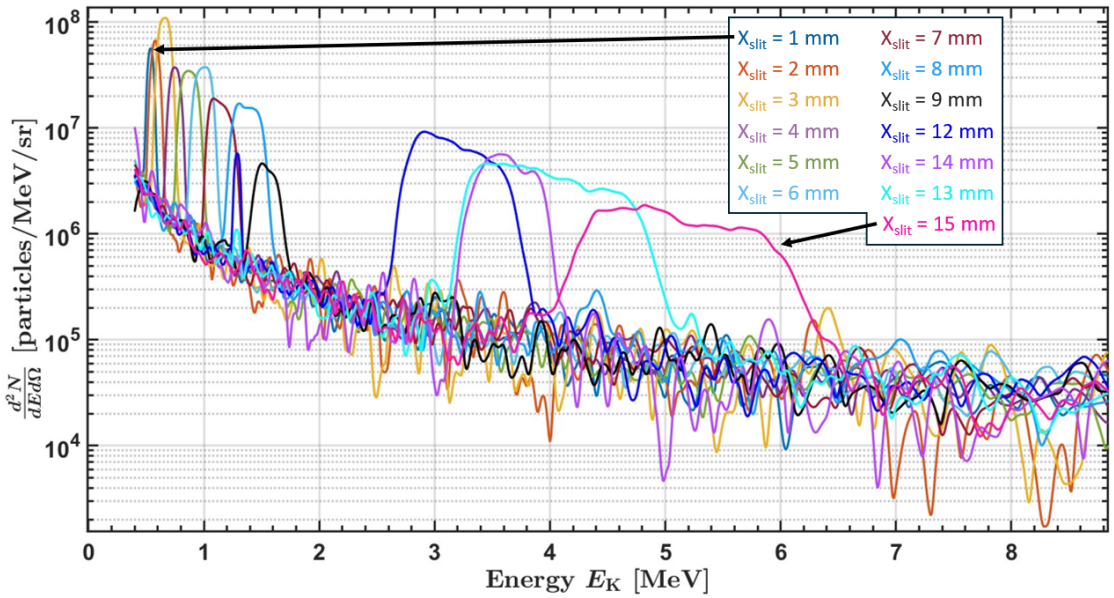

FIGURE 6.25 Spectre de protons après la mise en place du sélecteur d'énergie. Les différentes courbes correspondent à différentes positions de la fente en tantalum (Ta) et les spectres ont été moyennés sur 10 tirs chacun. Les plateaux correspondent à une position croissante de la fente de gauche à droite, comme indiqué par les deux flèches.

Les résultats montrés dans les figures Figure 6.23, Figure 6.24 et Figure 6.25 démontrent que les observations faites par Chen et al. [78] peuvent être reproduites en utilisant la ligne de faisceau à ALLS, soulignant la polyvalence de la méthode proposée. Il s'agit d'un résultat crucial, car les deux montages expérimentaux diffèrent dans leurs paramètres clés tels que le matériau de la cible, la durée de l'impulsion laser et le diamètre du point focal. Prouver que le sélecteur d'énergie peut être utilisé efficacement pour contrôler l'énergie des protons permet une analyse couche par couche des échantillons solides. La sélection des énergies centrales fonctionne efficacement, nous permettant d'ajuster finement le faisceau de protons. Cependant, au lieu de la largeur de bande de 10 % observée dans le travail de Chen et al. [78], le montage à ALLS présente une tendance à la hausse plus marquée pour des énergies centrales plus élevées, avec une valeur globalement augmentée, comme le montre la Table 6.1. À 0.99 MeV, les mesures à ALLS montrent une largeur de bande de 34.7 %, tandis qu'à 5.07 MeV, elle atteint 47.2 %. Cela diminue la capacité à sonder avec précision des couches minces en profondeur dans le matériau. Dans les cas où plusieurs couches minces recouvrent le matériau de base, cela ne devrait cependant pas trop limiter les capacités du Particle-Induced X-ray Emission (PIXE) multicouche, car la largeur de bande est minimisée à des énergies centrales plus faibles, qui déposent principalement leur énergie dans les premières couches du matériau. L'augmentation du

pourcentage de la largeur de bande provient de la distance accrue entre le sélecteur et la source dans les différents montages utilisés. Une plus grande distance source–sélecteur permet au faisceau de protons de diverger davantage avant d'entrer dans le sélecteur, déformant ainsi leur trajectoire et entraînant une largeur de bande élargie.

TABLE 6.1 Données de mesure de la largeur de bande des protons pour différentes énergies centrales, illustrées dans la Figure 6.24.

Énergie centrale (MeV)	**Largeur de bande** (%)
0.54 MeV	20.7%
0.99 MeV	34.7%
1.57 MeV	22.3%
2.01 MeV	28.9%
3.19 MeV	28.9%
4.07 MeV	48.1%
5.07 MeV	47.2%

La transmission moyenne globale

$$T = \frac{\text{Rendement en protons avec le sélecteur}}{\text{Rendement en protons sans le sélecteur}}$$

dans la région de largeur de bande correspondante, pour l'ensemble des énergies centrales mesurées, est de $20 \pm 9\%$. Comme prévu, une majorité de protons est perdue au profit de la sélection d'énergies à partir d'un spectre continu, ce qui entraîne un rendement en rayons X plus faible par tir. Cependant, cette limitation peut être compensée en effectuant un plus grand nombre de tirs pour l'acquisition d'un seul spectre de rayons X caractéristiques. Le nombre moyen de protons dans le plateau sélectionné est supérieur d'un à, dans le meilleur des cas, deux ordres de grandeur par rapport au reste du spectre. Cependant, un spectre de fond constant, d'une magnitude moyenne d'environ 1×10^5, est observé pour tous les réglages du sélecteur d'énergie, sur l'ensemble du spectre énergétique. Il a été constaté que ce fond correspond au bruit du système de caméra et qu'il est présent même en l'absence du sélecteur. la Figure 6.26 montre comment la plage d'énergie (du minimum au maximum du plateau observé dans la Figure 6.25) dépend de la position des deux bords de la fente. La position de la fente indique la distance du bord par rapport à la position complètement rétractée du bord correspondant. La tendance observée est similaire à celle de la Figure 6.24 : pour des positions de fente plus élevées, et donc des énergies centrales plus importantes, la séparation spatiale entre les protons de différentes énergies diminue, ce qui élargit la plage d'énergie pour une distance de déplacement identique. Une fois qu'un bord s'approche du centre de l'axe initial du faisceau de protons, la largeur du spectre augmente de façon significative. Les deux jeux

de données présentés dans la figure montrent une légère différence, due aux positions initiales différentes des bords supérieur et inférieur de la fente. Ces résultats confirment à nouveau les observations et simulations rapportées par Chen et al. [78].

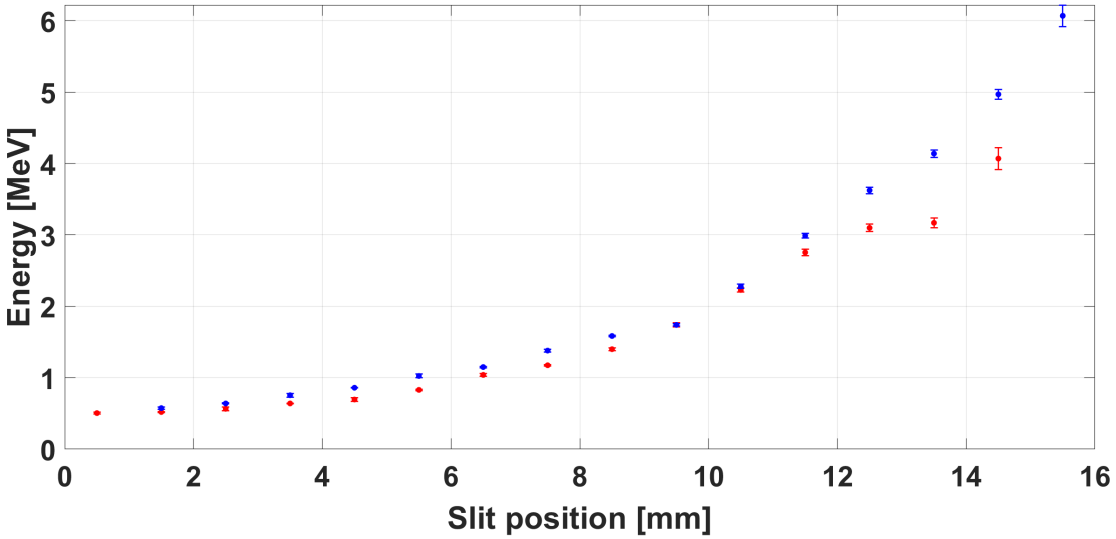

FIGURE 6.26 Énergie des protons pour différentes positions des deux bords de fente individuels. Les bords ont été déplacés simultanément, avec une distance fixe de 1 mm entre eux.

Expériences futures

Les mesures d'étalonnage présentées sont particulièrement précieuses, car les données de la Figure 6.26 permettent de calculer la plage d'énergie attendue ΔE pour diverses ouvertures et positions de fente, et inversement. Le calcul dépend uniquement de la position spécifique de chaque bord, comme décrit dans la Equation 6.28, où E_{lower} et E_{upper} sont les énergies correspondant aux positions des bords supérieur et inférieur respectivement :

$$\Delta E = E_{\text{lower}} - E_{\text{upper}} \tag{6.28}$$

Trois échantillons différents sont proposés pour des expériences futures, comme illustré dans le schéma de la Figure 6.27. Les échantillons à deux et trois couches sont similaires à ceux utilisés dans les travaux de Puyuelo-Valdés et al. (2021) [1], qui seront discutés plus en détail dans la section suivante.

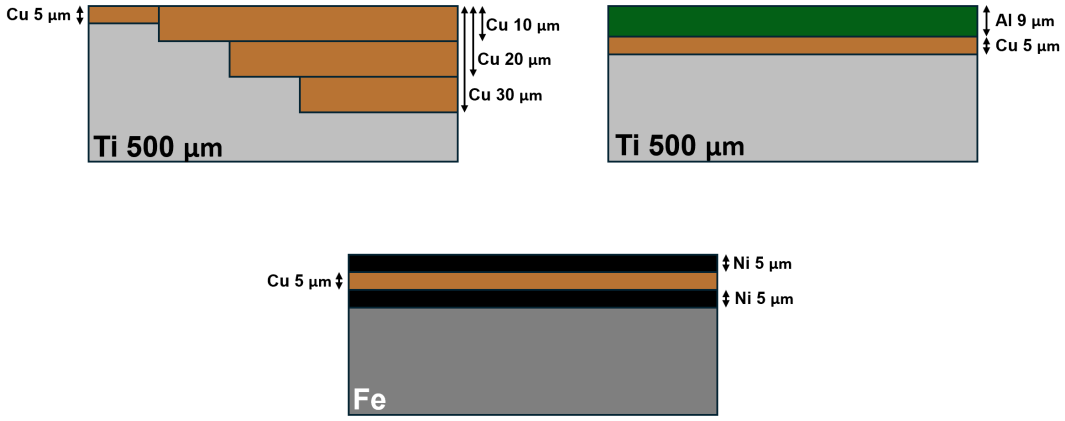

FIGURE 6.27 Schéma de trois échantillons proposés pour de futures expériences multicouches. Haut gauche : différentes épaisseurs de copper (Cu) sur un substrat de titanium (Ti) de 500 µm. Haut droite : structure à trois couches composée d'aluminum (Al), Cu et un substrat de Ti de 500 µm. Bas : échantillon à quatre couches composé de 5 µm de nickel (Ni), 5 µm de copper, 5 µm de Ni, suivi d'un substrat de iron (Fe).

En utilisant les données recueillies lors des mesures de la **??**, on peut calculer les positions de fente nécessaires pour sonder chaque couche. Les résultats sont présentés pour l'échantillon à quatre couches dans la Table 6.2.

TABLE 6.2 Positions de fente proposées, basées sur le dépôt d'énergie des protons, pour une analyse multicouche d'un échantillon à quatre couches : 5 µm de Ni, 5 µm de Cu, 5 µm de Ni, et un substrat de Fe.

Couche	**Énergie (Bragg)** (MeV)	**Bord sup.** (mm)	**Bord inf.** (mm)	**Largeur fente** (mm)
5 µm Ni	0.86	1.0	3.8	2.8
5 µm Cu	2.05	6.0	10.0	4.0
5 µm Ni	3.18	10.2	11.6	1.4
Substrat Fe	$\geq$ 3.9	13.8	15.5	1.7

Avec les réglages du sélecteur d'énergie proposés, basés sur les données de calibration, la procédure globale de l'analyse multicouche pourra être vérifiée. La cible d'interaction laser utilisée sera une feuille de tantalum d'une épaisseur de 2 µm. Bien que l'échantillon ne soit pas soumis à une X-Ray Fluorescence (XRF) — les rayons X produits par le mécanisme Target Normal Sheath Acceleration (TNSA) étant bloqués par le sélecteur — il est important de noter que la combinaison de 5 µm de nickel et de 5 µm de copper atténue respectivement 98.28 % et 98.69 % des rayons X caractéristiques du iron. On peut donc raisonnablement supposer qu'aucun rayon X caractéristique provenant du substrat n'atteindra le détecteur, même après plusieurs tirs. De même, seulement 4.1% des rayons X caractéristiques de la deuxième couche de nickel atteindront le détecteur. Une

fluorescence secondaire reste cependant possible entre les rayons X K_α et K_β du copper et la couche supérieure de nickel. Ce résultat souligne à nouveau à quel point l'ordre des couches et la nature des éléments sont cruciaux pour une analyse XPIF réussie, car un agencement sous-optimal peut sévèrement limiter les capacités de la technique. Ces prédictions devront être validées expérimentalement lors de prochaines campagnes de mesure, afin de mieux cerner les limites de cette procédure multicouche.

Vérification des calculs de rendement multicouche

Au moment de la rédaction, les données expérimentales des échantillons multicouches testés avec le sélecteur d'énergie n'étaient pas encore disponibles. Bien que ces expériences aient été initialement prévues, des contraintes de calendrier à l'installation laser ont empêché leur réalisation. Des expériences sur des échantillons multicouches sont cependant prévues dans un futur proche, en utilisant les échantillons montrés dans la Figure 6.27. À la place, on tente d'évaluer les performances du code, y compris les calculs pour les échantillons multicouches, en se basant sur une ancienne mesure effectuée dans le même laboratoire en 2021. Dans les travaux de Puyuelo-Valdes et al. [1], un échantillon massif composé de titanium pur a été recouvert de couches de copper d'épaisseurs variables (5, 10 et 20 µm, montré schématiquement dans la Figure 6.27) et a été irradié en utilisant la méthode XPIF. Le matériau cible utilisé pour l'accélération laser était le copper, qui est actuellement le seul élément entièrement implémenté dans le code. Pour des cibles avec des numéros atomiques plus élevés comme l'gold (Au) ou le tantalum, le Bremsstrahlung et les raies caractéristiques $L_{\alpha,\beta}$ doivent être inclus dans les calculs. Bien que les premiers calculs pour le Bremsstrahlung soient déjà terminés, ils doivent être vérifiés en même temps que les intensités $L_{\alpha,\beta}$. Bien que le code *MATLAB* présenté au chapitre précédent soit prêt à être déployé, la vérification de ses calculs reste difficile en raison du manque de données. Pour la vérification du code, la quantité de titanium sous les différentes couches de copper, irradiée par un spectre de protons continu, est estimée. Idéalement, les calculs donneront un substrat de titanium pur à $\sim$ 100%, puisque le rendement des pics de copper détectés sera pris en compte par les calculs de la couche supérieure. Les mesures effectuées par Puyuelo-Valdes et al. [1] sont montrées dans la Figure 6.28. On peut voir qu'avec une épaisseur croissante de la couche de copper, la taille de la raie K_α du titanium diminue. Ce comportement est conforme aux attentes, puisqu'une couche de copper plus épaisse entraîne l'absorption et le blocage de plus de rayons X et de protons.

TABLE 6.3 Transmission des rayons X caractéristiques K_α de copper et titanium à travers des couches de copper de diverses épaisseurs, parcours projeté des protons, et nombre de protons qui ne s'échappent pas de la couche supérieure (nombre total de protons avant dépôt d'énergie : 6.6×10^{10}).

	5 µm	10 µm	20 µm
Trans. Cu K_α	77.6%	60.8%	36.3%
Trans. Ti K_α	29.1%	9.1%	0.7%
Énergie de coupure des protons	0.783 MeV	1.302 MeV	2.089 MeV
Nombre de protons sous E_c	2.1×10^{10}	4.0×10^{10}	5.4×10^{10}
(en %)	(31.8%)	(60.6%)	(81.1%)

la Figure 6.29 montre la diminution du nombre de protons due au dépôt d'énergie dans la couche supérieure, et la Table 6.3 indique à quel point les différents types de rayons X sont atténués en traversant l'échantillon. Cela est particulièrement important pour le rayonnement caractéristique ($K_{\alpha,\beta}$) du titanium, qui est beaucoup plus atténué car ces photons sont moins énergétiques que les rayons X K_α du copper. À une épaisseur de 20 µm, presque aucun rayon X n'est capable de traverser la couche de copper. L'énergie de coupure (également appelée parcours projeté) indiquée dans le tableau correspond à l'énergie minimale qu'un proton doit avoir pour traverser la couche supérieure. En dessous de cette énergie, toute l'énergie est déposée dans la couche et contribue à la génération d'un rendement via PIXE. Dans la routine *MATLAB*, cette énergie de coupure est utilisée pour différencier l'utilisation du formalisme PIXE pour couche mince ou épaisse, comme décrit dans la section 6.2.

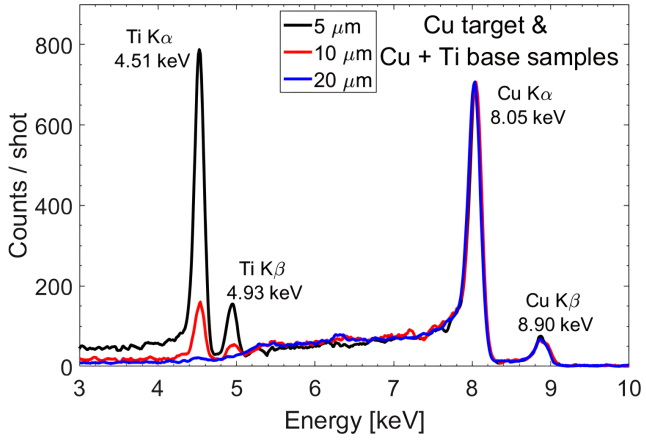

FIGURE 6.28 Mesure Ti-Cu effectuée par Puyuelo-Valdes et al. en 2021 [1], pour une couche de copper de 5, 10 et 20 µm sur un substrat de titanium (en utilisant la cible d'interaction de copper avec le spectre de protons montré dans la Figure 6.31). Pour les calculs, les données ont été extraites avec l'add-on *GRABIT* fourni pour *MATLAB*.

Les calculs concordent avec l'observation de la Figure 6.28, où aucune raie K_α du titanium n'est visible pour la mesure avec une couche de 20 µm. Même si certains protons atteignent le substrat de titanium, les rayons X caractéristiques excités ne sont pas assez énergétiques pour traverser la couche supérieure en direction du détecteur. Cette limitation est un facteur crucial dans le traitement d'échantillons multicouches, car elle limite la profondeur de détection de la méthode XPIF, même si elle est alimentée par des protons et rayons X TNSA d'énergies suffisamment élevées. Si la combinaison de composition élémentaire et d'épaisseur de la couche supérieure est défavorable, les rayons X ne seront pas détectés. Une observation tirée de la Figure 6.28, qui ne correspond pas aux attentes, est la hauteur et l'aire constantes de la raie K_α du Cu. On s'attendrait plutôt à une augmentation avec l'épaisseur croissante de la couche, car plus de rayons X et de protons devraient y déposer leur énergie. Cette découverte n'est pas discutée en détail dans le travail de Puyuelo-Valdes et al. [1], et a été initialement interprétée comme étant due à la diffraction élastique des rayons X copper entrants générés par TNSA. Cette hypothèse a conduit à l'implémentation des calculs de diffraction décrits dans la section 6.2 dans le code *MATLAB*. Les résultats sont présentés avec les impacts des calculs multicouches dans les paragraphes suivants.

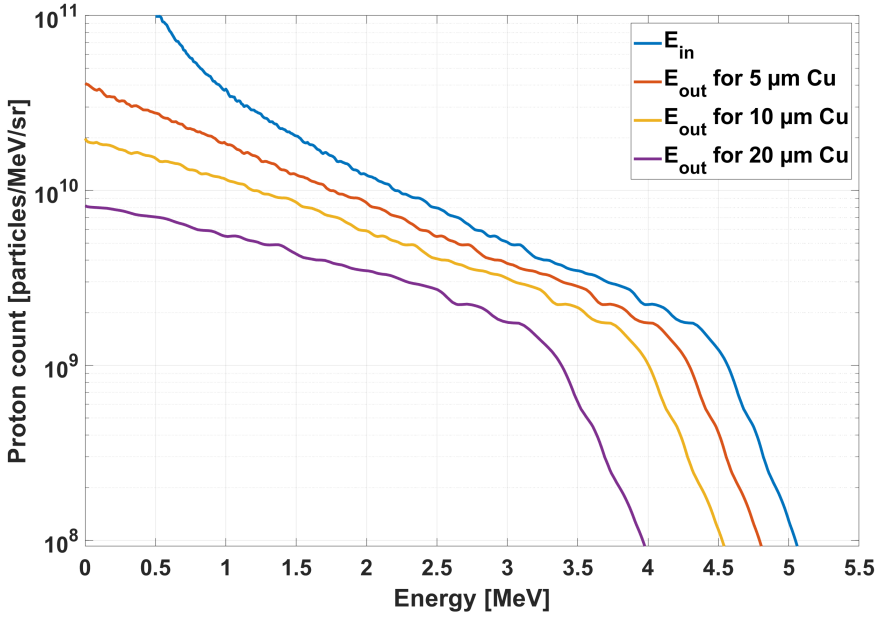

FIGURE 6.29 Spectre de protons après différentes épaisseurs de copper (5, 10 et 20 µm). Les calculs sont effectués en utilisant les équations présentées dans la section 6.2.

L'échantillon original a une épaisseur de 500 µm et une surface de 2×2 cm^2. Ci-dessous, les résultats de trois versions différentes du code *MATLAB*, décrites ci-après, sont comparés pour les mesures de 5 µm et 10 µm. La mesure avec une couche de copper de 20 µm ne présente aucune raie $K_\alpha$du Ti identifiable et est donc exclue de l'analyse. La pre-

mière version du code, nommée "initial", représente la structure initiale avant ce travail, sans calculs de rendement supplémentaires pour les échantillons multicouches. La seconde version ("initial + top layer") implémente uniquement les calculs de rendement dans différentes couches ainsi que l'atténuation des rayons X et protons, comme décrit dans la section 6.3. La dernière version, "current", inclut en plus la prise en compte de la diffraction élastique de l'échantillon vers le détecteur. Dans les simulations effectuées, la comparaison du rendement théorique au rendement expérimental est toujours un ajustement parfait. Aucun post-traitement n'a été appliqué aux données extraites, car cela avait déjà été fait pour les données présentées par Puyuelo-Valdes et al. [1]. La somme des concentrations massiques a été limitée à une plage de 0.8 à 1, et l'aire des pics a été calculée à l'aide d'une méthode différentielle.

TABLE 6.4 Résultat pour les concentrations massiques (équivalentes au pourcentage de cet élément dans l'échantillon) du spectre montré dans la Figure 6.28, tel que calculé par différentes versions du code. La restriction $0.8 \leq \sum_i w_i \leq 1$ a été appliquée à la simulation.

Version du code	Couche de Cu de 5 µm	Couche de Cu de 10 µm
initial	w_{Cu} : 0.830 w_{Ti} : 0.052	0.864 0.012
initial + top layer	w_{Cu} : 0.775 w_{Ti} : 0.116	0.812 0.075
current	w_{Cu} : 0.630 w_{Ti} : 0.264	0.684 0.214

Les résultats, présentés dans la Table 6.4, montrent une augmentation de la quantité estimée de titanium à l'intérieur de l'échantillon lors de l'implémentation de plus de calculs dans la routine multicouche. Alors que l'estimation du code « initial » ne suppose que quelques pourcents de titanium, la version « current » calcule des quantités $> 20\%$. Cependant, comme un substrat de titanium est étudié, ces valeurs sont loin des résultats visés. En raison de l'indisponibilité des données brutes des travaux de Puyuelo-Valdes et al. [1], et des conditions expérimentales exactes, seules des hypothèses sur les lacunes des calculs et les raisons potentielles de la faible estimation de titanium dans l'échantillon peuvent être faites. Les rayons X copper entrants, produits par TNSA, n'ont pas une énergie suffisante pour exciter les rayons X caractéristiques dans la couche de copper présentée. Par conséquent, il ne peut y avoir de contribution XRF résultant de cette couche, et la totalité du rendement de copper doit être produite par PIXE. Suite à ce fait, on s'attendrait à ce qu'avec une épaisseur de couche croissante, le nombre de coups $K_{\alpha,\beta}$ de copper augmente, et en même temps que le nombre total de coups $K_{\alpha,\beta}$ de titanium diminue. Cependant, alors que les pics de titanium suivent le comportement attendu en raison de l'atténuation accrue des rayons X et des protons, le pic de copper ne suit pas la tendance inverse. Dans les données présentées (Figure 6.28), un pic de copper

de hauteur et d'aire constantes est observé pour des épaisseurs de couche allant jusqu'à 20 µm. Cette observation suggère qu'une autre interaction physique a lieu à l'intérieur de l'échantillon. Cela a conduit à l'hypothèse que la diffraction élastique en était la cause, ce qui a été ensuite implémenté dans les calculs de rendement. Bien que l'inclusion de la diffraction ait amélioré l'estimation de la quantité de titanium de manière significative ($\sim 15\%$), cela n'est pas suffisant pour expliquer les résultats observés dans la Figure 6.28. Sinon, les calculs estimeraient une concentration de titanium proche de 100% à l'intérieur de l'échantillon. Comme mentionné au chapitre précédent, les mêmes échantillons seront à nouveau irradiés lors de futures expériences pour confirmer ces découvertes, trouver la cause du phénomène présenté et affiner le code. En utilisant les équations introduites dans la section 6.2, la contribution de la diffraction élastique par les couches de copper de 5 µm et 10 µm s'élève à 67.3% et 71.2%, respectivement. Le reste des rayons X de Cu mesurés est supposé être généré par PIXE, puisque la XRF ne se produit pas à l'intérieur de la couche de copper. Dans le cas de la couche de copper de 5 µm d'épaisseur, le rendement PIXE calculé représente 6.9% du rendement total (XRF + PIXE), soit seulement 2.2% de l'aire totale (rendement + diffraction) sous le pic K_α du Cu. Comme indiqué précédemment, il n'y a pas de contribution de la XRF puisque les rayons X générés par TNSA ne peuvent pas exciter les rayons X caractéristiques dans le copper. Dans le cas de la mesure de 10 µm, les valeurs augmentent à 28.8% et 8.3%. Cela montre que les calculs effectués dans la couche supérieure semblent corrects à première vue, car avec une épaisseur croissante, le rendement augmente également. Cependant, les calculs ne parviennent pas à expliquer la taille de la raie K_α du copper. Par conséquent, le code doit supposer que le rendement restant provient du substrat (Ti) de l'échantillon (montré dans la Figure 6.30), car aucune autre source potentielle de rendement en rayons X ne lui est fournie. Cela entraîne une surestimation du cuivre à l'intérieur du substrat de titanium.

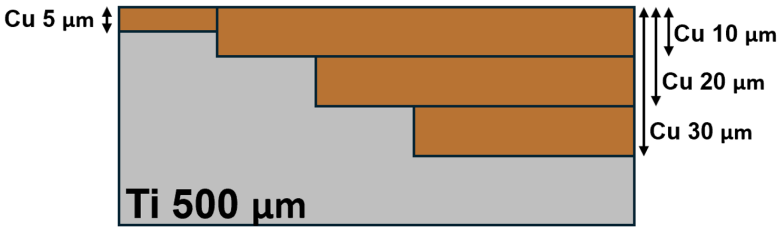

FIGURE 6.30 Schéma de l'échantillon Cu-Ti utilisé pour la validation du code.

En raison des observations faites lors de la mesure, il est probable qu'un autre facteur influence les données de mesure. Dans la même référence, une expérience similaire a été menée en utilisant de l'gold comme cible d'interaction laser, montrée dans la Figure 6.31. L'échantillon était composé d'une structure à trois couches faite d'aluminum, d'copper et d'un substrat de titanium. La partie gauche de la Figure 6.31 montre le spectre de protons pour une cible TNSA d'gold, comme montré dans la Figure 6.27.

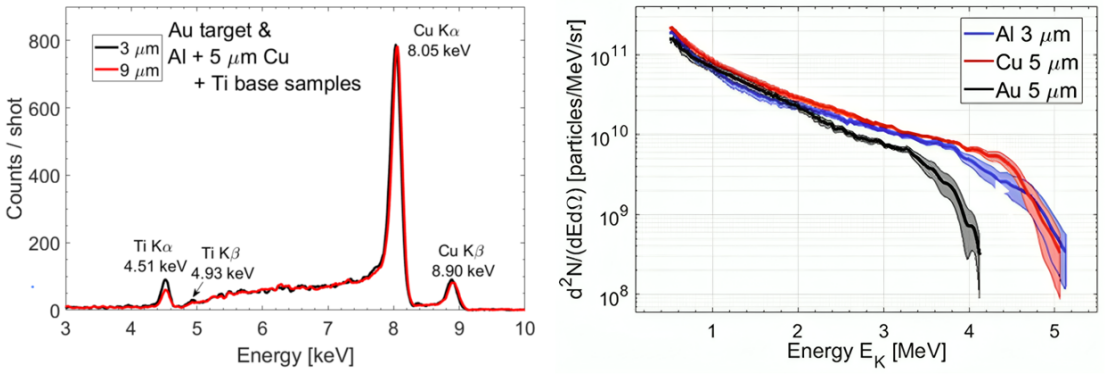

FIGURE 6.31 À gauche, spectres de couches d'Al de 3 et 9 µm reposant sur une couche de Cu de 5 µm placée sur un substrat de Ti, irradiées par XPIF en utilisant une cible d'Au de 5 µm. À droite, les spectres d'énergie des protons accélérés par des cibles d'Al de 3 µm (bleu), de Cu de 5 µm (rouge) et d'Au de 5 µm (noir) d'épaisseur, mesurés par le spectromètre TP. Les données ont été extraites de [1].

L'utilisation d'une cible d'interaction en gold n'est pas encore prise en charge dans la routine *MATLAB*, et par conséquent, aucune conclusion concernant l'analyse quantitative ne peut être tirée. De plus, comme l'aluminum et l'gold se situent tous deux en dehors de la plage du détecteur, il n'est pas possible d'analyser la teneur en aluminum ou la diffraction élastique potentielle des rayons X de l'gold par la couche supérieure. Néanmoins, un pic de copper constant peut à nouveau être observé sur plusieurs mesures, ce qui dans ce cas ne peut pas être causé par la diffraction élastique. Même en considérant les facteurs suivants, le rendement observé ne peut pas être expliqué de manière adéquate :

- Le pouvoir d'arrêt légèrement plus élevé de l'aluminum (1.720×10^2 MeV cm^2/g) contre 1.182×10^2 MeV cm^2/g pour l'gold à 1 MeV [26], combiné à l'énergie maximale plus faible du spectre de protons, fait que le PIXE est plus important que la XRF dans la couche de copper.

- Puisque les rayons X caractéristiques de l'gold ($K_\alpha = 68.803$ keV, $K_\beta = 77.984$ keV [107]) sont suffisamment énergétiques, la XRF est possible. Cependant, 9 µm d'aluminum transmet $\sim 99.95\%$ des rayons X entrants tandis que la couche de copper transmet 99.65%. Par conséquent, on peut en conclure que la majeure partie de la XRF se produit à l'intérieur du substrat de titanium, et que le rayonnement caractéristique du Ti est fortement atténué sur le chemin vers le détecteur, tout en causant potentiellement une fluorescence secondaire dans la couche d'aluminum. Par conséquent, la XRF ne peut pas être la cause de la taille des pics de copper.

Ainsi, il est probable que le rendement élevé observé aux énergies K_α et K_β du copper provienne d'une source non prise en compte. La fluorescence X parasite provenant des composants de l'instrument, par exemple, pourrait contribuer à ce signal. La dernière

possibilité est une erreur dans les calculs du rendement en rayons X. Cependant, l'identification de l'origine précise des comptes non pris en compte n'est pas possible sans données expérimentales supplémentaires pour l'enquête. Les travaux futurs se concentreront sur la validation rigoureuse du code à l'aide d'une série d'expériences sur des échantillons bien caractérisés. Bien que de telles expériences aient dépassé le cadre de ce travail en raison de contraintes externes, un plan expérimental complet a été établi. Ce plan implique l'irradiation d'échantillons métalliques multicouches, sélectionnés pour leurs émissions de rayons X caractéristiques dans les limites détectables de la caméra à rayons X. Les échantillons, montrés dans la Figure 6.27, présentant diverses combinaisons et épaisseurs de couches, seront analysés sous irradiation d'un spectre de protons complet ainsi que d'énergies de protons discrètes et sélectionnées via le sélecteur présenté. Cette approche systématique générera un ensemble de données robuste, essentiel pour vérifier la précision des calculs du code et identifier d'éventuelles erreurs systémiques.

Détection d'aérosols dans l'air

Le deuxième objectif de ce travail est d'évaluer la faisabilité de la détection d'aérosols dans l'air au moyen de la méthode XPIF décrite dans la section 6.3. Le gaz choisi pour les expériences était le krypton (Kr), car il se situe près du milieu de la plage d'énergie détectable de la caméra à rayons X et était facile à mettre en œuvre dans le montage existant. La détection de krypton (Kr) dans l'air a été effectuée à trois niveaux de dilution différents : 4 %, 0.4 %, et 0.04 %. La dilution de krypton a été réalisée en utilisant la méthode décrite dans la section 6.3. Les spectres mesurés pour chaque dilution sont montrés dans la Figure 6.32. Pour obtenir un Signal to Noise Ratio (SNR) suffisant, plusieurs tirs ont été nécessaires : 60 tirs pour 4 %, 100 tirs pour 0.4 %, et 120 tirs pour 0.04 %. Ensuite, toutes les données ont été moyennées sur 30 tirs pour une meilleure comparabilité. L'ajustement par régression linéaire pour l'étalonnage de la caméra CCD donne : 0.00746 ($\pm$ 0.00014) $\cdot$ x keV - 1.571 ($\pm$ 0.152) keV.
Dans les trois cas, les pics $K_\alpha = 12.649\,\text{keV}$ et $K_\beta = 14.112\,\text{keV}$ [90] du krypton sont identifiables sans nécessité de post-traitement. Cependant, pour la plus faible dilution, il n'est pas possible de vérifier de manière fiable le pourcentage de krypton dans le mélange gazeux sur la base des données mesurées. Bien que pour ce pourcentage de gaz, le pic satisfasse au critère Minimal Detectable Limit (MDL) introduit plus tôt dans ce travail, les résultats de l'analyse fournissent des informations peu fiables, qui seront discutées dans cette section. Il est également à noter que la raie K_β) à 0.04 % n'est plus distinguable du bruit de fond. L'analyse des pics se fait en examinant la hauteur et l'aire des raies K_α) les unes par rapport aux autres. Avant d'étudier les caractéristiques des pics, le pic enregistré a été comparé à toutes les raies K_α) des éléments présents dans le montage, confirmant que le signal enregistré est bien attribué au krypton. La superposition des différentes mesures appuie en outre cette affirmation. Outre le pic de krypton, de nombreux autres

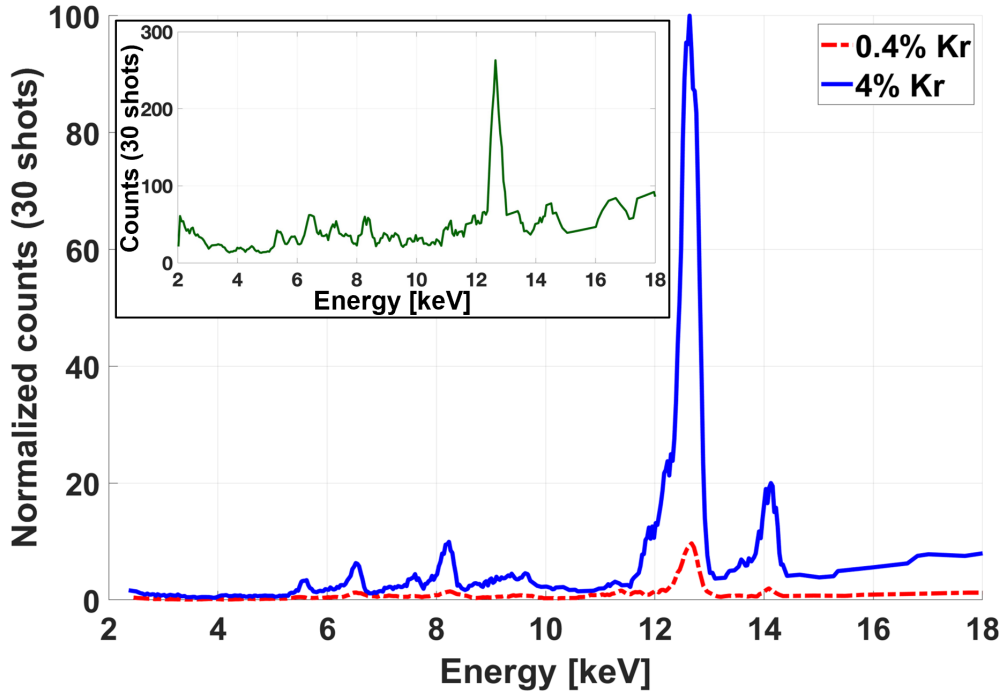

FIGURE 6.32 Spectres de rayons X générés pour les trois proportions mesurées de krypton dans l'air ; Rouge : 0.4 %, et Bleu : 4 %. L'encart montre une mesure où la dilution visée était de 0.04 %.

pics (notamment à 5.62, 6.52, 7.61, 8.23, 9.63, et 11.27 keV) sont visibles dans le spectre. Les raies K_α) trouvées dans le spectre à des énergies inférieures à la raie nominale K_α) du krypton (12.65 keV) peuvent s'expliquer comme suit :

Les rayons X du Kr générés interagissent avec les autres atomes typiquement contenus dans l'air — principalement N_2 (78 %), O_2 (21 %), Ar (1 %), et CO_2 (0.04 %) [82] — et perdent une partie de leur énergie durant ce processus. À titre d'exemple, le deuxième plus grand pic à 8.23 keV peut s'expliquer par l'excitation des rayons X suivants par un rayon K_α) produit à l'intérieur de la chambre [90] : deux raies $O_{K_\alpha} = 524.9$ eV, une raie $Ar_{K_\alpha} = 2.96$ keV, et une raie $N_{K_\alpha} = 292.4$ eV, entraînant une perte d'énergie totale de 4.40 keV. Le même raisonnement s'applique au reste des pics non identifiés aux énergies susmentionnées. On s'attend à ce que les rayons X générés par la fluorescence du krypton soient la cause des pics supplémentaires, car la section efficace des rayons X issus du rayonnement généré par le Ta est inférieure d'au moins deux ordres de grandeur à celle du Kr pour tous les éléments pertinents [107]. Cette affirmation est en outre soutenue par la diminution constante de l'intensité de tous les pics lorsque le niveau de dilution du krypton est diminué. Selon la base de données du NIST [26], le krypton présente un pouvoir d'arrêt des protons légèrement inférieur à celui de l'air sec dans la gamme de 0−6 MeV. Cela suggère que les protons peuvent induire un rendement en rayons X marginalement plus élevé lié aux composants de l'air en raison d'un dépôt d'énergie

accru. Cependant, les pics K_α) des constituants de l'air ne sont pas détectables avec le montage actuel, ce qui rend impossible la détermination du pourcentage de krypton sur la base de la mesure d'un seul niveau de dilution. En revanche, les rayons X du tantalum produits par TNSA ($K_{\alpha,\mathrm{Ta}} = 57.53\,\mathrm{keV}$) interagissent avec le krypton avec des sections efficaces de deux à quatre ordres de grandeur plus élevées qu'avec tous les composants de l'air énumérés précédemment. On peut en conclure que la XRF apporte en effet une contribution précieuse à la technique XPIF. Particulièrement dans le cas du krypton, la XRF peut aider à mieux distinguer les raies du Kr du bruit de fond. En utilisant le spectre de protons TNSA du tantalum, comme décrit dans la section 6.3, la contribution de la XRF pour les rayons X caractéristiques et le Bremsstrahlung peut être calculée et comparée à la contribution des protons. En utilisant la quantité de rayonnement/protons qui frappent l'échantillon et les sections efficaces d'interaction respectives, le rendement qui est généré par atome en $\frac{\mathrm{atome}}{\mathrm{cm}^2}$ est calculé. Les calculs montrent que le PIXE contribue à $\sim$ 85 % du signal global, la partie caractéristique de la XRF assurant le reste. Le Bremsstrahlung est de deux à trois ordres de grandeur plus faible par rapport aux rayons X caractéristiques ($K_{\alpha,\beta}$) de la cible d'interaction laser (Cu) et est donc considéré comme négligeable. Bien que la base de données des sections efficaces XRF ne contienne que des valeurs allant jusqu'à 200 keV, on ne s'attend pas à ce que la contribution change de manière significative, car les valeurs des sections efficaces diminuent avec l'augmentation de l'énergie incidente des photons [107]. Pour vérifier la quantité de molécules de krypton dans le mélange gazeux, deux méthodes couramment utilisées pour l'analyse des spectres XRF sont employées : l'aire du pic et la hauteur du pic [108]. Les résultats de l'analyse des aérosols par XPIF sont consignés dans le Table 6.5. L'aire sous un pic est estimée à l'aide d'un ajustement gaussien comme décrit dans la section 6.3. Pour quantifier si un pic peut être reconnu comme tel, la méthode MDL décrite dans la même section est utilisée. En comparant les aires des pics de krypton dans l'air (montrées dans le Table 6.5), la dilution à 0.4 % correspond à 8.6 % de l'aire du pic de référence à une dilution de 4 % de krypton. La hauteur du pic est de même réduite à 9.7 %. Bien que cela n'équivaille pas à la diminution attendue de 10 %, en corrélation avec la dilution de krypton, les deux valeurs se situent dans la plage d'erreur attendue, étant donné la fluctuation tir-à-tir d'environ 18 % du rendement en protons.

TABLE 6.5 Résumé des caractéristiques du pic K_α) pour différentes proportions de krypton dans l'air, montrées dans la Figure 6.32. La hauteur et l'aire du pic pour la dilution de 0.04 % de Kr sont extrapolées à partir des deux autres mesures. Les valeurs pour $Y_{\text{background}}$ et Y_{MDL} sont des estimations basées sur le bruit des mesures effectuées avec une dilution plus faible.

Proportion de Kr	Hauteur du pic [coups]	Y_{MDL} [coups·keV]	Y_{peak} [coups·keV]	$Y_{\text{background}}$ [coups·keV]
4 %	3912	21	1188	49
0.4 %	378	8	102	8
0.04 % (estimé)	~ 39	7	$\sim 10-12$	5

Dans le cas de la mesure à 0.04 % de Kr, la hauteur et l'aire ont indiqué une teneur en krypton plus élevée que prévu. Cet écart est probablement dû aux limitations du manomètre de mesure ou à la méthode utilisée pour introduire le krypton dans la chambre. À de faibles dilutions, l'adsorption de krypton sur les parois de la chambre pendant l'évacuation et la désorption subséquente lors de la remise à l'air peuvent contaminer le mélange et fausser la concentration visée. Bien que négligeable à 4 % et 0.4 %, cet effet devient significatif à des niveaux de dilution plus faibles. Au lieu de cela, les mesures à des dilutions inférieures à 0.4 % ont été utilisées pour affiner l'estimation du SNR à de faibles concentrations. Le Table 6.5 présente les valeurs de SNR correspondantes et les limites de détection théoriques du montage. Compte tenu des résultats présentés, on estime que 0.4 % représente actuellement la plus faible dilution permettant des mesures fiables avec le montage actuel. Bien que des concentrations aussi faibles que 0.04 % soient très probablement détectables aussi, les mesures sont limitées par le matériel et la méthodologie du mélange de gaz. À des dilutions inférieures à ~ 0.04 %, on s'attend à une baisse du SNR, ce qui rend l'analyse plus difficile. Cependant, effectuer plus de tirs laser à des dilutions plus faibles pourrait atténuer cette limitation. Par conséquent, on prévoit que le montage sera capable de mesurer avec confiance des dilutions jusqu'à 0.01 % avec la configuration expérimentale actuelle.

6.5 Résumé et perspectives

Ce chapitre résume les résultats obtenus dans le cadre de cette thèse et présente une perspective sur les recherches futures. Il aborde les expériences potentielles et les modifications possibles du matériel et du logiciel du montage expérimental, et se termine par un aperçu de l'avenir de la technique X-ray and Particle Induced X-ray Fluorescence (XPIF).

Analyse couche par couche par XPIF

Ce travail présente l'utilisation de XPIF pour des échantillons à plusieurs couches, en décrivant la théorie ainsi que les capacités et les limites du montage expérimental. La méthode repose sur deux éléments clés : un sélecteur d'énergie matériel et une procédure MATLAB personnalisée. Il est démontré que le sélecteur d'énergie de Chen et al. [78], installé à l'installation ALLS, permet de contrôler le spectre énergétique des protons, offrant un contrôle de la profondeur pour une analyse couche par couche. Bien que les tests confirment qu'il peut générer des plateaux d'énergie adéquats, sa précision est limitée à des énergies plus élevées en raison de l'élargissement de la bande passante. Ce problème est dû à la distance entre le sélecteur et la source, une contrainte physique à l'intérieur de la chambre principale. À partir de ces résultats, les positions des fentes pour diverses énergies et bandes passantes ont été calculées pour de futures expériences. Le code MATLAB original de Frédéric Boivin [2] a été étendu pour analyser des échantillons composés de plusieurs couches de compositions élémentaires différentes. Les principales modifications concernent les calculs de rendement, l'atténuation par les couches sus-jacentes et la diffraction des rayons X, ainsi que la mise en œuvre de tables de consultation pour une couverture élémentaire plus large. Les premiers tests montrent que la routine et les calculs sont correctement implémentés. Cependant, la validation de la précision de ces calculs reste un défi en raison du peu de données disponibles. Les calculs de rendement n'ont pas pu expliquer complètement les données de mesure de Puyuelo-Valdes et al. [1]. Des tests supplémentaires sont nécessaires pour déterminer la cause de l'écart par rapport aux résultats attendus. Par conséquent, une nouvelle série d'expériences est prévue prochainement. Elle consistera à utiliser XPIF sur plusieurs échantillons métalliques multicouches, présentés dans l' Figure 6.27. Cela aidera à identifier la source des erreurs d'identification élémentaire précédentes et fournira plus de données pour tester le code *MATLAB*. Surtout, la connaissance complète des paramètres expérimentaux permettra une validation plus efficace et précise du code. Les échantillons seront irradiés avec et sans le sélecteur d'énergie pour valider à la fois le code *MATLAB* et la fonctionnalité du sélecteur. Ce sera la première expérience combinant le sélecteur et un échantillon. Si le temps le permet, des maquettes du patrimoine culturel seront également testées pour améliorer la méthode couche par couche et déterminer la profondeur de sondage de la technique XPIF. L'objectif principal est l'identification qualitative et la localisation des

particules dans les échantillons. À l'issue des expériences, il sera possible de développer une technique novatrice capable d'analyser des échantillons multicouches de composition inconnue. La précision et la profondeur de pénétration de la méthode dépendent de l'échantillon, avec des applications potentielles en science des matériaux [109, 110], dans l'industrie des semi-conducteurs [111], le patrimoine culturel [10, 112] et les domaines biomédical et environnemental [113, 114]. Plusieurs extensions matériel et logiciel sont également prévues. Les efforts actuels de l'équipe ALLS se concentrent sur [115, 116] :

- Le remplacement du filtre en beryllium de la caméra à rayons X pour détecter les éléments de numéro atomique plus faible et l'ajout d'un second détecteur pour élargir la couverture du spectre des rayons X et améliorer le rapport signal/bruit.
- L'équipement du sélecteur d'énergie d'un meilleur moteur pour un contrôle plus précis de la position des fentes.
- La mise en œuvre de l'apprentissage automatique pour optimiser les paramètres du laser.
- Cela améliore l'énergie de coupure tout en réduisant le temps nécessaire pour trouver le meilleur jeu de paramètres.
- L'extension du porte-cibles multiple pour les cibles minces d'interaction laser afin d'augmenter le nombre de tirs par cycle de pompage.
- L'extension du code MATLAB avec les calculs de la fluorescence secondaire ainsi que du rendement en rayons X provenant du Bremsstrahlung de la cible TNSA.
- De plus, le code pourra gérer un plus grand nombre de cibles d'interaction laser de matériaux différents.

Des travaux supplémentaires se concentrent sur l'amélioration des fluctuations tir à tir du rendement en protons et en rayons X pour augmenter considérablement le signal. La possibilité d'utiliser les électrons générés lors de la TNSA pour une excitation supplémentaire des rayons X caractéristiques est également à l'étude. Cela signifierait une combinaison de Particle-Induced X-ray Emission et Energy Dispersive X-ray fluorescence dans le même montage, ce qui augmenterait encore ses capacités [18].

Analyse des aérosols dans l'air

Ce travail démontre que la combinaison du PIXE et du XRF par laser permet de détecter des concentrations de gaz jusqu'à plusieurs centaines de ppm sans préparation complexe de l'échantillon. Si une mesure de référence est disponible, les concentrations relatives de gaz peuvent être estimées en comparant les hauteurs ou les aires des pics à l'aide de techniques d'ajustement spectral. Bien que des limitations dans le système de valve

actuel et le bruit de fond des rayons X empêchent une quantification fiable en dessous de 0.4%, la présence de Kr est encore clairement discernable à ce niveau. Avec une meilleure stabilité tir à tir du laser, une moyenne du signal sur plusieurs tirs et un contrôle plus précis du gaz, le système devrait atteindre des sensibilités de quelques centaines de ppm. Cette projection se base sur le fait que des signaux correspondant à de telles dilutions sont déjà détectables, mais ne sont pas encore contrôlés avec une précision suffisante et sont largement masqués par le bruit. Les défis d'identification des pics peuvent être abordés en restreignant la gamme d'éléments attendus et en intégrant une analyse assistée par logiciel, potentiellement améliorée par des algorithmes d'IA pour une meilleure détection des pics [117, 118]. Des routines automatisées déclenchées par des conditions de seuil permettraient en outre une surveillance continue des aérosols toxiques ou des particules fines [119, 120]. Les performances actuelles à ALLS démontrent la faisabilité du XPIF laser en quasi temps réel pour des applications telles que l'analyse des gaz d'échappement d'usines, la surveillance des décharges et le contrôle de la qualité de l'air urbain [23, 121, 122]. La contribution accrue du XRF pour les éléments à Z élevé rend également cette méthode adaptée à la détection d'espèces radioactives telles que le césium ou l'iode, libérées lors d'incidents nucléaires. La résolution du système permet même de distinguer des isotopes tels que le ^{134}Cs et le ^{137}Cs [123]. Bien que davantage de tirs soient nécessaires pour exciter suffisamment de rayons X à des concentrations de Kr plus faibles, la fréquence de répétition du laser de 0.625 Hz garantit que ce n'est pas un facteur limitant. Alors que les solutions de cibles stables à plus haute fréquence de répétition restent un goulot d'étranglement pour l'accélération de protons [124], certaines solutions atteignent déjà des taux de répétition de 1 Hz avec des jets d'hydrogène cryogéniques ayant une évolutivité attendue jusqu'à 1 kHz [125, 126]. Combiné à la disponibilité croissante d'accélérateurs laser compacts et rentables capables de fournir des protons de 3 à 5 MeV pour le PIXE [127], l'évolutivité du XPIF par laser semble prometteuse [23, 120]. Ce fait ne se limite pas seulement aux applications environnementales, mais à l'ensemble des opérations potentielles du XPIF.

Bibliography

[1] P. Puyuelo-Valdes, S. Vallières, M. Salvadori, S. Fourmaux, S. Payeur, J.-C. Kieffer, F. Hannachi, and P. Antici, "Combined laser-based X-ray fluorescence and particle-induced X-ray emission for versatile multi-element analysis," *Scientific Reports*, vol. 11, no. 1, p. 9998, May 2021. [Online]. Available: https://www.nature.com/articles/s41598-021-86657-6

[2] H. Sawada, Y. Sentoku, A. Bass, B. Griffin, R. Pandit, F. Beg, H. Chen, H. Mclean, A. Link, P. Patel, and Y. Ping, "Characterization of intense laser-produced fast electrons using hard x-rays via bremsstrahlung," *Journal of Physics B: Atomic, Molecular and Optical Physics*, vol. 48, 11 2015.

[3] A. Yogo, T. Maeda, T. Hori, H. Sakaki, K. Ogura, M. Nishiuchi, A. Sagisaka, H. Kiriyama, H. Okada, S. Kanazawa, T. Shimomura, Y. Nakai, M. Tanoue, F. Sasao, P. R. Bolton, M. Murakami, T. Nomura, S. Kawanishi, and K. Kondo, "Measurement of relative biological effectiveness of protons in human cancer cells using a laser-driven quasimonoenergetic proton beamline," *Applied Physics Letters*, vol. 98, no. 5, p. 053701, Jan. 2011. [Online]. Available: https://pubs.aip.org/apl/article/98/5/053701/931691/Measurement-of-relative-biological-effectiveness

[4] K. Ledingham, P. Bolton, N. Shikazono, and C.-M. Ma, "Towards Laser Driven Hadron Cancer Radiotherapy: A Review of Progress," *Applied Sciences*, vol. 4, no. 3, pp. 402–443, Sep. 2014. [Online]. Available: https://www.mdpi.com/2076-3417/4/3/402

[5] B. Dromey, M. Coughlan, L. Senje, M. Taylor, S. Kuschel, B. Villagomez-Bernabe, R. Stefanuik, G. Nersisyan, L. Stella, J. Kohanoff, M. Borghesi, F. Currell, D. Riley, D. Jung, C.-G. Wahlström, C. Lewis, and M. Zepf, "Picosecond metrology of laser-driven proton bursts," *Nature Communications*, vol. 7, no. 1, p. 10642, Feb. 2016. [Online]. Available: https://www.nature.com/articles/ncomms10642

[6] M. Scisciò, M. Barberio, C. Liberatore, S. Veltri, A. Laramée, L. Palumbo, F. Legaré, and P. Antici, "Analysis of induced stress on materials exposed to laser-plasma radiation during high-intensity laser experiments," *Applied Surface Science*, vol. 421, pp. 200–204, Nov. 2017. [Online]. Available: https://linkinghub.elsevier.com/retrieve/pii/S0169433216327040

[7] M. Barberio, M. Scisciò, S. Vallières, F. Cardelli, S. N. Chen, G. Famulari, T. Gangolf, G. Revet, A. Schiavi, M. Senzacqua, and P. Antici, "Laser-accelerated particle beams for stress testing of materials," *Nature Communications*, vol. 9, no. 1, p. 372, Jan. 2018. [Online]. Available: https://www.nature.com/articles/s41467-017-02675-x

[8] Z. Smit and M. Holc, "Differential PIXE measurements of thin metal layers," *Nuclear Instruments and Methods in Physics Research Section B: Beam Interactions with Materials and Atoms*, vol. 219-220, pp. 524–529, Jun. 2004. [Online]. Available: https://linkinghub.elsevier.com/retrieve/pii/S0168583X04001430

[9] H. R. Verma, *Atomic and nuclear analytical methods: XRF, Mössbauer, XPS, NAA and ion-beam spectroscopic techniques.* Berlin and Heidelberg: Springer, 2007.

[10] M. Barberio, S. Veltri, M. Scisciò, and P. Antici, "Laser-Accelerated Proton Beams as Diagnostics for Cultural Heritage," *Scientific Reports*, vol. 7, p. 40415, Mar. 2017. [Online]. Available: https://www.nature.com/articles/srep40415

[11] R. S. Popelka-Filcoff, "Proton-Induced X-Ray Emission Spectroscopy (PIXE): Applications in Archaeology," in *Encyclopedia of Global Archaeology.* Cham: Springer International Publishing, 2018, pp. 1–5. [Online]. Available: http://link.springer.com/10.1007/978-3-319-51726-1_342-2

[12] S. Vallières, P. Puyuelo-Valdes, M. Salvadori, C. Bienvenue, S. Payeur, E. d'Humières, and P. Antici, "The laser-driven ion acceleration beamline on the ALLS 200 TW for testing nanowire targets," in *Laser Acceleration of Electrons, Protons, and Ions V*, E. Esarey, C. B. Schroeder, and J. Schreiber, Eds., vol. 11037, International Society for Optics and Photonics. SPIE, 2019, p. 1103703. [Online]. Available: https://doi.org/10.1117/12.2520178

[13] D. N. Papadopoulos, J. P. Zou, C. L. Blanc, L. Ranc, F. Druon, L. Martin, A. Fréneaux, A. Beluze, N. Lebas, M. Chabanis, C. Bonnin, J. B. Accary, B. L. Garrec, F. Mathieu, and P. Audebert, "First commissioning results of the apollon laser on the 1 pw beam line," in *Conference on Lasers and Electro-Optics.* Optica Publishing Group, 2019, p. STu3E.4. [Online]. Available: https://opg.optica.org/abstract.cfm?URI=CLEO_SI-2019-STu3E.4

[14] L. Roso, "High repetition rate Petawatt lasers," *EPJ Web of Conferences*, vol. 167, p. 01001, 2018. [Online]. Available: https://www.epj-conferences.org/10.1051/epjconf/201816701001

[15] Centre de Recherche et de Restauration des Musées de France, "C2rmf - centre de recherche et de restauration des musées de france," 2025, accessed: 2025-03-26. [Online]. Available: https://c2rmf.fr/

[16] M. Massi, L. Giuntini, M. Chiari, N. Gelli, and P. Mandò, "The external beam microprobe facility in florence: Set-up and performance," *Nuclear Instruments and Methods in Physics Research Section B: Beam Interactions with Materials and Atoms*, vol. 190, pp. 276–282, 05 2002.

[17] L. Giuntini, M. Massi, and S. Calusi, "The external scanning proton microprobe of firenze: A comprehensive description," *Nuclear Instruments and Methods in Physics Research Section A: Accelerators, Spectrometers, Detectors and Associated Equipment*, vol. 576, pp. 266–273, 06 2007.

[18] F. Mirani, A. Maffini, F. Casamichiela, A. Pazzaglia, A. Formenti, D. Dellasega, V. Russo, D. Vavassori, D. Bortot, M. Huault, G. Zeraouli, V. Ospina, S. Malko, J. I. Apiñaniz, J. A. Pérez-Hernández, D. D. Luis, G. Gatti, L. Volpe, A. Pola, and M. Passoni, "Integrated quantitative pixe analysis and edx spectroscopy using a laser-driven particle source," *Science Advances*, vol. 7, no. 3, p. eabc8660, 2021. [Online]. Available: https://www.science.org/doi/abs/10.1126/sciadv.abc8660

[19] C. Brenner and G. Sarri, "Summary of working group 4: Application of compact and high-gradient accelerators," *Journal of Physics: Conference Series*, vol. 1596, p. 012034, 07 2020.

[20] L. Beck, M. Mayer, T. F. Silva, C. Berthier, and L. Pichon, "Combining pixe and ebs for the analysis of paint layers: Experiment and simulation highlight the influence of the pigment grain size," *Nuclear Instruments and Methods in Physics Research Section B: Beam Interactions with Materials and Atoms*, vol. 555, p. 165468, 2024. [Online]. Available: https://www.sciencedirect.com/science/article/pii/S0168583X24002386

[21] C.-C. Lee, S.-Y. Cai, T.-C. Chao, M.-J. Lin, and C.-J. Tung, "Depth dose characteristics of proton beams within therapeutic energy range using the particle therapy simulation framework (PTSim) Monte Carlo technique," *Biomedical Journal*, vol. 38, no. 5, p. 408, 2015. [Online]. Available: http://biomedj.cgu.edu.tw/pdfs/2015/38/5/images/BiomedJ_2015_38_5_408_167076.pdf

[22] E. B. Podgorsak, *Radiation physics for medical physicists*, third edition ed., ser. Graduate texts in physics. Cham: Springer, 2016.

[23] A. Bancuta, C. Stihi, I. V. Popescu, T. Badica, and G. V. Cimpoca, "Elemental analysis of aerosols using PIXE method," *Journal of Physics: Conference Series*, vol. 41, pp. 502–505, may 2006. [Online]. Available: https://iopscience.iop.org/article/10.1088/1742-6596/41/1/056

[24] E. A. Stefaniak, A. Buczynska, V. Novakovic, R. Kuduk, and R. V. Grieken, "Determination of chemical composition of individual airborne particles by

sem/edx and micro-raman spectrometry: A review," *Journal of Physics: Conference Series*, vol. 162, no. 1, p. 012019, apr 2009. [Online]. Available: https://dx.doi.org/10.1088/1742-6596/162/1/012019

[25] M. Toyoda, K. Kaibuchi, M. Nagasono, Y. Terada, T. Tanabe, S. Hayakawa, and J. Kawai, "X-ray analysis of a single aerosol particle with combination of scanning electron microscope and synchrotron radiation x-ray microscope," *Spectrochimica Acta Part B: Atomic Spectroscopy*, vol. 59, no. 8, pp. 1311–1315, 2004, 10th Symposium on Total Reflection X-Ray Fluorescence Analysis and 39th Discussion Meeting on Chemical Analysis. [Online]. Available: https://www.sciencedirect.com/science/article/pii/S058485470400151X

[26] National Institute of Standards and Technology (NIST), "PSTAR: Stopping-Power and Range Tables for Protons," https://physics.nist.gov/PhysRefData/Star/Text/PSTAR.html, 2025, accessed: 17 June 2025.

[27] ——, "ESTAR: Stopping-Power and Range Tables for Electrons," 2025, accessed: 2025-04-02. [Online]. Available: https://physics.nist.gov/PhysRefData/Star/Text/ESTAR.html

[28] J. H. Hubbell and S. M. Seltzer, "X-ray mass attenuation coefficients," 2004, data last updated in July 2004. The original publication is NISTIR 5632 (1995). [Online]. Available: https://www.nist.gov/pml/x-ray-mass-attenuation-coefficients

[29] R. E. Van Grieken, A. A. Markowicz, and R. Van Grieken, Eds., *Handbook of x-ray spectrometry*, 2nd ed., ser. Practical spectroscopy. New York, NY Basel: Dekker, 2002, no. 29.

[30] K. Ishii and S. Morita, "Theoretical estimation of pixe detection limits," *Nuclear Instruments and Methods in Physics Research Section B: Beam Interactions with Materials and Atoms*, vol. 34, no. 2, pp. 209–216, 1988. [Online]. Available: https://www.sciencedirect.com/science/article/pii/0168583X88907458

[31] Y. Wang and M. Nastasi, *Handbook of modern ion beam materials analysis*, 2nd ed. Warendale, PA: Materials Research Society, 2009.

[32] N. A. Dyson, *X-rays in atomic and nuclear physics*, 2nd ed. Cambridge: Cambridge Univ. Press, 1990. [Online]. Available: http://www.loc.gov/catdir/description/cam023/88038330.html

[33] M. Uo, T. Wada, and T. Sugiyama, "Applications of x-ray fluorescence analysis (xrf) to dental and medical specimens," *Japanese Dental Science Review*, vol. 51, no. 1, pp. 2–9, 2015. [Online]. Available: https://www.sciencedirect.com/science/article/pii/S1882761614000258

[34] A. Maksimchuk, S. Gu, K. Flippo, D. Umstadter, and A. Y. Bychenkov, "Forward ion acceleration in thin films driven by a high-intensity laser," *Physical Review Letters*, vol. 84, no. 18, p. 4108 – 4111, 2000. [Online]. Available: https://www.scopus.com/inward/record.uri?eid=2-s2.0-0001008329&doi=10.1103%2fPhysRevLett.84.4108&partnerID=40&md5=c2f4433256a9afb0b2d4f0d2b8cc502a

[35] E. L. Clark, K. Krushelnick, J. R. Davies, M. Zepf, M. Tatarakis, F. N. Beg, A. Machacek, P. A. Norreys, M. I. K. Santala, I. Watts, and A. E. Dangor, "Measurements of energetic proton transport through magnetized plasma from intense laser interactions with solids," *Phys. Rev. Lett.*, vol. 84, pp. 670–673, Jan 2000. [Online]. Available: https://link.aps.org/doi/10.1103/PhysRevLett.84.670

[36] P. McKenna, D. Neely, R. Bingham, and D. A. Jaroszynski, Eds., *Laser-plasma interactions and applications*, ser. Scottish graduate series. Switzerland and Heidelberg and New York: Springer, 2013.

[37] M. Passoni, L. Bertagna, and A. Zani, "Target normal sheath acceleration: theory, comparison with experiments and future perspectives," *New Journal of Physics*, vol. 12, no. 4, p. 045012, Apr. 2010. [Online]. Available: https://iopscience.iop.org/article/10.1088/1367-2630/12/4/045012

[38] S. C. Wilks, A. B. Langdon, T. E. Cowan, M. Roth, M. Singh, S. Hatchett, M. H. Key, D. Pennington, A. MacKinnon, and R. A. Snavely, "Energetic proton generation in ultra-intense laser–solid interactions," *Physics of Plasmas*, vol. 8, no. 2, pp. 542–549, Feb. 2001. [Online]. Available: https://pubs.aip.org/pop/article/8/2/542/264618/Energetic-proton-generation-in-ultra-intense-laser

[39] J. Schreiber, "Ion acceleration driven by high-intensity laser pulses," Ph.D. dissertation, lmu, 2006.

[40] S. Vallières, "Towards reliable, intense and high repetition-rate laser-driven ion beamlines," Ph.D. dissertation, 12 2020.

[41] M. Kaluza, J. Schreiber, M. I. K. Santala, G. D. Tsakiris, K. Eidmann, J. Meyer-ter Vehn, and K. J. Witte, "Influence of the laser prepulse on proton acceleration in thin-foil experiments," *Phys. Rev. Lett.*, vol. 93, p. 045003, Jul 2004. [Online]. Available: https://link.aps.org/doi/10.1103/PhysRevLett.93.045003

[42] P. Mora, "Plasma expansion into a vacuum," *Phys. Rev. Lett.*, vol. 90, p. 185002, May 2003. [Online]. Available: https://link.aps.org/doi/10.1103/PhysRevLett.90.185002

[43] W. H. Bragg and R. K. and, "Xxxix. on the particles of radium, and their loss of range in passing through various atoms and molecules," *The London, Edinburgh,*

and Dublin Philosophical Magazine and Journal of Science, vol. 10, no. 57, pp. 318–340, 1905. [Online]. Available: https://doi.org/10.1080/14786440509463378

[44] H. Paganetti, Ed., *Proton therapy physics*, second edition ed., ser. Series in medical physics and biomedical engineering. Boca Raton and London and New York and Berlin: CRC Press Taylor & Francis Group and ProQuest Ebook Central, 2019, vol. 20. [Online]. Available: https://ebookcentral.proquest.com/lib/kxp/detail.action?docID=5602097

[45] H. Paul and A. Schinner, "Statistical analysis of stopping data for protons and alphas in compounds," *Nuclear Instruments and Methods in Physics Research Section B: Beam Interactions with Materials and Atoms*, vol. 249, no. 1-2, pp. 1–5, Aug. 2006. [Online]. Available: https://linkinghub.elsevier.com/retrieve/pii/S0168583X06002461

[46] J. A. van Bokhoven, *X-Ray Absorption and X-Ray Emission Spectroscopy: Theory and Applications*, 1st ed. New York: John Wiley & Sons Incorporated, 2015. [Online]. Available: https://ebookcentral.proquest.com/lib/kxp/detail.action?docID=4332385

[47] F. H. Attix, *Introduction to radiological physics and radiation dosimetry*, ser. Physics textbook. Weinheim: Wiley-VCH, 2004.

[48] J. H. Hubbell and S. M. Seltzer, "X-Ray Mass Attenuation Coefficients for Cu (Z=29)," NIST Physical Measurement Laboratory, Gaithersburg, MD, 2004, version 1.4. Online database. Accessed April 29, 2025. [Online]. Available: https://physics.nist.gov/PhysRefData/XrayMassCoef/ElemTab/z29.html

[49] M. J. Berger, J. H. Hubbell, S. M. Seltzer, J. Chang, J. S. Coursey, R. Sukumar, and D. S. Zucker, "XCOM: Photon Cross Sections Database," NIST Standard Reference Database 8 (XGAM), Version 1.5, Gaithersburg, MD, 2019, online: http://physics.nist.gov/xcom. Accessed April 30, 2025. [Online]. Available: http://physics.nist.gov/xcom

[50] J. F. Ziegler, M. D. Ziegler, and J. P. Biersack, "SRIM - The stopping and range of ions in matter (2010)," *Nuclear Instruments and Methods in Physics Research Section B: Beam Interactions with Materials and Atoms*, vol. 268, no. 11-12, pp. 1818–1823, jun 2010, describes the SRIM software available at http://www.srim.org/. [Online]. Available: https://doi.org/10.1016/j.nimb.2010.02.091

[51] M. O. Krause, C. W. Nestor, Jr, C. J. Sparks, Jr, and E. Ricci, "X-ray fluorescence cross sections for k and l x rays of the elements," Oak Ridge National

Lab. (ORNL), Oak Ridge, TN (United States), Tech. Rep., 06 1978. [Online]. Available: https://www.osti.gov/biblio/7032250

[52] B. E. Warren, *X-ray diffraction*, ser. Addison-Wesley series in metallurgy and materials. Reading, Mass. u.a.: Addison-Wesley, 1969. [Online]. Available: https://permalink.obvsg.at/AC04046912

[53] R. W. James, *The optical principles of the diffraction of X-Rays*, repr. [der ausg. london, 1962] ed., ser. Orginally publ. as The Crystalline State, Vol. 2 in 1948. Woodbridge, Conn.: Ox Bow Pr, 1982.

[54] B. Clauß and A. Schubert, "Milling of an aluminium matrix composite using mcd-tipped tools with adjusted corner and minor cutting edge geometries," *Journal of Composites Science*, vol. 5, p. 235, 09 2021.

[55] "face-centered cubic," https://www.wikidata.org/wiki/Q3006714, nov 2023, wikidata item Q3006714. Last modified: 22 November 2023. Accessed: 8 May 2025.

[56] D. Boer, "Calculation of x-ray fluorescence intensities from bulk and multilayer samples," *X-Ray Spectrometry*, vol. 19, pp. 145 – 154, 06 1990.

[57] G. F. Knoll, *Radiation detection and measurement*, 4th ed. Hoboken, NJ: Wiley, 2010.

[58] J. van Abbema, M.-J. van Goethem, J. Mulder, A. Biegun, M. Greuter, A. van der Schaaf, S. Brandenburg, and E. van der Graaf, "High accuracy proton relative stopping power measurement," *Nuclear Instruments and Methods in Physics Research Section B: Beam Interactions with Materials and Atoms*, vol. 436, pp. 99–106, 2018. [Online]. Available: https://www.sciencedirect.com/science/article/pii/S0168583X18305482

[59] F. Salvat, "Bethe stopping-power formula and its corrections," *Phys. Rev. A*, vol. 106, p. 032809, Sep 2022. [Online]. Available: https://link.aps.org/doi/10.1103/PhysRevA.106.032809

[60] J. F. Ziegler, "Stopping of energetic light ions in elemental matter," *Journal of Applied Physics*, vol. 85, no. 3, pp. 1249–1272, 1999.

[61] D. Cohen, J. Crawford, and R. Siegele, "K, l, and m shell datasets for pixe spectrum fitting and analysis," *Nuclear Instruments and Methods in Physics Research Section B: Beam Interactions with Materials and Atoms*, vol. 363, 08 2015.

[62] D. Cohen and M. Harrigan, "K- and l-shell ionization cross sections for protons and helium ions calculated in the ecpssr theory," *Atomic Data and*

Nuclear Data Tables, vol. 33, no. 2, pp. 255–343, 1985. [Online]. Available: https://www.sciencedirect.com/science/article/pii/0092640X8590004X

[63] M. Pia, G. Weidenspointner, M. Augelli, L. Quintieri, P. Saracco, M. Sudhakar, and A. Zoglauer, "Pixe simulation with geant4," *Nuclear Science, IEEE Transactions on*, vol. 56, pp. 3614 – 3649, 01 2010.

[64] M. Batic, M. Pia, and S. Cipolla, "Isicsoo: a class for the calculation of ionization cross sections from ecpssr and pwba theory," *Computer Physics Communications*, vol. 183, 10 2011.

[65] Physics Open Lab, "Bremsstrahlung Radiation," Blog Post, Physics Open Lab, August 2017, accessed April 30, 2025. [Online]. Available: https://physicsopenlab.org/2017/08/02/bremsstrahlung-radiation/

[66] L. C. Jarrott, A. J. Kemp, L. Divol, D. Mariscal, B. Westover, C. McGuffey, F. N. Beg, M. Suggit, C. Chen, D. Hey, B. Maddox, J. Hawreliak, H.-S. Park, B. Remington, M. S. Wei, and A. MacPhee, "K-alpha and bremsstrahlung x-ray radiation backlighter sources from short pulse laser driven silver targets as a function of laser pre-pulse energy," *Physics of Plasmas*, vol. 21, no. 3, p. 031211, 02 2014. [Online]. Available: https://doi.org/10.1063/1.4865230

[67] B. M. Hegelich, B. J. Albright, J. Cobble, K. Flippo, S. Letzring, M. Paffett, H. Ruhl, J. Schreiber, R. K. Schulze, and J. C. Fernández, "Laser acceleration of quasi-monoenergetic MeV ion beams," *Nature*, vol. 439, no. 7075, pp. 441–444, Jan. 2006. [Online]. Available: https://www.nature.com/articles/nature04400

[68] C. A. J. Palmer, N. P. Dover, I. Pogorelsky, M. Babzien, G. I. Dudnikova, M. Ispiriyan, M. N. Polyanskiy, J. Schreiber, P. Shkolnikov, V. Yakimenko, and Z. Najmudin, "Monoenergetic Proton Beams Accelerated by a Radiation Pressure Driven Shock," *Physical Review Letters*, vol. 106, no. 1, p. 014801, Jan. 2011. [Online]. Available: https://link.aps.org/doi/10.1103/PhysRevLett.106.014801

[69] D. Haberberger, S. Tochitsky, F. Fiuza, C. Gong, R. A. Fonseca, L. O. Silva, W. B. Mori, and C. Joshi, "Collisionless shocks in laser-produced plasma generate monoenergetic high-energy proton beams," *Nature Physics*, vol. 8, no. 1, pp. 95–99, Jan. 2012. [Online]. Available: https://www.nature.com/articles/nphys2130

[70] T. Toncian, M. Borghesi, J. Fuchs, E. d'Humières, P. Antici, P. Audebert, E. Brambrink, C. A. Cecchetti, A. Pipahl, L. Romagnani, and O. Willi, "Ultrafast Laser-Driven Microlens to Focus and Energy-Select Mega-Electron Volt Protons," *Science*, vol. 312, no. 5772, pp. 410–413, Apr. 2006. [Online]. Available: https://www.science.org/doi/10.1126/science.1124412

[71] S. Ter-Avetisyan, M. Schnürer, R. Polster, P. Nickles, and W. Sandner, "First demonstration of collimation and monochromatisation of a laser accelerated proton burst," *Laser and Particle Beams*, vol. 26, no. 4, pp. 637–642, Dec. 2008. [Online]. Available: https://www.cambridge.org/core/product/identifier/S0263034608000712/type/journal_article

[72] K. Harres, I. Alber, A. Tauschwitz, V. Bagnoud, H. Daido, M. Günther, F. Nürnberg, A. Otten, M. Schollmeier, J. Schütrumpf, M. Tampo, and M. Roth, "Beam collimation and transport of quasineutral laser-accelerated protons by a solenoid field," *Physics of Plasmas*, vol. 17, no. 2, p. 023107, Feb. 2010. [Online]. Available: https://pubs.aip.org/pop/article/17/2/023107/261798/Beam-collimation-and-transport-of-quasineutral

[73] M. Schollmeier, S. Becker, M. Geißel, K. A. Flippo, A. Blažević, S. A. Gaillard, D. C. Gautier, F. Grüner, K. Harres, M. Kimmel, F. Nürnberg, P. Rambo, U. Schramm, J. Schreiber, J. Schütrumpf, J. Schwarz, N. A. Tahir, B. Atherton, D. Habs, B. M. Hegelich, and M. Roth, "Controlled Transport and Focusing of Laser-Accelerated Protons with Miniature Magnetic Devices," *Physical Review Letters*, vol. 101, no. 5, p. 055004, Aug. 2008. [Online]. Available: https://link.aps.org/doi/10.1103/PhysRevLett.101.055004

[74] I. Hofmann, "Performance of solenoids versus quadrupoles in focusing and energy selection of laser accelerated protons," *Physical Review Special Topics - Accelerators and Beams*, vol. 16, no. 4, p. 041302, Apr. 2013. [Online]. Available: https://link.aps.org/doi/10.1103/PhysRevSTAB.16.041302

[75] C. L. C. Lacoste, E. Catrix, S. Vallières, A. Hirsch-Passicos, T. Guilberteau, M. Lafargue, J. Lopez, I. Manek-Hönninger, S. Fourmaux, D. Raffestin, E. d'Humières, P. Antici, and M. Bardon, "Experimental and numerical investigation of the impact of helical coil targets on laser-driven proton and carbon accelerations," *Matter and Radiation at Extremes*, vol. 10, no. 3, p. 037602, 03 2025. [Online]. Available: https://doi.org/10.1063/5.0257518

[76] S. Nakamura, M. Ikegami, Y. Iwashita, T. Shirai, H. Tongu, H. Souda, H. Daido, M. Mori, M. Kado, A. Sagisaka, K. Ogura, M. Nishiuchi, S. Orimo, Y. Hayashi, A. Yogo, A. S. Pirozhkov, S. V. Bulanov, T. Esirkepov, A. Nagashima, T. Kimura, T. Tajima, T. Takeuchi, A. Fukumi, Z. Li, and A. Noda, "High-Quality Laser-Produced Proton Beam Realized by the Application of a Synchronous RF Electric Field," *Japanese Journal of Applied Physics*, vol. 46, no. 8L, p. L717, Aug. 2007. [Online]. Available: https://iopscience.iop.org/article/10.1143/JJAP.46.L717

[77] T. Burris-Mog, K. Harres, F. Nürnberg, S. Busold, M. Bussmann, O. Deppert, G. Hoffmeister, M. Joost, M. Sobiella, A. Tauschwitz, B. Zielbauer, V. Bagnoud,

T. Herrmannsdoerfer, M. Roth, and T. E. Cowan, "Laser accelerated protons captured and transported by a pulse power solenoid," *Physical Review Special Topics - Accelerators and Beams*, vol. 14, no. 12, p. 121301, Dec. 2011. [Online]. Available: https://link.aps.org/doi/10.1103/PhysRevSTAB.14.121301

[78] S. N. Chen, M. Gauthier, D. P. Higginson, S. Dorard, F. Mangia, R. Riquier, S. Atzeni, J.-R. Marquès, and J. Fuchs, "Monochromatic short pulse laser produced ion beam using a compact passive magnetic device," *Review of Scientific Instruments*, vol. 85, no. 4, p. 043504, Apr. 2014. [Online]. Available: https://pubs.aip.org/rsi/article/85/4/043504/357778/Monochromatic-short-pulse-laser-produced-ion-beam

[79] E. Wilson and B. J. Holzer, "Beam Dynamics," in *Particle Physics Reference Library*, S. Myers and H. Schopper, Eds. Cham: Springer International Publishing, 2020, pp. 15–50. [Online]. Available: http://link.springer.com/10.1007/978-3-030-34245-6_2

[80] "TPR280/TPR281 Operating Instrucitons," https://www.pfeiffer-vacuum.com/global/en/shop/products/PT_R26_953_B, Pfeiffer Vacuum, jun 2024, accessed: 2025-05-12.

[81] P. W. Atkins, J. de Paula, and J. J. Keeler, *Atkins' physical chemistry*, eleventh edition ed. Oxford and New York: Oxford University Press, 2018.

[82] National Oceanic and Atmospheric Administration (NOAA), "Jetstream - an online school for weather: Atmosphere," 2025, accessed: 2025-03-26. [Online]. Available: https://www.noaa.gov/jetstream/atmosphere

[83] R. Prasad, D. Doria, S. Ter-Avetisyan, P. Foster, K. Quinn, L. Romagnani, C. Brenner, J. Green, P. Gallegos, M. Streeter, D. Carroll, O. Tresca, N. Dover, C. Palmer, J. Schreiber, D. Neely, Z. Najmudin, P. McKenna, M. Zepf, and M. Borghesi, "Calibration of thomson parabola—mcp assembly for multi-mev ion spectroscopy," *Nuclear Instruments and Methods in Physics Research Section A: Accelerators, Spectrometers, Detectors and Associated Equipment*, vol. 623, no. 2, pp. 712–715, 2010, 1rs International Conference on Frontiers in Diagnostics Technologies. [Online]. Available: https://www.sciencedirect.com/science/article/pii/S0168900210002767

[84] P. Bolton, M. Borghesi, C. Brenner, D. Carroll, C. De Martinis, F. Fiorini, A. Flacco, V. Floquet, J. Fuchs, P. Gallegos, D. Giove, J. Green, S. Green, B. Jones, D. Kirby, P. McKenna, D. Neely, F. Nuesslin, R. Prasad, S. Reinhardt, M. Roth, U. Schramm, G. Scott, S. Ter-Avetisyan, M. Tolley, G. Turchetti, and J. Wilkens, "Instrumentation for diagnostics and control of laser-accelerated proton

(ion) beams," *Physica Medica*, vol. 30, no. 3, pp. 255–270, May 2014. [Online]. Available: https://linkinghub.elsevier.com/retrieve/pii/S1120179713003979

[85] *APD 2 PS 97X79/32/25/8 I 40:1 NR P43*, Photonis USA, Inc., accessed on June 4, 2025. [Online]. Available: https://www.photonis.com

[86] *BFLY-PGE-13H2M-CS*, FLIR Integrated Imaging Solutions, Inc., accessed on June 4, 2025. [Online]. Available: https://www.flir.com

[87] V. Scuderi, G. Milluzzo, D. Doria, A. Alejo, A. Amico, N. Booth, G. Cuttone, J. Green, S. Kar, G. Korn, G. Larosa, R. Leanza, P. Martin, P. McKenna, H. Padda, G. Petringa, J. Pipek, L. Romagnani, F. Romano, A. Russo, F. Schillaci, G. Cirrone, D. Margarone, and M. Borghesi, "TOF diagnosis of laser accelerated, high-energy protons," *Nuclear Instruments and Methods in Physics Research Section A: Accelerators, Spectrometers, Detectors and Associated Equipment*, vol. 978, p. 164364, Oct. 2020. [Online]. Available: https://linkinghub.elsevier.com/retrieve/pii/S0168900220307610

[88] V. Scuderi, G. Milluzzo, A. Alejo, A. Amico, N. Booth, G. Cirrone, D. Doria, J. Green, S. Kar, G. Larosa, R. Leanza, D. Margarone, P. McKenna, H. Padda, G. Petringa, J. Pipek, L. Romagnani, F. Romano, F. Schillaci, M. Borghesi, G. Cuttone, and G. Korn, "Time of Flight based diagnostics for high energy laser driven ion beams," *Journal of Instrumentation*, vol. 12, no. 03, pp. C03 086–C03 086, Mar. 2017. [Online]. Available: https://iopscience.iop.org/article/10.1088/1748-0221/12/03/C03086

[89] W. Hong, X.-L. Wen, L. Wei, B. Zhu, Y.-C. Wu, K.-G. Dong, C.-Y. Jiao, B. Wu, Y.-L. He, F.-Q. Zhang, W.-M. Zhou, and Y.-Q. Gu, "Detailed calibration of the PI-LCX:1300 high performance single photon counting hard x-ray CCD camera," *Chinese Physics B*, vol. 26, no. 2, p. 025204, feb 2017. [Online]. Available: https://iopscience.iop.org/article/10.1088/1674-1056/26/2/025204

[90] A. C. Thompson, D. T. Attwood, M. R. Howells, J. B. Kortright, A. L. Robinson, J. H. Underwood, K.-J. Kim, J. Kirz, I. Lindau, P. Pianetta, H. Winick, G. P. Williams, and J. H. Scofield, "X-Ray Data Booklet," p. 457.

[91] D. H. Lumb, E. G. Chowanietz, and A. Wells, "X-ray measurements of charge diffusion effects in eev ltd. charge-coupled devices," *Optical Engineering*, vol. 26, no. 8, pp. 773–778, 1987.

[92] A. Owens, G. Fraser, and K. J. McCarthy, "On the experimental determination of the fano factor in si at soft x-ray wavelengths," *Nuclear Instruments and Methods in Physics Research Section A: Accelerators, Spectrometers, Detectors*

and Associated Equipment, vol. 491, no. 3, pp. 437–443, 2002. [Online]. Available: https://www.sciencedirect.com/science/article/pii/S0168900202011786

[93] Princeton Instruments, *PI-SX: 1300 High-Sensitivity Camera System Datasheet*, Princeton Instruments, rev C1. [Online]. Available: https://www.princetoninstruments.com/products/ccd-cameras/pi-sx-1300

[94] C. Fourment, N. Arazam, C. Bonte, T. Caillaud, D. Descamps, F. Dorchies, M. Harmand, S. Hulin, S. Petit, and J. J. Santos, "Broadband, high dynamics and high resolution charge coupled device-based spectrometer in dynamic mode for multi-kev repetitive x-ray sources," *Review of Scientific Instruments*, vol. 80, no. 8, p. 083505, 08 2009. [Online]. Available: https://doi.org/10.1063/1.3189004

[95] S. Fourmaux, S. Corde, K. Ta Phuoc, P. M. Leguay, S. Payeur, P. Lassonde, S. Gnedyuk, G. Lebrun, C. Fourment, V. Malka, S. Sebban, A. Rousse, and J. C. Kieffer, "Demonstration of the synchrotron-type spectrum of laser-produced betatron radiation," *New Journal of Physics*, vol. 13, no. 3, p. 033017, mar 2011. [Online]. Available: https://dx.doi.org/10.1088/1367-2630/13/3/033017

[96] F. Boivin, S. Vallières, S. Fourmaux, S. Payeur, and P. Antici, "Quantitative laser-based x-ray fluorescence and particle-induced x-ray emission," *New Journal of Physics*, vol. 24, no. 5, p. 053018, May 2022. [Online]. Available: https://iopscience.iop.org/article/10.1088/1367-2630/ac6767

[97] M. Kavčič, M. Žitnik, K. Bučar, and J. Szlachetko, "Application of wavelength dispersive X-ray spectroscopy to improve detection limits in X-ray analysis," *X-Ray Spectrometry*, vol. 40, no. 1, pp. 2–6, jan 2011. [Online]. Available: https://analyticalsciencejournals.onlinelibrary.wiley.com/doi/10.1002/xrs.1291

[98] K. Janssens, Ed., *Microscopic X-ray fluorescence analysis*. Chichester and Weinheim: Wiley, 2000.

[99] H. Matsumoto, H. Sakaki, Y. Watanabe, T. Endo, M. Hata, K. Kondo, and K. Nagashima, "Evaluating beam neutralization and transport dynamics in laser-driven ion accelerators," in *Proc. LINAC2024*, 2024, pp. 502–505, paper TUPB087. [Online]. Available: https://accelconf.web.cern.ch/linac2024/pdf/TUPB087.pdf

[100] P. Antici, B. Albertazzi, P. Audebert, S. Buffechoux, F. Hannachi, E. d'Humières, F. Gobet, T. Grismayer, A. Mancic, M. Nakatsutsumi, C. Plaisir, L. Romagnani, M. Tarisien, H. Pépin, Y. Sentoku, and J. Fuchs, "Measuring hot electron distributions in intense laser interaction with dense matter," *New Journal of Physics*, vol. 14, no. 6, p. 063023, Jun. 2012. [Online]. Available: https://iopscience.iop.org/article/10.1088/1367-2630/14/6/063023

[101] P. Antici, J. Fuchs, M. Borghesi, L. Gremillet, T. Grismayer, Y. Sentoku, E. d'Humières, C. A. Cecchetti, A. Mančić, A. C. Pipahl, T. Toncian, O. Willi, P. Mora, and P. Audebert, "Hot and cold electron dynamics following high-intensity laser matter interaction," *Phys. Rev. Lett.*, vol. 101, p. 105004, Sep 2008. [Online]. Available: https://link.aps.org/doi/10.1103/PhysRevLett.101.105004

[102] E. Lefebvre, L. Gremillet, A. Levy, R. Nuter, P. Antici, M. Carrie, T. Ceccotti, M. Drouin, J. Fuchs, V. Malka, and D. Neely, "Proton acceleration by moderately relativistic laser pulses interacting with solid density targets," *New Journal of Physics*, vol. 12, Apr. 2010.

[103] J. J. Santos, F. Amiranoff, S. D. Baton, L. Gremillet, M. Koenig, E. Martinolli, M. Rabec Le Gloahec, C. Rousseaux, D. Batani, A. Bernardinello, G. Greison, and T. Hall, "Fast Electron Transport in Ultraintense Laser Pulse Interaction with Solid Targets by Rear-Side Self-Radiation Diagnostics," *Physical Review Letters*, vol. 89, no. 2, p. 025001, Jun. 2002. [Online]. Available: https://link.aps.org/doi/10.1103/PhysRevLett.89.025001

[104] S. D. Baton, J. J. Santos, F. Amiranoff, H. Popescu, L. Gremillet, M. Koenig, E. Martinolli, O. Guilbaud, C. Rousseaux, M. Rabec Le Gloahec, T. Hall, D. Batani, E. Perelli, F. Scianitti, and T. E. Cowan, "Evidence of Ultrashort Electron Bunches in Laser-Plasma Interactions at Relativistic Intensities," *Physical Review Letters*, vol. 91, no. 10, p. 105001, Sep. 2003. [Online]. Available: https://link.aps.org/doi/10.1103/PhysRevLett.91.105001

[105] V. Istokskaia, B. Lefebvre, R. Versaci, D. B. Dreghici, D. Doria, F. Grepl, V. Olšovcová, F. Schillaci, S. Stanček, M. Tryus, and et al., "Real-time bremsstrahlung detector as a monitoring tool for laser–plasma proton acceleration," *High Power Laser Science and Engineering*, vol. 12, p. e57, 2024.

[106] X. Llovet, F. Salvat, D. Bote, F. Salvat-Pujol, A. Jablonski, and C. J. Powell, *NIST Database of Cross Sections for Inner-Shell Ionization by Electron or Positron Impact, Version 1.0.* Gaithersburg, Maryland: National Institute of Standards and Technology, 2014, nIST Standard Reference Database 164. [Online]. Available: https://www.nist.gov/srd/nist-standard-reference-database-164

[107] M. S. del Rio, A. Brunetti, B. Golosio, A. Somogyi, and A. Simionovici, "xraylib: X-ray matter interaction cross sections tables, version 2.3," 2024, accessed: 2025-03-27. [Online]. Available: http://ftp.esrf.fr/pub/scisoft/xraylib/xraylib_tables_v2.3.pdf

[108] M. N. Nader and D. E. Fleming, "Assessment of alternative methods for analyzing X-ray fluorescence spectra," *Applied Radiation and Isotopes*, vol. 146, pp.

133–138, apr 2019. [Online]. Available: https://linkinghub.elsevier.com/retrieve/pii/S096980431831087X

[109] M. Scisciò, M. Barberio, C. Liberatore, S. Veltri, A. Laramée, L. Palumbo, F. Legaré, and P. Antici, "Analysis of induced stress on materials exposed to laser-plasma radiation during high-intensity laser experiments," *Applied Surface Science*, vol. 421, pp. 200–204, 2017, 11th International Conference on Surfaces, Coatings and Nanostructured Materials. [Online]. Available: https://www.sciencedirect.com/science/article/pii/S0169433216327040

[110] M. Barberio, S. Vallières, M. Scisciò, G. Kolhatkar, A. Ruediger, and P. Antici, "Graphitization of diamond by laser-accelerated proton beams," *Carbon*, vol. 139, pp. 531–537, 2018. [Online]. Available: https://www.sciencedirect.com/science/article/pii/S0008622318305876

[111] S. Shibata, H. Kamiyanagi, T. Okano, and A. Kitamura, "New evaluation method for cross-contamination of ion implantation by using grazing angle incidence pixe in photo-resist," *IEEE Transactions on Semiconductor Manufacturing*, vol. 23, no. 3, pp. 423–428, 2010.

[112] R. S. Popelka-Filcoff, *Proton-Induced X-Ray Emission Spectroscopy (PIXE): Applications in Archaeology*. Cham: Springer International Publishing, 2020, pp. 8953–8957. [Online]. Available: https://doi.org/10.1007/978-3-030-30018-0_342

[113] K. S. Johnson, A. Laskin, J. L. Jimenez, V. Shutthanandan, L. T. Molina, D. Salcedo, K. Dzepina, and M. J. Molina, "Comparative analysis of urban atmospheric aerosol by particle-induced x-ray emission (pixe), proton elastic scattering analysis (pesa), and aerosol mass spectrometry (ams)," *Environmental Science & Technology*, vol. 42, no. 17, pp. 6619–6624, 2008.

[114] M. Xu, Y. Chu, G. Wang, M. Qiu, and L. Zheng, "An upgraded external beam pixe setup for multielemental analysis of atmospheric aerosol samples," *X-Ray Spectrometry*, vol. 47, no. 1, pp. 79–85, 2018. [Online]. Available: https://analyticalsciencejournals.onlinelibrary.wiley.com/doi/abs/10.1002/xrs.2814

[115] E. Catrix, F. Boivin, K. Langlois, S. Vallières, C. Boynukara, S. Fourmaux, and P. Antici, "Stable high repetition-rate laser-driven proton beam production for multidisciplinary applications on the advanced laser light source ion beamline," *Review of Scientific Instruments*, vol. 94, 10 2023.

[116] L. Giuffrida, F. Schillaci, F. Grepl, M. Tryus, S. Stancek, A. Velyhan, V. Istokskaia, G. Petringa, G. Cirrone, J. Cupal, L. Koubikova, D. Peceli, J. A. Jarboe, T. Chagovets, V. Kantarelou, N. Gamaiunova, A. Hadjikyriacou,

J. Psikal, S. Kar, M. Borghesi, B. Rus, and D. Margarone, "Commissioning experiments at the ELIMAIA user beamline (Conference Presentation)," in *Laser Acceleration of Electrons, Protons, and Ions VII*, S. S. Bulanov, C. B. Schroeder, J. Schreiber, D. A. Jaroszynski, and M. S. Hur, Eds., vol. PC12579, International Society for Optics and Photonics. SPIE, 2023, p. PC125790S. [Online]. Available: https://doi.org/10.1117/12.2665598

[117] S. Kogou, L. Lee, G. Shahtahmassebi, and H. Liang, "A new approach to the interpretation of xrf spectral imaging data using neural networks," *X-Ray Spectrometry*, vol. 50, 08 2020.

[118] V. Andrić, G. Kvaščev, M. Cvetanovic, S. Stojanovic, N. Bacanin, and M. D. Gajić-Kvaščev, "Deep learning assisted xrf spectra classification," *Scientific Reports*, vol. 14, 02 2024.

[119] W. Maenhaut, "Present role of PIXE in atmospheric aerosol research," *Nuclear Instruments and Methods in Physics Research Section B: Beam Interactions with Materials and Atoms*, vol. 363, pp. 86–91, nov 2015. [Online]. Available: https://linkinghub.elsevier.com/retrieve/pii/S0168583X15006217

[120] M. Chiari, E. Yubero, G. Calzolai, F. Lucarelli, J. Crespo, N. Galindo, J. Nicolás, M. Giannoni, and S. Nava, "Comparison of pixe and xrf analysis of airborne particulate matter samples collected on teflon and quartz fibre filters," *Nuclear Instruments and Methods in Physics Research Section B: Beam Interactions with Materials and Atoms*, vol. 417, 08 2017.

[121] A. Onjia, N. Raes, and W. Maenhaut, "Particle-induced x-ray emission spectrometry of size-fractionated atmospheric aerosols," 01 2002.

[122] W. Maenhaut, N. Raes, and W. Wang, "Analysis of atmospheric aerosols by particle-induced X-ray emission, instrumental neutron activation analysis, and ion chromatography," *Nuclear Instruments and Methods in Physics Research Section B: Beam Interactions with Materials and Atoms*, vol. 269, no. 22, pp. 2693–2698, nov 2011. [Online]. Available: https://linkinghub.elsevier.com/retrieve/pii/S0168583X11007890

[123] National Nuclear Data Center (NNDC), "NuDat 3," https://www.nndc.bnl.gov/nudat3/, Brookhaven National Laboratory (BNL), 2025, accessed: June 25, 2025. NuDat 3 is an online database for nuclear structure and decay data.

[124] L. R. He, M. Bachhammer, F. Balling, S. Biswas, L. Doyle, S. Gerlach, I. Hofrichter, M. Kharbedia, J. Liese, M. De Marco, T. Pohle, A. Praßelsperger, A.-K. Schmidt, F. Schweiger, M. F. Kling, S. Karsch, and J. Schreiber, "Stable

high-energy proton acceleration with water-leaf targets driven by intense laser pulses," *Phys. Rev. Res.*, vol. 7, p. 023190, May 2025. [Online]. Available: https://link.aps.org/doi/10.1103/PhysRevResearch.7.023190

[125] M. Gauthier, C. B. Curry, S. Göde, F.-E. Brack, J. B. Kim, M. J. MacDonald, J. Metzkes, L. Obst, M. Rehwald, C. Rödel, H.-P. Schlenvoigt, W. Schumaker, U. Schramm, K. Zeil, and S. H. Glenzer, "High repetition rate, multi-MeV proton source from cryogenic hydrogen jets," *Applied Physics Letters*, vol. 111, no. 11, p. 114102, sep 2017. [Online]. Available: https://pubs.aip.org/apl/article/111/11/114102/149763/High-repetition-rate-multi-MeV-proton-source-from

[126] M. Nishiuchi, I. Daito, M. Ikegami, H. Daido, M. Mori, S. Orimo, K. Ogura, A. Sagisaka, A. Yogo, A. S. Pirozhkov, H. Sugiyama, H. Kiriyama, H. Okada, S. Kanazawa, S. Kondo, T. Shimomura, M. Tanoue, Y. Nakai, H. Sasao, D. Wakai, H. Sakaki, P. Bolton, I. W. Choi, J. H. Sung, J. Lee, Y. Oishi, T. Fujii, K. Nemoto, H. Souda, A. Noda, Y. Iseki, and T. Yoshiyuki, "Focusing and spectral enhancement of a repetition-rated, laser-driven, divergent multi-mev proton beam using permanent quadrupole magnets," *Applied Physics Letters*, vol. 94, no. 6, p. 061107, 02 2009. [Online]. Available: https://doi.org/10.1063/1.3078291

[127] C. Greb, E. Aktan, R. Adam, A. Dickson, C. Sire, V. E. Nefedova, F. Sylla, R. Lopez-Martens, C. M. Schneider, J. Faure, and M. Büscher, "Advanced Laser–Plasma Diagnostics for a Modular High-Repetition-Rate Plasma Electron Accelerator," *Instruments*, vol. 8, no. 3, p. 40, aug 2024. [Online]. Available: https://www.mdpi.com/2410-390X/8/3/40